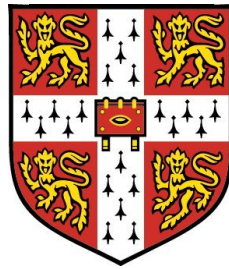# Studying Galaxy Formation Through Lyman Alpha in Emission and Absorption

THIS DISSERTATION IS SUBMITTED FOR
THE DEGREE OF DOCTOR OF PHILOSOPHY

OCTOBER, 2009

Luke Andrew Barnes

INSTITUTE OF ASTRONOMY

AND

WOLFSON COLLEGE

UNIVERSITY OF CAMBRIDGE

To Bernadette, for everything.

She made beauty all around her ...
when she ran in the rain,
the rain was silver.

C.S.Lewis, Till We Have Faces

Declaration

I hereby declare that my thesis entitled *Studying Galaxy Formation Through Lyman Alpha in Emission and Absorption* is not substantially the same as any that I have submitted for a degree or diploma or other qualification at any other University. I further state that no part of my thesis has already been or is being concurrently submitted for any such degree, diploma or other qualification.

This dissertation is the result of my own work and includes nothing that is the outcome of work done in collaboration except where specifically indicated in the text. Various figures throughout the text are reproduced from the work of other authors, for illustration or discussion. Such figures are always credited in the associated caption.

Those parts of this thesis which have been published or accepted for publication are as follows:

- The work presented in Chapter 4 has been completed in collaboration with M. G. Haehnelt and is published as: Luke A. Barnes, Martin G. Haehnelt, 2009 "A joint model for the emission and absorption properties of damped Lyman alpha absorption systems", *Monthly Notices of the Royal Astronomical Society*, 397, 511.

- The work presented in Chapters 3 and 5 have been completed in collaboration with M. G. Haehnelt and have been submitted to *Monthly Notices of the Royal Astronomical Society*.

This thesis contains fewer than 60,000 words.

Luke Andrew Barnes
Cambridge, September 2009

Summary

Galaxy formation is one of the central problems of Physical Cosmology. Neutral hydrogen plays an important role, linking the collapse of cooling gas into haloes with the formation of stars. Lyman alpha, hydrogen's strongest spectral line, can directly probe neutral hydrogen in the high redshift Universe. Lyα can be observed in absorption in Damped Lyman Alpha systems (DLAs): high H I column density regions that dominate the neutral gas content of the Universe between $z \sim 0 - 5$. Lyα in emission is an important signature of early, star-forming galaxies. Both populations, however, present significant theoretical challenges. As part of my thesis, I have developed a Monte Carlo Lyα radiative transfer code to investigate models of early galaxies.

Rauch et al. (2008) performed an ultra-deep spectroscopic survey and discovered a new population of very faint, spatially extended Lyα emitters, which they claimed to be the long-sought host galaxies of DLAs at $z \sim 3$.

I show here that a simple analytical model, which reproduces the incidence rate and kinematics of DLAs in the context of ΛCDM models for structure formation, also reproduces the size distribution of the faint Lyα emitters for plausible parameters, which supports their identification as DLA host galaxies. The model suggests that galaxies in haloes with $v_c \sim 100 - 150$ km s^{-1} account for the majority of DLA host galaxies, and that these galaxies at $z \sim 3$ are the building blocks of typical present-day galaxies like our Milky Way.

I further use my newly developed Lyα code to perform detailed 1D radiative transfer calculations, investigating the spatial and spectral distribution of Lyα emission due to star formation at the centre of DLAs, and its dependence on the spatial and velocity structure of the gas. The modelling reproduces the observed properties of both DLAs and the faint Lyα emitters, including the velocity width and column density distribution of DLAs and the large observed spatial extent of the faint emitters. In the model, haloes hosting DLAs retain up to 20% of the cosmic baryon fraction in the form of neutral hydrogen. The scattering of Lyα photons at the observed radii, which can be as large as 50 kpc, requires the bulk velocity of the gas at the centre of the haloes to be moderate.

I furthermore perform 3D Lyα radiative transfer simulations, building on numerical simulations of galaxy formation that include galactic winds and gas infall. The Lyα emission region is shown to be larger and smoother than the cross-section for damped absorption by $\sim 50\%$, with Lyα photons scattered effectively by gas with column densities $\gtrsim 10^{17}$ cm^{-2}. The spectra typically show two peaks, with the relative strength of the red (blue) peak being a reflection of the relative contribution of outflow (inflow) in the velocity profile. There is considerable variation in the observed line profile and spectral intensity with viewing angle. These more realistic models support many of the simplifying assumptions of my previous models, and have the potential to probe the important role of galactic winds in protogalaxies.

The main conclusion is that the faint population of Lyα emitters are indeed the long-sought host population of DLAs. Ultra-faint observations of Lyα emission have exceptional potential to directly probe the spatial distribution and kinematics of neutral hydrogen in early galaxies.

ACKNOWLEDGEMENTS

Contents

List of Figures

List of Tables

List of Acronyms

AGN	Active Galactic Nuclei
AMR	Adaptive Mesh Refinement
CDM	Cold Dark Matter
CMB	Cosmic Microwave Background
DHS06	Dijkstra et al. (2006a)
DLA	Damped Lyman alpha Absorber
DM	Dark Matter
ESO	European Southern Observatory
FLE	Fluorescent Lyα Emitter
FLRW	Friedmann-Lemaître-Robertson-Walker
FORS	FOcal Reducer and low dispersion Spectrograph
FWHM	Full Width Half Maximum
HAWK-I	High Acuity Wide field K-band Imager
HDF	Hubble Deep Field
HUDF	Hubble Ultra Deep Field
ICM	InterCloud Medium
IGM	InterGalactic Medium
IMF	Initial Mass Function
IR	InfraRed
ISM	InterStellar Medium
LAB	Lyman Alpha Blob
LAE	Lyman Alpha Emitter
LBG	Lyman Break Galaxy
LLS	Lyman Limit System
LOS	Line Of Sight
LRIS	Low Resolution Imaging Spectrometer
MUSE	Multi Unit Spectroscopic Explorer
MUSYC	MUltiwavelength Survey by Yale-Chile

NFW	Navarro Frenk White (Navarro et al. 1996)
PM	Particle Mesh
PSF	Point Source Function
QSO	Quasi-Stellar Object
R08	Rauch et al. (2008)
RT	Radiative Transfer
RW	Robertson-Walker
SDSS	Sloan Digital Sky Survey
SN	Supernovae
SPH	Smoothed-Particle Hydrodynamics
THINGS	HI Nearby Galaxies Survey
UVB	Ultra Violet Background
UV	Ultra Violet
VLT	Very Large Telescope
WMAP	Wilkinson Microwave Anisotropy Probe

Chapter 1

Introduction

> ...the very name "Space" seemed a blasphemous libel for this empyrean ocean of radiance in which they swam. No: space was the wrong name. Older thinkers had been wiser when they named it simply the heavens — the heavens which declared the glory.
>
> *C.S.Lewis, Out of the Silent Planet*

1.1 The Standard Model of Cosmology

The most exciting developments in cosmology in the last decade have undoubtedly been observational. Cosmological parameters that are crucial to our ability to understand the past and predict the future of our Universe have been measured to a high degree of accuracy. A wide range of observations has been brought together to reach this level of precision. These include measurements of the Cosmic Microwave Background (CMB) by the Wilkinson Microwave Anisotropy Probe

(WMAP, Spergel et al. 2003, 2007) and other experiments (Grainge et al. 2003, Kuo et al. 2004, Piacentini et al. 2006); the clustering of galaxies, studied using large surveys such as the 2dF Galaxy Redshift Survey (Cole et al. 2005) and the Sloan Digital Sky Survey (Tegmark et al. 2004, Eisenstein et al. 2005); evidence of the acceleration of the expansion of the Universe from Type 1a supernovae (Perlmutter et al. 1999, Riess et al. 2004, Astier et al. 2006); weak lensing experiments (Bacon et al. 2003, Heymans et al. 2005, Semboloni et al. 2006); X-ray luminous galaxy clusters (Allen et al. 2003, Bahcall & Bode 2003, Voevodkin & Vikhlinin 2004); Lyα forest data (Croft et al. 2002, Viel et al. 2004, Jena et al. 2005, Seljak et al. 2005). Our confidence in the standard model of cosmology comes from the remarkable agreement between these very different methods of measuring cosmological parameters.

These observations reveal that the Universe is homogeneous and isotropic on large scales, spatially flat, and expanding at an accelerating rate. The energy content of the Universe is dominated by dark energy, whose repulsive gravity drives the accelerating expansion, but whose identity remains a mystery[1]. The matter content of the Universe is dominated by dark matter, which is believed to be cold (i.e. it moves with negligible velocity dispersion). Structure formation in a Cold Dark Matter (CDM) universe is *hierarchical* — the smallest structures collapse first and merge continuously under the effect of gravitational instability to form more and more massive structures.

In this chapter, we will introduce the standard model of cosmology, in which the observational results mentioned above are interpreted. We will then move on to the specific issue of the formation of cosmic structure and, in particular, galaxies.

1.1.1 The Friedmann-Lemaître-Robertson-Walker (FLRW) Model

The Robertson-Walker (RW) Metric

Modern cosmology is based on the surprisingly accurate assumption that the Universe is homogenous and isotropic. Surprising, because in spite of the obvious

---

[1] It is also possible that the acceleration of the Universe is due to a modification of gravity on large scales. See Nojiri & Odintsov (2006), Frieman et al. (2008) for a review.

(over-)simplicity of this assumption, observations do not require anything more complicated to explain the Universe as a whole; astrophysical structures are mere perturbations on this background. Robertson (1935) and Walker (1936) independently derived a metric that describes spacetime intervals in a homogeneous and isotropic universe. The line element for this metric is,

$$\mathrm{d}s^2 = c^2\mathrm{d}t^2 - R^2(t)\left[\mathrm{d}\chi^2 + S_k^2\left(\mathrm{d}\theta^2 + \sin^2\theta\mathrm{d}\phi^2\right)\right], \qquad (1.1)$$

where c is the speed of light; $S_k(\chi) = \sin\chi,\ \chi,\ \sinh\chi$ (for $k = +1, 0, -1$); k is the spatial curvature and (χ, θ, ϕ) are spherical polar comoving coordinates — objects in the Universe with fixed comoving coordinates are said to be following the "Hubble flow". The most important factor in Equation (1.1) is $R(t)$, known as the scale factor. We can relate the scale factor[1] to redshift (z),

$$\frac{R(t)}{R_0} \equiv a(t) = \frac{1}{1+z}. \qquad (1.2)$$

The Friedmann Equations

The field equations of general relativity relate the geometry of spacetime (via the metric) to the energy density of the Universe (in the form of a stress-energy tensor). We make the reasonable assumption that the stress-energy tensor is the perfect fluid tensor, with the fluid particles (galaxies) following non-intersecting geodesic trajectories. This is known as Weyl's Postulate.

General relativity, given the perfect fluid tensor and the RW metric, relates the scale size of the Universe to its energy content. The result is the Friedmann equations (Friedmann 1922, Lemaître 1931),

$$H^2 \equiv \left(\frac{\dot{R}}{R}\right)^2 = \frac{8\pi G}{3}\rho - \frac{kc^2}{R^2}, \qquad (1.3a)$$

$$\dot{\rho} = -3H(\rho + \mathrm{p}), \qquad (1.3b)$$

$$\frac{\ddot{R}}{R} = -\frac{4\pi G}{3}(\rho + 3\mathrm{p}), \qquad (1.3c)$$

where an overdot refers to differentiation with respect to time, ρ is total energy density, p is pressure and H is the Hubble parameter. H is time dependant

---

[1]Subscript 0 always refers to a quantity evaluated at the present time.

and has units of $[time]^{-1}$ so that H^{-1} gives a characteristic time scale for the expansion. Equation (1.3a) is known as the expansion equation, (1.3b) is the adiabatic equation and (1.3c) is the acceleration equation. We can derive any one of these equations from the other two.

The Universe contains energy components (labelled i), each with a corresponding pressure p_i and energy density ρ_i, that contribute to the total $p = \sum_i p_i$, $\rho = \sum_i \rho_i$. We specify components by their equation of state,

$$w_i \equiv \frac{p_i}{\rho_i}. \tag{1.4}$$

For example, matter (i = m) has $w_m = 0$, radiation (i = r) has $w_r = 1/3$.

By putting $k = 0$ into (1.3a), we define the critical density,

$$\rho_{\text{crit}} \equiv \frac{3H^2}{8\pi G} \qquad \text{and} \qquad \Omega_i \equiv \frac{\rho_i}{\rho_{\text{crit}}}, \tag{1.5}$$

where Ω_i is the dimensionless density parameter for component i. Then, by (1.3a) the sum over all the density parameters is,

$$\Omega \equiv \sum_i \Omega_i = 1 + \frac{kc^2}{R^2 H^2}. \tag{1.6}$$

This allows us to see explicitly the connection between the energy density and the geometry of the Universe,

$$k = +1 \iff \Omega > 1 \quad \text{(Overdense universes have positive curvature),} \tag{1.7}$$
$$k = 0 \iff \Omega = 1 \quad \text{(Critical-density universes have no curvature),} \tag{1.8}$$
$$k = -1 \iff \Omega < 1 \quad \text{(Underdense universes have negative curvature).} \tag{1.9}$$

For flat universes, R_0 is arbitrary. For non-flat universes, there is a relationship between R_0, H_0 and Ω_0 (from Equation (1.6)),

$$R_0 = \frac{c}{H_0} \left(|\Omega_0 - 1|\right)^{-1/2}. \tag{1.10}$$

The Cosmological Constant

The right hand side of Equation (1.3c) shows that for positive ρ and p, the scale size of the universe is not constant. Einstein realised this soon after deriving the

h	0.701	Hubble constant (in units of 100 km s^{-1}Mpc^{-1})
Ω_m	0.279	Present-day matter density
Ω_Λ	0.721	Present-day dark energy density
Ω_b	0.0462	Present-day baryonic matter density
σ_8	0.817	Amplitude of the mass density fluctuations
n	0.960	Slope of the initial power spectrum

Table 1.1: Cosmological parameters from WMAP5 (Hinshaw et al. 2009).

field equations of general relativity and, guided by his belief that the Universe was static, altered the equations. He added an extra term, dubbed the cosmological constant (Λ), which has since lost its original motivation but is retained in our equations for the sake of generality. In the context of the FLRW model, the cosmological constant can be thought of as an energy component (i = Λ) with,

$$\rho_\Lambda \equiv \frac{\Lambda}{8\pi G} \qquad \text{and} \qquad p_\Lambda = -\rho_\Lambda. \tag{1.11}$$

1.1.2 The Parameters of the Standard Model

A wide range of observations has converged on a set of parameters for the FLRW model, known as the standard model of cosmology. These parameters are given in Table 1.1.

1.2 Cosmic Structure

Explaining the formation of structure in the Universe is one of cosmology's most ambitious goals. Questions remain about the sequence of events that link the extreme smoothness of the early Universe (as seen in the CMB) to today's stars, galaxies, and clusters.

The standard explanation for the growth of structure in the Universe is the gravitational instability scenario (Eggen et al. 1962, Sandage et al. 1970, Press & Schechter 1974, White & Rees 1978, Peebles 1993). Tiny perturbations from homogeneity grow under gravitational attraction to form the large overdensities

we observe today[1]. The primordial density perturbations are thought to be laid down during inflation (for a review of this topic, see Weinberg 2008).

Structure growth occurs in two conceptual stages. The first is the *linear regime* — perturbations can be modelled as small deviations from uniformity. Much of the essential physics can be extracted from a Newtonian approach, without the complications of linearising general relativity. The standard procedure (see, for example, Peacock 1999) is to perturb the Euler, energy and Poisson equations for non-relativistic fluid flow away from the Hubble flow. We can combine these equations into a single equation for the time evolution of the amplitude of a density perturbation $[\delta \equiv (\rho - \bar{\rho})/\bar{\rho}]$ with comoving wavenumber k in a matter-dominated universe,

$$\ddot{\delta} + 2H\dot{\delta} = \delta \left(4\pi G\bar{\rho} - \frac{c_s^2 k^2}{a^2} \right), \tag{1.12}$$

where $\bar{\rho}$ is the average matter density of the universe and c_s is the sound speed. Each Fourier mode of the density field evolves independently according to this equation. Whether the right hand side (the driving term) is positive or negative depends on the scale of the perturbation. On large scales (small k), gravity dominates and perturbations can grow. On small scales, pressure can effectively counteract gravity and the perturbation simply oscillates. The critical scale is called the Jeans length (λ_J).

A particularly relevant case is that of a fluid of cold dark matter and baryons. The dark matter can cluster significantly before recombination, when the baryons are released from their coupling (via Thompson scattering) to the radiation fluid. The equation for the evolution of the density perturbation of baryons and dark matter in matrix form is,

$$L \begin{pmatrix} \delta_b \\ \delta_d \end{pmatrix} = \frac{4\pi G\bar{\rho}}{\Omega} \begin{pmatrix} \Omega_b & \Omega_d \\ \Omega_b & \Omega_d \end{pmatrix} \begin{pmatrix} \delta_b \\ \delta_d \end{pmatrix}, \tag{1.13}$$

where $L \equiv \partial^2/\partial t^2 + 2H\partial/\partial t$. The matrix has two time-independent eigenvalues: $(1, 1)$ and $(\Omega_d, -\Omega_b)$. These represent two modes, and each mode allows two power-law solutions: $\delta \propto t^n$ with $n = 2/3, -1$ and $0, -1/3$. A perturbation that

---

[1]This may seem obvious, but there was a contender to this scenario in the early 1970's. It was proposed that galaxies formed as a result of primordial cosmic turbulence. The extreme isotropy of the CMB led to the abandonment of these theories (see Coles & Lucchin 2002, pg. 212).

begins in one of these modes will remain in that mode, while the solution for a general perturbation will be a linear combination of these solutions. The initial condition relevant for our Universe is $\delta_b \ll \delta_d$ due to radiation drag: electrons moving with respect to the CMB experience a drag force as they Compton-scatter photons. This means that perturbations in (pre-recombination) baryons are held back with respect to dark matter. This combination of modes will evolve to be dominated by the fastest growing mode ($n = 2/3$), for which $\delta_b = \delta_d$. In other words, *baryons fall into existing dark matter potential wells.*

The full, general relativistic treatment allows for the accurate calculation of the transfer function, defined as,

$$T_k \equiv \frac{\delta_k(z = 0)}{\delta_k(z)D(z)}, \tag{1.14}$$

where $D(z)$ is the linear growth factor, calculated taking only gravity into account. The transfer function thus tracks scale-dependent modifications to the perturbation spectrum from effects such as gas or radiation pressure on scales smaller than the Jeans mass, and the dissipative effects of free-streaming and random walking, which erases structure on scales small enough that particles can travel out of perturbations.

The *non-linear* regime begins when the deviations from uniformity can no longer be considered "small". In general, N-body simulations are needed to model the effects of gravity in this regime. However, in the special case of a spherically symmetric overdensity, we have an analytic solution that captures the fundamentals of the scenario. In fact, it is formally the same solution as for an overdense, closed universe. Initially, the sphere of matter expands with the Hubble flow and follows the predictions of linear theory. The onset of the non-linear regime brings three important stages:

- Turnaround: The overdensity's self-gravity halts its expansion. The sphere reaches its maximum radius and stalls.
- Collapse: The overdensity begins to collapse. Formally, this would continue until the density at the centre of the overdensity became infinite. Linear theory predicts a corresponding overdensity of $\delta_{\text{lin}} = 1.686$ for an Einstein-de Sitter universe.

- Virialisation: In practice, asymmetries mean that infalling motion is converted into random motion. The virial theorem predicts that the overdensity will stabilise when it reaches an equilibrium state where $U = -2K$, where U is the gravitational potential energy and K is the kinetic energy. The overdensity is said to have virialised.

These calculations give us the following rule of thumb: linear theory applies until δ_{lin} reaches some critical δ_{c}, often taken to be the linear overdensity predicted at the time of collapse in the spherical collapse model.

The spherical collapse model only includes the effects of gravity, and as such only applies when other forces are negligible. This is the case when the collapsing matter is dark matter, which only interacts gravitationally. Virialised dark matter overdensities are called dark matter haloes. Analytical models that combine linear theory and spherical collapse have proven effective (when tested against N-body simulations) in modelling the statistical properties of dark matter haloes in the non-linear regime. However, before we can consider these methods, we will need some tools to analyse cosmological density fields.

1.2.1 Cosmological Density Fields

The generation of primordial perturbations is a stochastic process. Hence, the exact form of $\delta(\boldsymbol{x})$ cannot be predicted from first principles; we need statistical measures of the density field. We begin with the *correlation function*,

$$\xi(\boldsymbol{r}) \equiv \langle \delta(\boldsymbol{x})\delta(\boldsymbol{x}+\boldsymbol{r})\rangle, \tag{1.15}$$

which is the autocorrelation function of the density field; the angled brackets indicate an average over the normalisation volume V. In an isotropic universe, it depends only on $r \equiv |\boldsymbol{r}|$. For galaxies, it gives the excess probability of finding a galaxy at a distance r from a given galaxy. It can also be expressed as,

$$\xi(\boldsymbol{r}) = \frac{V}{(2\pi)^3} \int |\delta_{\boldsymbol{k}}|^2 e^{-i\boldsymbol{k}\cdot\boldsymbol{r}} \, \mathrm{d}^3 k. \tag{1.16}$$

Thus, the correlation function is the Fourier transform of the *power spectrum*,

$$P(k) \equiv \langle |\delta_k|^2 \rangle, \tag{1.17}$$

where, as before, in an isotropic universe it depends only on $k \equiv |\boldsymbol{k}|$.

In the absence of a physical theory that predicts the power spectrum, there is nothing to pick out a particular scale as special. In this case, we expect a featureless power-law spectrum, $P(k) \propto k^n$. A power-law spectrum implies a power-law correlation function.

An important special case is the *scale-invariant* or *Zeldovich spectrum*; if we set $n = 1$, then when the universe is viewed on the scale of the horizon r_{H}, it looks the same as the universe expands i.e. $\delta(r_{\mathrm{H}}) \approx$ constant. Fluctuations in the gravitational potential are independent of the length scale for such a spectrum.

We are often interested in the properties of the density field on a certain scale. We can smooth the density field using a filter function, such as a spherical top-hat in real space. The filter function in real space f has a corresponding filter in k-space, f_k. An important statistical quantity is the variance of the filtered field,

$$\sigma^2 = \frac{V}{(2\pi)^3} \int P(k)|f_k|^2 \; \mathrm{d}^3 k. \tag{1.18}$$

The normalisation of the power spectrum is usually specified by σ_8, which is the rms density variation of the density field when smoothed with a top-hat filter of radius $8h^{-1}\mathrm{Mpc}$.

1.2.2 Hierarchical Structure Growth and the Press-Schechter Formalism

The standard model of galaxy formation states that structures in the Universe form when baryons cool and collapse inside dark matter haloes. As a simple model of structure in the Universe, we can consider the properties of these haloes. The advantage of this approach is that surprisingly accurate analytical models of the abundance of dark matter haloes of different masses have been developed. The obvious downside is that we are ignoring the significant complications of baryonic physics. Nevertheless, these models have proven to be very useful.

The first attempt to calculate the abundance (as a function of mass) of gravitationally bound structures was made by Press & Schechter (1974). Press-Schechter theory is used very widely in the literature because it has proven to be very accurate in reproducing the results of N-body simulations (Baugh 2006, and references therein). The theory is explained in detail in a number of textbooks (Peacock

1999, Liddle & Lyth 2000, Coles & Lucchin 2002), so we will only need to review the basics here.

Press-Schechter theory is a hybrid of linear theory and the spherical collapse model. We begin by considering the density contrast of the matter in the Universe, $\delta(\boldsymbol{r}, t) = \rho(\boldsymbol{r}, t)/\bar{\rho}(t) - 1$, where $\bar{\rho}$ is the background cosmic matter density. The growth of the Fourier modes of this field can be accurately predicted in the linear regime. The idea behind Press-Schechter theory is that while linear theory will not allow us to follow the collapse of structures once $\delta \gtrsim 1$, it should at least allow us to identify the sites, size, and mass of collapsed structures via the peaks in the linear density field.

Given the density field as predicted by linear theory, we can probe different scales, R, (and consequently different mass scales $M = 4/3\pi\bar{\rho}R^3$) by smoothing the field in spheres of radius R. Press-Schechter theory asserts that the fraction of space in which the density field (smoothed on some mass scale M) exceeds some threshold δ_c is in collapsed objects of mass greater than M. For a density field that obeys Gaussian statistics, the comoving number density of haloes with mass between M and $M + \mathrm{d}M$ at a redshift of z is given by,

$$n_{\mathrm{ps}}(M, z)\,\mathrm{d}M = \sqrt{\frac{2}{\pi}}\frac{\bar{\rho}_0}{M}\frac{\mathrm{d}\nu}{\mathrm{d}M}\exp\left(-\frac{\nu^2}{2}\right)\,\mathrm{d}M, \qquad (1.19)$$

where $\nu \equiv \delta_c/[D(z)\sigma(M)]$, $\sigma(M)$ is the rms-mass fluctuation in spheres containing mass M — fitting formulae for a ΛCDM cosmology an be found in Mo & White (2002), $D(z) = g(z)/[g(0)(1 + z)]$ is the linear growth factor — a fitting formula for $g(z)$ can be found in Carroll et al. (1992), and $\bar{\rho}_0$ is the present-day background cosmic matter density. The link with the spherical collapse model comes in the choice of the critical overdensity δ_c. By considering a spherical overdensity, both in linear theory and with the exact solution, we discover that when the overdensity has reached maximal compression ($\delta \sim 200$), linear theory predicts an overdensity of $\delta \approx 1.686$ for an Einstein-de Sitter universe. Thus, we postulate that any region for which the linearly extrapolated density contrast is $\gtrsim \delta_c \approx 1.686$ has collapsed to form a virialised halo.

Press-Schechter theory has been extensively studied (see Baugh 2006). In particular, Bond et al. (1991) attacked the problem using excursion set theory. This approach makes the derivation of the Press-Schechter mass function more rigorous, and allows the formalism to be extended, providing a way to calculate

such quantities as merger rates, formation times, and survival times. The increasing accuracy of N-body simulations has led to refinements to the Press-Schechter ansatz. Sheth & Tormen (2002) proposed an alteration to Equation (1.19) using a ellipsoidal model of collapse. The Sheth-Tormen mass function is,

$$n_{\mathrm{st}}(M, z)\, \mathrm{d}M = A \left(1 + \frac{1}{\nu'^{2q}}\right) \sqrt{\frac{2}{\pi}} \frac{\bar{\rho}_0}{M} \frac{\mathrm{d}\nu'}{\mathrm{d}M} \exp\left(-\frac{\nu'^2}{2}\right)\, \mathrm{d}M, \qquad (1.20)$$

where $\nu' = \sqrt{a}\nu$, $a = 0.707$, $A \approx 0.322$, and $q = 0.3$.

1.2.3 Galaxy Formation

Galaxy formation is complicated by baryonic physics. The general outline of the process is the same as before — baryons clump together through gravitational instability. However, baryons are subject to the smoothing effects of gas pressure, which counteracts the force of gravity effectively on scales smaller than the Jeans length, as well as energy loss processes such as radiative cooling. Numerical simulations that include hydrodynamic effects show that baryons form a web-like structure (Bond et al. 1996), where the densest regions are the "knots" of matter at the intersection of filaments. It is in these regions that the gas is dense enough to form luminous objects like stars, galaxies, and quasars.

White & Rees (1978) presented the following theoretical framework for galaxy formation. Firstly, dark matter haloes form via gravitational instability as outlined above. Then, the baryonic component falls into the pre-existing dark matter potential wells, as we saw in the linear case. The infalling gas is shock-heated to the virial temperature of the halo,

$$T_{\mathrm{vir}} = \frac{\mu m_{\mathrm{H}} v_{\mathrm{c}}^2}{2 k_{\mathrm{B}}} \approx 10^6 \text{ K} \left(\frac{v_{\mathrm{c}}}{165 \text{ km s}^{-1}}\right)^2, \qquad (1.21)$$

where $v_{\mathrm{c}} = (GM/R_{\mathrm{vir}})^{1/2}$ is the circular velocity of the halo, R_{vir} is its virial radius and μ is the mean molecular weight of the gas. (We will see later, however, that more recent work has somewhat changed our understanding of this process in ways that are very relevant to Lyα emission). The collapse is halted when the gas becomes pressure-supported. The crucial process that allows further contraction is radiative cooling. The gas (for masses and radii relevant to galaxies) is at temperatures well above 10^4 K, and is thus ionised. It will cool radiatively on

a short timescale and rapidly collapse into the halo, eventually settling into a rotationally supported disk (Fall & Efstathiou 1980). Meanwhile, the cool dense gas will fragment, triggering star formation. Thus, galaxies form as a concentrated luminous core embedded in an extensive dark matter halo. Clusters of galaxies form in a hierarchical fashion — smaller systems merge into an amorphous whole. Galaxies become sufficiently concentrated during their cooling phase that they can survive the mergers that disrupt their haloes. This explains why we see clusters of individual galaxies, and not cluster-sized galaxies.

There are three relevant timescales in this process. Already mentioned is the cooling time, defined as the time taken to radiate away the thermal energy of the system (Coles & Lucchin 2002, pg. 311),

$$t_{\text{cool}} = \frac{3nk_{\text{B}}T}{2\Lambda(T)}, \tag{1.22}$$

where n is the gas number density and $\Lambda(T)$ is the cooling function (energy radiated away per unit time), which depends on the temperature, density, and chemical composition of the gas. The so-called dynamical timescale is defined as the freefall time for a sphere of density ρ,

$$t_{\text{dyn}} = \sqrt{\frac{3}{32\pi G\rho}}, \tag{1.23}$$

which is related to the time taken for the gas to reach virial equilibrium and become pressure-supported. Finally, the Hubble time $t_{\text{H}} = H_0^{-1}$ is related to the age of the Universe. For gas to cool inside dark matter haloes we must have:

- $t_{\text{cool}}, t_{\text{dyn}} < t_{\text{H}}$ — so that all relevant processes have had enough time to produce structure by the present epoch;
- $t_{\text{cool}} < t_{\text{dyn}}$ — so that radiative cooling can remove thermal energy from the gas quickly enough to prevent the gas becoming pressure-supported, allowing almost freefall collapse.

These conditions set a characteristic upper limit to galactic masses and sizes (White & Rees 1978).

While this scenario has been altered and extrapolated since it was first proposed (see the summary in Mo et al. 1998), it remains fundamentally unchanged

as the framework for theories of galaxy formation. However, there are many complicating factors that need to be considered — e.g. the physics of star formation, the hydrodynamics of the gas, the role of magnetic fields, and the role of merging and interactions with other galaxies (Giavalisco 2002). Here we will discuss a particular effect that will be of some importance later: the action of feedback by supernovae (SN), Active Galactic Nuclei (AGN), and stellar winds. The following paragraphs follow the excellent discussion in Ciardi & Ferrara (2005).

Feedback in this context refers to a back-reaction of the process of star/galaxy formation on itself. There are three broad classes of feedback — radiative, mechanical, and chemical (which we will not need to consider here). Radiative feedback refers to ionising/dissociating radiation produced by massive stars and quasars. This Ultra Violet (UV) radiation field inhibits the formation of galaxies and stars for two main reasons. Firstly, photoheating prevents collapse via radiative cooling and the formation of cool neutral clouds of hydrogen out of which stars condense. Secondly, gas can photoevaporate out of the host halo if it heated above the virial temperature. Thoul & Weinberg (1996) show that objects as large as $v_c \sim 30$ km s^{-1} can be photoevaporated and prohibited from collapsing, a conclusion reinforced by Kitayama et al. (2000), Susa & Kitayama (2000), Kitayama et al. (2001), Okamoto et al. (2008). This radiation, of course, is also responsible for cosmic reionisation (Barkana & Loeb 2001).

Mechanical feedback refers to the mass, energy, and momentum deposited in the InterStellar Medium (ISM) and InterGalactic Medium (IGM) by particles ejected by stellar winds, supernovae and AGN. Within galaxies, star formation can be significantly affected by gas being blown out of the galaxy. These ejecta form a galactic wind, depositing energy and metals into the IGM, even into the low-density environment of the Lyα forest. There is evidence for galactic winds in the high redshift Universe; see the review in Veilleux et al. (2005). For example, most $z \sim 3 - 4$ Lyman Break Galaxies (LBGs) have low-ionisation interstellar lines that are blueshifted by hundreds of kilometres per second relative to systematic velocities, and redshifted Lyα lines indicate similar outflow velocities. High redshift Lyα emitters also show red asymmetric or P Cygni profiles, which are indicative of outflow. These winds are expected, especially in LBGs, due to their combination of compact sizes and large star formation rates.

An extreme example of mechanical feedback is a superwind: a burst of rapid,

massive star formation in the early Universe resulting in a rapid burst of supernovae. These supernovae could overlap and evolve into a so-called superbubble. If the kinetic energy of this superbubble is enough to overcome the gravitational attraction of the galaxy, then the gas clouds will be blown out into the IGM in what is called a superwind (see Taniguchi & Shioya 2000, and references therein). Superwinds have been observed at $z \simeq 3$ (Wilman et al. 2005), and are invoked by current theories of galaxy formation to terminate star formation in the most massive galaxies and to deposit metals into the IGM.

In the next chapter, we will look at a particular probe of the baryons involved in galaxy formation: Lyα radiation.

Chapter 2

The Lyman Alpha Line and Galaxy Formation

In light of the theoretical uncertainties regarding galaxy formation, it was quickly realised that observational evidence would be essential in guiding our understanding. The most abundant element, and thus the most direct probe of baryons in the Universe, is hydrogen. Neutral hydrogen, in particular, has a vital role in galaxy and star formation — gas that has cooled to allow it to collapse into a halo will be predominantly neutral. Furthermore, stars will not form out of warm ionised gas — they require cold neutral clouds as a precursor to molecular clouds. Thus, to study neutral hydrogen at high redshift is to see galaxy formation as it happens.

The most direct probe of neutral hydrogen is its strongest spectral line, Lyman alpha. The Lyα line is a resonant transition with a frequency of 2.466×10^{15} Hz, corresponding to a jump between the $2\ ^2P$ state to the $1\ ^2S$ (ground) state,

$$\text{H}(2\ ^2P) \leftrightarrow \text{H}(1\ ^2S) + \text{Ly}\alpha. \tag{2.1}$$

Lyα can be used to probe neutral hydrogen in absorption or emission. We will

consider both of these cases.

2.1 Lyman Alpha in Absorption

Lyman alpha is seen in absorption in the spectra of quasars. The large cross-section for the Lyα transition makes this technique by far the most sensitive method for detecting baryons at any redshift (e.g. Rauch 1998). These absorbers are classified into three types according to their neutral hydrogen column density, $N_{\rm HI}$. Lyα forest absorbers have $N_{\rm HI} < 10^{17}$ cm^{-2}, making them optically thin to ionising radiation. Lyman Limit Systems (LLS) have 10^{17} cm$^{-2} < N_{\rm HI} < 2 \times 10^{20}$ cm^{-2}. Damped Lyman alpha Absorbers (DLAs) are the highest column density systems, with $N_{\rm HI} > 2 \times 10^{20}$ cm^{-2}. Damped Lyα absorption profiles are characterised by their Lorentz or damping wings: at such high column densities, unit optical depth occurs in the damping wings of the profile function, beyond the inner Doppler core. This means that the equivalent width of the line is independent of the velocity (and temperature) structure of the absorber. The column density $N_{\rm HI} = 2 \times 10^{20}$ cm^{-2} also fortuitously separates the predominantly ionised LLS population from DLAs, in which the hydrogen is mainly neutral due to self-shielding against ionising radiation.

The connection between neutral hydrogen, the Lyα line, and galaxy formation thus leads us to explore the population of DLAs, the dominant reservoir of neutral gas in the Universe. This section follows the excellent review by Wolfe et al. (2005).

2.1.1 Observational Properties of DLAs

Wolfe (1986) conducted the first DLA survey, looking to find neutral gas in the disks of high redshift galaxies. The principle difficulty in identifying a DLA is in distinguishing a single absorption line that has been broadened by damping from an absorption feature caused by the blending of Doppler-broadened profiles from several low column density systems. The Lyα forest also generates confusion noise, contaminating the damping wings. These problems have been overcome, yielding over a thousand known DLAs. The most comprehensive DLA survey to date comes from the Sloan Digital Sky Survey (SDSS, Prochaska et al. 2005).

2.1.1.1 Column Density Distribution

Following the literature, let the number of absorbers ($d^2\mathcal{N}$) along a random sight-line that have HI column densities in the range $(N, N + dN)$, and are in the redshift range $(z, z + dz)$ be,

$$d^2\mathcal{N} = n_N(N, z)\sigma(N, z)(1 + z)^3 \frac{dl_{\mathrm{p}}}{dz}\,dN\,dz \qquad (2.2)$$

$$\equiv f(N, X)\,dN\,dX, \qquad (2.3)$$

where $n_N\,dN$ is the comoving number density of DLAs within $(N, N + dN)$, σ is the absorption cross-section, the ratio of proper distance interval to redshift interval is given by,

$$\frac{dl_p}{dz} = \frac{c}{H(z)(1 + z)}, \qquad (2.4)$$

and the so-called absorption distance X is defined by,

$$dX \equiv \frac{H_0}{H(z)}(1 + z)^2\,dz. \qquad (2.5)$$

The determination of $f(N, X)$ in the survey (mean redshift $z = 3.06$) of Prochaska et al. (2005) is shown in Figure 2.1. A single power-law is a poor fit. Better fits are given by a Γ function (exponentially suppressed at high N), and a double power law. The parameters for these fitting functions are given in Prochaska et al. (2005). The distribution has a low-N dependence of $f \propto N^2$, and drops very steeply above $N = 10^{21.5}$ cm^{-2}, which can be attributed to the reduced number density of haloes with large mass and the formation of molecular hydrogen in the highest column density clouds. Prochaska & Wolfe (2009) showed that the shape of $f(N, X)$ does not appear to evolve in the redshift range $z = 2.2$ to 5, and in fact is remarkably similar to the corresponding distribution for HI disks in the local Universe, measured using 21cm observations. Only the normalisation of $f(N, X)$ changes with time, which we will consider next.

The zeroth moment of $f(N, X)$ gives the number of DLAs encountered along a line of sight per unit absorption distance dX i.e. the line density of DLAs,

$$l_{\mathrm{DLA}}(X)\,dX \equiv \int_{N_{\mathrm{DLA}}}^{\infty} f(N, X)\,dN\,dX, \qquad (2.6)$$

where $N_{\mathrm{DLA}} = 2 \times 10^{20}$ cm^{-2}. The dependence of l_{DLA} on redshift as determined by Prochaska et al. (2005) is given in Figure 2.2. There is significant evolution
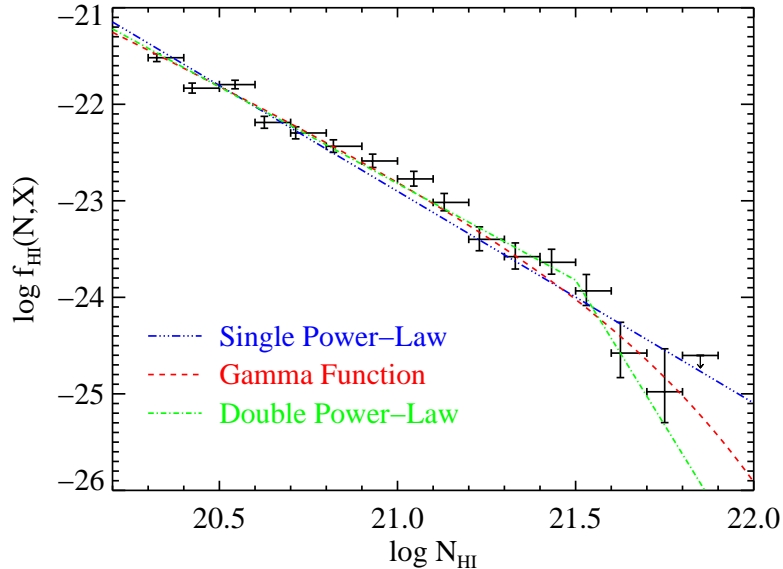
Figure 2.1: DLA column density distribution $f(N, X)$ for all of the systems identified in the SDSS DR3_4 sample (Prochaska et al. 2005). The mean redshift of the sample is $z = 3.06$. Overplotted on the binned data points (with errorbars) are three fitting functions. The blue solid line is a single power law, which is a poor fit to the data. The red dashed line is a Γ function, a power law that is exponentially suppressed at high N. The green dot-dashed line is a double power law, which steepens above $N = 10^{21.5}$ cm^{-2}. The Γ function and double power law are acceptable fits to the data.

from $z = 2.2 - 5.5$, and surprisingly little evolution for $z < 2.2$, a period of approximately 10 Gyr.

The first moment of $f(N, X)$ can be related to the gas mass density of H I atoms,

$$\Omega_g^{\mathrm{HI}}(X) \, \mathrm{d}X = \frac{\mu m_{\mathrm{H}} H_0}{c \rho_{\mathrm{crit}}} \int_{N_{\min}}^{N_{\max}} N \, f(N, X) \, \mathrm{d}N \, \mathrm{d}X \tag{2.7}$$

where μ is the mean molecular mass of the gas; see Prochaska et al. (2005) for a discussion of the choice of $N_{\min}$ and $N_{\max}$. The most important consequence of this calculation is that *DLAs dominate the neutral gas content of the Universe in the redshift interval $z = [0 - 5]$*. Further, DLAs between $z \sim 3.0 - 4.5$ contain sufficient neutral hydrogen to account for a significant fraction of the gas mass in stars in present-day galaxies. It is widely believed (Wolfe et al. 2005), therefore,
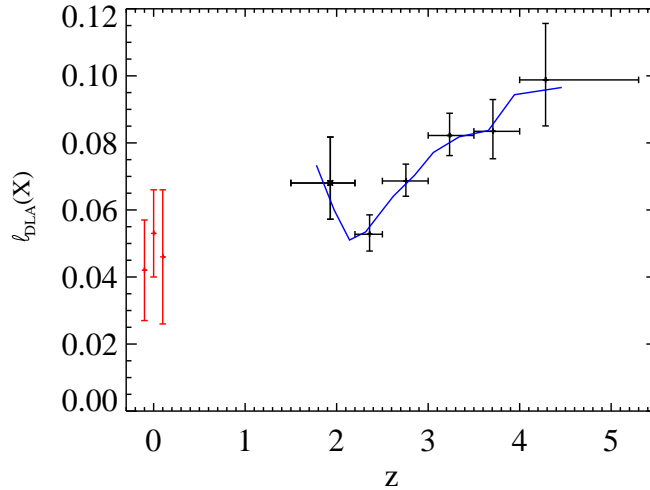
Figure 2.2: The line density of DLAs (l_{DLA}) as a function of redshift, as determined by Prochaska et al. (2005). The curve follows the evolution of l_{DLA} in 0.5 Gyr intervals. The points at $z = 0$ are from three analyses of 21cm observations by Ryan-Weber et al. (2003, 2005), Rosenberg & Schneider (2003), Zwaan et al. (2005).

that DLAs contain or are related to the reservoirs of gas needed to fuel star formation for much of the history of the Universe.

2.1.1.2   Kinematics

An important constraint on the nature of DLAs comes from the velocity profiles of metal lines. As we noted above, because unit optical depth occurs outside the Doppler core, the observed Lyα absorption profiles contain no information about the velocity structure of the gas. Observers have used high-resolution spectroscopy to study so-called low-ionisation metals (or low-ions). Si I, for example has an ionisation potential of 10.4 eV, while for Si II it is 23.3 eV (Dopita & Sutherland 2003). Thus, in a region where neutral hydrogen is self-shielded from photons with energies above its ionisation potential (13.6 eV), the dominant ion of silicon will be Si II. Other low-ions include Mg II, Fe II and Ni II, while N I and O I have ionisation potentials that are greater than 13.6 eV and are thus predominantly neutral in a self-shielded H I region (Viegas 1995).

Thus, we have good reasons to believe that low-ions associated with DLAs
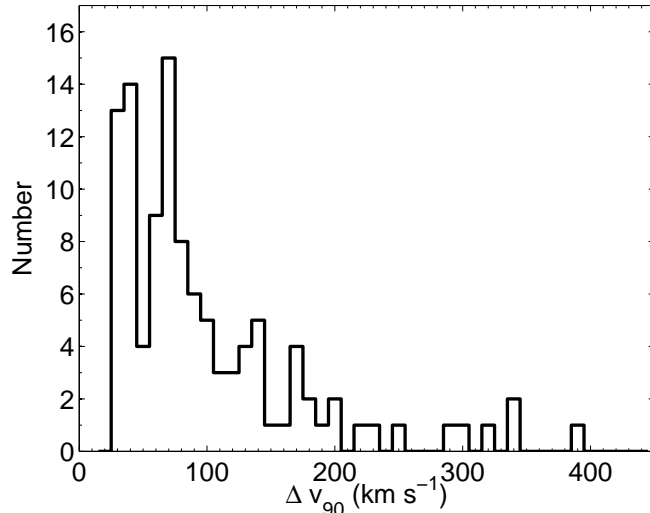
Figure 2.3: Histogram of the velocity width, Δv_{90}, of low-ions associated with the sample of DLAs found in Prochaska et al. (2008). The sample shows velocity widths ranging from 15 km s^{-1} to several hundred km s^{-1} with a median of ≈ 80 km s^{-1}.

trace the neutral gas. Absorption features from low-ionisation metals at the same redshift as the DLA give us crucial information about the kinematics of the neutral gas in DLAs.

The most common statistic used to characterise the width of a low-ion metal absorption feature is Δv_{90}, defined by Prochaska & Wolfe (1997) in their pioneering survey as the velocity interval encompassing 90% of the total integrated optical depth; see also the lucid discussion in Pontzen et al. (2008). (We will often use the more compact notation $v_{\rm w}$.) The observations of Prochaska et al. (2008) are given in Figure 2.3. This figure shows that DLAs exhibit velocity widths ranging from 15 km s^{-1} to several hundred km s^{-1} with a median of ≈ 80 km s^{-1}. The high-velocity tail has been the subject of much theoretical attention, following the claim by Prochaska & Wolfe (1997) that it conflicts with the predictions of hierarchical structure growth within CDM cosmologies.

An important low redshift insight on DLA kinematics comes from 21cm emission from HI in local galaxy disks. Zwaan et al. (2008) point to several lines of evidence that suggest that DLAs at low redshifts ($z \lesssim 1$) are likely to arise in the gas disks of galaxies like those seen in the local Universe. In order to see

whether this was the case at higher redshifts, they used high-quality HI 21cm data to study the gas kinematics of local galaxies. The resultant distribution of Δv_{90} for local galaxies with $N_{\mathrm{HI}} > 2 \times 10^{20}$ cm^{-2} peaks sharply at around 30 km s^{-1}, with a FWHM of ~ 20 km s^{-1} and a shallow tail out to ~ 200 km s^{-1}. This distribution is very different to that shown in Figure 2.3 for high-redshift DLAs — the median is smaller by more than a factor of two. Zwaan et al. (2008) conclude that gas kinematics at high redshifts must be increasingly influenced by gas that does not participate in ordered rotation in cold disks.

2.1.1.3   Metallicity

The connection between DLAs and star formation makes the metallicity of DLAs an important diagnostic quantity. This subsection will follow the reviews of Pettini (2004, 2006), Wolfe et al. (2005). The elemental abundances of DLAs are the most accurate measurements in the high redshift Universe of the chemical enrichment of gas by stars. Furthermore, regardless of their exact identity, the mean metallicity of DLAs is the best measure we have of the amount of metal enrichment of neutral gas in the Universe at a given epoch. The most important points regarding DLA metallicities are:

- DLAs are generally metal-poor at all redshifts. This points to DLAs as arising in gas that is in its earliest stages of star formation.

- No DLAs have been found without significant metal absorption. Specifically, there are no DLAs with $[M/H] < -2.6$.

- Metallicities in DLAs at the same redshift exhibit a wide scatter, indicating different rates and stages of star formation within the DLA population.

- Wolfe et al. (2005) report a statistically significant increase in the cosmic metallicity in DLAs with decreasing redshift, in contrast to the earlier conclusions of Pettini (2004). This is in keeping with the expectation that star formation will pollute the neutral gas with metals via supernovae and stellar winds.

Johansson & Efstathiou (2006) presented a model that uses a physically motivated prescription for stellar feedback to follow the metallicity evolution of DLAs.

Their model reproduced the low mean metallicities in DLAs, concluding that DLAs probe the outer gaseous parts of dwarf galaxies ($v_c \lesssim 70$ km s^{-1}). They further conclude that the galaxies responsible for DLAs make only a small contribution to the total star formation rate of the Universe.

2.1.1.4 The Search for the Hosts of DLAs

Searches for the galaxies that are responsible for damped absorption in QSO spectra have a long history, as observers have sought to shed light on the nature of DLAs. The most common technique is to search adjacent to quasar sightlines with known absorption systems (Fynbo et al. 1999, Bunker et al. 1999, Kulkarni et al. 2000, 2001, Warren et al. 2001, Christensen et al. 2007). This is a difficult task, as the light of the extremely bright quasar must be accurately subtracted in order to study the light from the galaxy, which is very faint in comparison. Kulkarni et al. (2000) and others caution of the possibility that a given emission feature is a Point Source Function (PSF) artefact rather than a real source. Christensen et al. (2007) report that, for $z > 2$, six DLA galaxies have been confirmed through spectroscopic observation of Lyα emission, with other techniques producing a few additional candidates. Christensen et al. added another six Lyα emission candidates to this group. While a quantitative statistical interpretation of the many (largely unsuccessful) searches is difficult, the low success rate appears to be consistent with their interpretation as galaxies of rather low mass and low star formation rate. The ultra-deep, long slit search of Rauch et al. (2008) for the hosts of DLAs will be discussed in Section 2.2.5.

2.1.2 Theoretical Models of DLAs

In the local Universe, most Hi atoms are found in the disks of L_* type galaxies. This motivated Wolfe (1986) to search for the disks of such galaxies at high redshift by looking for high column density Hi in absorption in the spectra of quasars. Thus, DLAs have traditionally been considered to be high-redshift disks of Hi. Other models have been proposed, which we will summarise in this section.

Arons (1972) was the first to suggest that absorption lines in high-redshift QSO spectra could be Lyα absorption from Hi in protogalaxies, though in those models the gas is highly ionised and thus not directly relevant to DLAs. York

et al. (1986) suggested that some DLAs could be associated with gas-rich dwarf galaxies, which would explain the complexity of the metal line profiles. Schiano et al. (1990) used hydrodynamic simulations of the collapse of a gaseous corona into a "Lyα disk" via radiative cooling to test the idea that DLAs originate in large, massive disks of gas that are the progenitors of present-day galaxies. They conclude that such a scenario is plausible, provided there is sufficient metallicity to allow for rapid cooling. Lu et al. (1996), by considering elemental abundances, found that DLAs are much less metal-enriched than the Galactic disk in its past. They concluded that DLAs are not high redshift spiral disks in the traditional sense, postulating thick disks or spheroidal components of (dwarf) galaxies as more likely scenarios.

Within the cosmological context of the CDM model of structure formation, Mo & Miralda-Escude (1994) modelled DLAs as gaseous disks within dark matter haloes. Such models were refined and extended by Kauffmann (1996), who based a disk-formation model on the paradigm of White and Rees: galaxies form by the continuous cooling and accretion of gas within a merging hierarchy of dark matter haloes. The model also incorporates star formation, with the gas supply regulated by infall from the surrounding halo. Chemical enrichment occurs through the ejection of metals back into the hot IGM by supernovae; this gas then cools back onto the disk. This model predicts, with reasonable success, the redshift dependence of $\Omega_{\rm HI}$ as well as $f(N, X)$. A general prediction of this model is that DLAs are smaller, more compact, and less luminous than today's galaxies.

Mo et al. (1998) placed rotationally supported disks within haloes with an NFW density profile (Navarro et al. 1996), allowing the spin parameter λ to vary over a lognormal distribution. These models successfully reproduce $\rm dN/dz$ at $z = 2.5$ by including the contribution of disks with rotation velocities down to 50-100 km s^{-1}.

Gardner et al. (1997a) were among the first to study DLAs using numerical simulations of structure formation. Extending the simulations of Katz et al. (1996a,b), they sought to overcome the problem of the lack of resolution in cosmological simulations. Their simulations could not resolve dark matter haloes below 100 km s^{-1}, while higher resolution simulations of smaller cosmological volumes by Quinn et al. (1996) indicate that haloes as small as 35 km s^{-1} can host DLAs. Their approach was to use the Press-Schechter formalism to extrapolate the re-

23

sults of the simulation to smaller circular velocities. (We will have much more to say about this method in the Chapter 4.) The results for dN/dz are in good agreement with observations for $z = 2 - 4$ in an $\Omega_m = 1$ universe. Gardner et al. (1997b), however, applied this method to other cosmological models, showing that in a ΛCDM universe (with $\sigma_8 = 0.79$), absorbers are underproduced at $2 \lesssim z \lesssim 3$ by a factor of 3. Further simulations (Gardner et al. 2001) produced a more adequate fit to the data, though precise predictions were affected by the uncertainty in determining the smallest halo capable of hosting a DLA.

Prochaska & Wolfe (1997) showed that kinematical data present a considerable challenge to theoretical models of DLAs. They considered six different models for DLAs, and subjected them to four statistical tests based on the velocity width, the displacement of the median from the mean, and the displacement of the two strongest peaks from the mean. The model favoured by the data was that of a single disk with $v_{\rm rot} = 250$ km s^{-1} viewed from different lines-of-sight (LOS), which produces an ensemble of profiles. The disk is thick ($h = 0.4R_d$), and cold ($\sigma_{cc} = 10$km s$^{-1} \ll v_{\rm rot}$), where σ_{cc} is the isotropic velocity dispersion of absorbing clouds within the disk. Despite the obvious oversimplification of using only one representative galaxy rather than a distribution, this model is preferred by the data, passing the four tests. The most significant conclusion of Prochaska & Wolfe (1997) regards a CDM model of DLAs. In this model, $v_{\rm rot}$ for the thick disk is chosen from the distribution $P(v_{\rm rot})$ calculated by Kauffmann (1996) for a CDM cosmology. This model fails to reproduce the velocity width distribution because of the predominance of slowly rotating disks. Making the disk thin only makes things worse. The simulated profiles are also significantly more symmetric than is observed. The other four models considered were a dwarf galaxy (with a hot disk), an isothermal halo, spherical accretion onto a galactic bulge and random motion with a halo. These models are ruled out by the data, often because the absorption profiles are much more symmetric than those observed.

Haehnelt et al. (1998) challenged the assumption that the velocity widths of high redshift galaxies are due solely to rotational motion in disks. In hierarchical structure formation, galaxies are built up from the merging of protogalactic clumps, often moving along filaments. Haehnelt et al. (1998) thus considered absorption arising in more realistic, irregular protogalactic clumps, whose velocity field is a mixture of rotation, infall, merging, and random motion. They used the

hydrodynamic code GRAPESPH to simulate small regions of a CDM universe with high spatial and mass resolution. This high resolution is crucial for resolving the substructure of the clumps. The result was a population of DLAs that was able to reproduce the kinematic data of Prochaska & Wolfe (1997).

McDonald & Miralda-Escudé (1999) considered an analytical model that resembled the scenario of Haehnelt et al. (1998). They considered randomly moving clouds within a spherical halo formed in the context of a CDM universe, and found that such a model was able to reproduce the kinematic data of Prochaska & Wolfe (1997). They also identified the issue of energy dissipation: randomly moving clouds will collide often, producing shocks in the absorbing gas. These shocks seem to dissipate energy at a much higher rate than it can be supplied from the gravitational energy of merging haloes. This could suggest another energy source capable of maintaining gas motions in DLAs.

The next generation of cosmological simulations aimed at DLAs came with the modelling of Nagamine et al. (2004), who used Smoothed-Particle Hydrodynamics (SPH) simulations in the context of the ΛCDM model. Their simulations included the effects of radiative cooling, the Ultra Violet Background (UVB), star formation, supernovae feedback, and in particular considered the effect of galactic winds using a simple phenomenological model that involves giving gas particles a "kick" in a random direction to drive them out of dense star-forming regions. They used the Press-Schechter formalism to extend their results below the resolution limit of their simulations. The result was a reasonable agreement with $\Omega_{\mathrm{HI}}(z)$ so long as "strong" winds were invoked; otherwise, there was too much gas left in the DLAs. Their prediction for $\mathrm{d}N/\mathrm{d}z(z)$ was also reasonably successful — they note that they do not invoke a smallest halo mass capable of hosting a DLA, as Gardner et al. (2001) did. Finally, $f(N, X)$ is slightly underpredicted, with strong winds necessary to prevent overprediction at high-N. Nagamine et al. (2007) refined the previous models with a more careful consideration of winds, concluding that DLAs are hosted by small ($M_{\mathrm{halo}} < 10^{12} h^{-1} M_{\odot}$), faint galaxies.

Further cosmological simulations have been able to model the DLA population without using analytic extensions based on the Press-Schechter formalism. The first to accomplish this was Razoumov et al. (2006), who used AMR cosmological simulations to address both the neutral gas cross-section and the gas kinematics. Their results show that $f(N, X)$ is overpredicted for $N_{\mathrm{HI}} > 10^{21}$ cm^{-2}, which

may be due to the effects of grid resolution or the absence of a model for the formation of H_2, which will affect the highest density systems. The velocity width distribution is dramatically underpredicted, even when star formation is taken into account (Razoumov et al. 2008). Another surprising conclusion of these simulations was the abundance of DLAs that are not associated with any halo — intergalactic DLAs were found in tidal tails and quasi-filamentary structures.

Pontzen et al. (2008) analysed DLAs in the galaxy formation simulations of Governato et al. (2007, 2008), Brooks et al. (2007). These simulations produce impressively realistic disk galaxies at $z = 0$. It is thus a major success that the simulations are able also to match $f(N, X)$ at $z = 3$, apart from a slight overprediction at high-N. The simulations also find good agreement with the distribution of metallicities in DLAs, which is something that previous simulations were unable to do. However, as before, the simulations cannot fully reproduce the velocity width data, producing too few high-v_w systems.

Tescari et al. (2009) once again investigated DLAs with SPH simulations, and were successful in reproducing $f(N, X)$ and the incidence rate (dN/dz), so long as strong winds are invoked. However, the simulations do not produce systems with v_w greater than 100 km/s. This is attributed to the fact that the simulations spread around the haloes small clumps of metals that are primarily in a wind phase, and thus not efficiently enriching the IGM. Tescari et al. thus suggest that small-scale turbulence or a pre-enrichment of the IGM (possibly by PopIII stars) may reconcile simulation and observation with regard to velocity widths.

In conclusion, the theoretical modelling of DLAs has produced some impressive results regarding the incidence and column densities of DLAs. In these models, DLAs represent protogalactic clumps in which gas has cooled within a merging hierarchy of dark matter haloes. However, the failure of all cosmological simulations to date to reproduce the velocity width distribution suggests that something is missing from these simulations. It could be a purely numerical effect, such as limited resolution or box size, or the consequence of missing physics. As always, observational evidence will provide important clues to guide theoretical modelling.

2.2 Lyman Alpha in Emission

Partridge & Peebles (1967) pointed out that Lyα emission should be an excellent tracer of young galaxies. While it was three decades before observational searches for Lyα emitters were successful, the detection of Lyα emission is now an important method for studying the high-redshift Universe. It is to this particular method that we turn our attention.

There are three general causes of Lyα emission, corresponding to the three ways in which a hydrogen atom can be placed in the $2\ ^2P$ state. The first is when an H$\textsc{i}$ atom in the ground state absorbs a Lyα photon. There are no other states between the $2\ ^2P$ and the ground state, and thus the re-emission of a Lyα photon is the most likely way for the atom to return to the ground state. When the probability of collisional de-excitation is negligible, the absorption and re-emission of Lyα photons by H$\textsc{i}$ can be thought of as a scattering process, and there is no net production or destruction of Lyα photons.

The other two ways are physically more interesting. A Lyα photon will be emitted when an electron drops into the $2\ ^2P$ state from a higher energy state and subsequently drops to the ground state. This higher energy state could be an $n \geq 3$ bound state, or a free state, meaning that we have a recombination producing a Lyα photon as follows:

$$e^- + H^+ \rightarrow H(2\ ^2P) + \text{photon} \rightarrow H(1\ ^2S) + Ly\alpha \qquad (2.8)$$
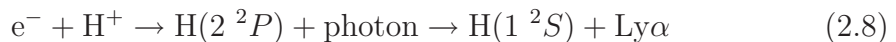
For atoms at $T = 10^4$ K, with only a weak dependence on temperature, $\sim 42\%$ of recombinations will pass through the $2\ ^2P$ state on their way to the ground state and produce a Lyα photon, while $\sim 38\%$ will go directly to the ground state and produce an ionising photon, and $\sim 20\%$ go to the $2\ ^2S$ state, producing 2 continuum photons in a forbidden transition to the ground state (Gould & Weinberg 1996).

Finally, an H$\textsc{i}$ atom can be placed in the $2\ ^2P$ state via collisional excitation. This case is summarised in Gould & Weinberg (1996). In short, most collisions at the relevant temperatures place the H$\textsc{i}$ atom in an $n = 2$ state: $\sim 25\%$ go to the $2\ ^2S$ and $\sim 75\%$ go to the $2\ ^2P$. Approximately 10% of the energy is lost to bremsstrahlung, meaning that $\sim 68\%$ of the thermal energy that is radiated away by collisional excitation is in the form of Lyα photons.

We will now consider these processes in astrophysical contexts. We can divide astrophysical sources of Lyα radiation into three broad categories. The first is star-forming galaxies: new stars that condense out of dense nebulae of hydrogen and helium in galaxies are expected to produce copious amounts of ionising radiation (Bromm et al. 2001). This ionising radiation will immediately encounter the H I in the surrounding ISM from which the star formed, producing H II. Upon recombination, Lyα photons are emitted $\sim 42\%$ of the time, as detailed above. If the surrounding medium is optically thick to ionising radiation, any ionising photon emitted as a result of a recombination will be quickly captured again, giving another chance to produce a Lyα photon. Thus, ionising photons are reprocessed, while Lyα photons are simply scattered. In this optically thick case, Lyα photons are emitted at $\sim 68\%$ of the rate at which the ISM absorbs ionising radiation. Because the Lyα line is narrow and strong, it should (in theory) provide a signature of primeval, high-redshift galaxies. In practice, the visibility of the line is affected by complications such as radiative transfer and dust, which we will discuss in the next section.

The second astrophysical source of Lyα radiation is gas that is cooling within dark matter haloes. This gas may radiate a substantial fraction of its gravitational energy via collisionally excited Lyα emission. Such a scenario was considered by Haiman et al. (2000), Fardal et al. (2001), Kereš et al. (2005). An important finding of these studies concerns the stage of the galaxy formation process when the infalling gas is supposedly shock-heated to the virial temperature of the halo, $\sim 10^6$ K. Gas at this temperature will cool primarily by emitting bremsstrahlung and He$^+$ line radiation. However, numerical simulations suggest that most of the gas that cools in galaxies, at all redshifts and summed over all masses (Kereš et al. 2009, Fig. 2), is never heated to the virial temperature. For example, Kay et al. (2000) find that only $\sim 10\%$ of SPH particles that end up in galaxies were ever heated above 10^5 K. Haiman et al. (2000) find that internal shocks are not likely to heat the gas above $\sim 6 \times 10^4$ K, where He$^+$ line cooling begins to dominate over Lyα cooling. Birnboim & Dekel (2003) and Kereš et al. (2005) found that gas accretes onto galaxies in two modes: a hot mode, where particles are heated to $T_{\rm vir} \sim 10^6$ K before cooling via bremsstrahlung and accreting onto the galaxy quasi-spherically; and a cold mode, where particles are never heated above $\sim 10^5$ K, cool by Lyα line emission and are usually accreted along filaments. The cold

mode dominates in low mass galaxies ($M_{\text{gal}} \lesssim 10^{10.3} M_\odot$), while the hot mode dominates in high mass systems. Fardal et al. (2001) estimate that Lyα emission accounts for 57% of cooling radiation, with just 2% coming from bremsstrahlung. While they find that the contribution to the Lyα luminosity from cooling radiation is less than that from massive star formation, the cooling radiation is produced at larger radii and is thus less likely to be extinguished by dust.

Lyα radiation from cooling gas can also be the result of photoheating — when an ionising photon has more than the 13.6 eV needed to remove the electron from its proton, the excess energy goes into the kinetic energy of the released electron. Thus, photoionisation can heat the gas, giving it another chance to emit Lyα photons as it cools.

A third source of Lyα emission is known as Lyα fluorescence: neutral hydrogen in the IGM will "glow" in Lyα as a result of being exposed to an external source of ionising radiation, such as the UV background. Observations of these Fluorescent Lyα Emitters (FLEs) hold great potential — they would allow us to directly image gas *outside* of galaxies, where most of the baryons are at high redshift. Further, for clouds that are optically thick to ionising radiation, the surface brightness of the fluorescent emission is set by the strength of the ionising background (Cantalupo et al. 2007). Thus, observations of Lyα fluorescence can measure accurately the intensity of the UV background at the Lyman limit, at least in principle.

We can summarise the above discussion as follows. There are three atomic processes that result in Lyα emission:

- A Lyα photon is absorbed; the only radiative transition back to the ground state is to re-emit a Lyα photon. Thus, Lyα photons scatter in an H\textsc{i} region.

- An electron drops to the $2\,^2P$ level from a higher bound state, or a free state. This includes the absorption of higher Lyman lines, and recombination.

- Hydrogen atoms are collisionally excited into the $2\,^2P$ level, and emit a Lyα photon.

The three main astrophysical causes of Lyα emission are:

- Ionising radiation from new stars and/or AGN illuminating the gas cloud from which they form.

- Cooling radiation, where gas releases its gravitational potential energy as it collapses into dark matter haloes. Other sources of heating can also power cooling radiation, including photoheating.

- Lyα fluorescence, where the UV background lights up neutral hydrogen in the IGM. (This can be thought of as a special case of the first scenario).

We will now review the current state of observations of Lyα, and the theoretical efforts to model this data.

2.2.1 Lyman Alpha Emitters (LAEs)

Following the theoretical work of Partridge & Peebles (1967), a number of groups attempted to find early galaxies via their redshifted Lyα emission. However, until rather recently they enjoyed no convincing successes — Djorgovski (1992), Thompson et al. (1995) note the lack of unambiguous detections of primeval galaxies. This in turn led to an increasing focus on finding alternative methods for discovering high redshift galaxies, such as the Lyman-break technique and selection criteria based on radio emission. As late as 1998, Cowie & Hu report the widespread belief that Lyα line searches have failed and should be abandoned in favour of colour-based searches.

The construction of 10m-class telescopes changed this situation very quickly. Lyα surveys have detected several hundred galaxies out to $z = 7$ (e.g. Steidel et al. 2000, Hu et al. 2002, Kodaira et al. 2003, Rhoads et al. 2004, Taniguchi et al. 2005, Kashikawa et al. 2006, Iye et al. 2006, Stanway et al. 2007), including Lyman Break galaxies and the host galaxies of damped Lyα systems (Fynbo et al. 1999, 2000). Future Lyα data will come from HAWK-I (Casali et al. 2006), which is already operational, and MUSE (Bacon et al. 2004).

The advantages of studying Lyα emission in young galaxies are that it is easily detected in both spectroscopic and imaging surveys, and that it mainly targets star-forming galaxies. This later point is an important one: LAEs are "normal" galaxies, selected primarily for their ability to make stars. This stands in contrast to other high-redshift galaxy samples, such as quasars and radio galaxies, which are selected on the basis of extreme phenomena such as AGN.

The properties of the population of LAEs are summarised in Nilsson & Meisenheimer (2009) and references therein. Gawiser et al. (2006), drawing on the

MUSYC samples of LAEs at $z \sim 3$, characterize a typical LAE as being small, blue and young with rapid star formation, low stellar mass, little dust obscuration, and signs of mergers.

There are a number of complications to the simple picture of early galaxies as star-driven Lyα beacons. One effect that could add to the Lyα luminosity of a star-forming galaxy is the presence of a central quasar, which provides another source of ionising photons. Haiman & Rees (2001) studied the effect of a quasar turning on within an assembling protogalaxy, and found that it would boost the Lyα emission in a spatially extended region dubbed "Lyα fuzz". Observations typically show that the fraction of LAEs associated with AGN is in the order of a few percent (Gawiser et al. 2006).

The very large cross-section of Lyα scattering means that radiative transfer effects are always relevant to Lyα emitters. A Lyα photon (at line centre) passing through an H I region with column density N_{HI} and temperature T encounters an optical depth of,

$$\tau_0 \approx 1.41 \left(\frac{T}{10^4 \ \mathrm{K}} \right)^{-\frac{1}{2}} \left(\frac{N_{\mathrm{HI}}}{10^{13} \ \mathrm{cm}^{-2}} \right). \tag{2.9}$$

With quasar absorption spectra frequently revealing H I regions with column densities N_{HI} of order $10^{16}-10^{22}$ cm^{-2}, extremely large optical depths of $\tau_0 = 10^3-10^9$ are likely to be encountered by the emitted Lyα photons. This is particularly true when ionising radiation is the source of Lyα photons. At temperatures of $\sim 10^4$ K, the optical depth of H I in Lyα is about 10^4 times larger than the optical depth at the Lyman limit (Osterbrock 1989, pg. 77). A Lyman limit photon that enters an H I region will be absorbed at a depth of $\tau_{LL} \sim 1$. When recombination produces a Lyα photon, this photon will find itself at an optical depth of $\tau_{\mathrm{Ly}\alpha} \simeq 10^4$. This means that computationally expensive radiative transfer calculations are required to trace the paths of Lyα photons through the ISM and IGM.

We will conclude this section with a summary of the factors that are relevant to Lyα radiative transfer in LAEs. Lyα radiative transfer is sensitive to the kinematics, geometry and ionisation state of H I, both inside and outside the galaxy in which the Lyα radiation was produced. Inside the galaxy, neutral hydrogen is expected to undergo a mixture of inflow due to gravitational collapse and outflow due to galactic winds. Dijkstra et al. (2006a) have studied the properties of Lyα emission that result from inflowing gas in haloes. Chapter 5 will summarise

and extend such models, so we will delay our discussion until then. Meanwhile, Verhamme et al. (2006) have studied Lyα radiative transfer in the context of an expanding shell geometry. Such models have been successful in reproducing the variety of Lyα line profiles found in LBG spectra (Schaerer & Verhamme 2008, Verhamme et al. 2008). The dominant effect in a shell geometry is the reflection of photons off the far side of the shell. Such photons are redshifted as a result of interaction with the receding gas, and can be far enough from line centre to pass unscattered through the front of the shell and thus escape to the observer. This results in an emission peak at a velocity that is *twice* the expansion velocity of the shell.

Dust can be a very important factor in Lyα radiative transfer. The long random walk undertaken by a typical Lyα photon in an H I region means that it is especially vulnerable to dust extinction (Neufeld 1990, Charlot & Fall 1991). On the one hand, since stars themselves produce the metals that make up dust, primeval galaxies undergoing their first burst of star formation are not expected to contain dust. On the other hand, the first stars were very massive and thus produced metals on a short time-scale — super-solar metallicities have been observed in the highest redshift quasars at $z \sim 6$ (Pentericci et al. 2002). Thus, it is likely that the "dust-free" epoch in the life of a primeval galaxy is short-lived. It was thought that dust extinction could account for the early failures to detect primeval galaxies through their Lyα emission. However, Giavalisco et al. (1996) showed that dust content (as inferred from metallicity or submillimetre emission) is not strongly correlated with Lyα equivalent width, implying a decoupling between the extinction of continuum and resonant-line photons. Neufeld (1991) and Hansen & Oh (2006) present an intriguing scenario to explain this. Consider, instead of a uniform mix of H I and dust, a clumpy medium consisting of dusty H I clouds and a largely empty InterCloud Medium (ICM). Then, when a Lyα photon encounters a cloud, it will be efficiently reflected by resonant H I scattering, returning to the dustless ICM. Meanwhile, continuum photons are not reflected at the surfaces of the clouds and suffer extinction from the dust inside.

Theoretical predictions of the properties of high-redshift LAEs need to take into account the possible interaction of escaping Lyα photons with the IGM, which introduces a significant source of uncertainty. As a simple starting point, Loeb & Rybicki (1999) consider Lyα propagating through a neutral IGM with

a pure Hubble flow velocity field. They find that the scattering of Lyα photons means that these sources appear more spatially extended in the Lyα line than in the continuum to the red of the line. Further, photons to the blue of the line will be progressively redshifted into resonance as they propagate, resulting in a redshifted Lyα line. The velocity structure of the IGM will also contain a contribution from outflow (due to winds) and infall onto galaxies. Dijkstra et al. (2007), for example, note that the infall of gas in the IGM onto galaxies will occur out to distances well beyond the virial radius. This has the effect of scattering the red side of the Lyα line. Santos (2004) study a model where the gas in the IGM is completely neutral at $z \approx 6.5$, is infalling close to the galaxy and returns to the Hubble flow at large distances, concluding that Lyα luminosity can be reduced by an order of magnitude and significantly redshifted.

The ionisation state of the IGM is also very relevant. Consequently, LAEs may be able to probe the epoch of reionisation, when ionising radiation from stars and quasars ionised the IGM. In essence, we are using the LAE as a light bulb that illuminates the Hi fog of the surrounding IGM (Loeb & Rybicki 1999). A number of studies have discussed this possibility (Loeb & Rybicki 1999, Santos 2004, Dijkstra et al. 2007, McQuinn et al. 2007). In particular, McQuinn et al. (2007) notes that bubbles of ionised hydrogen will affect the *measured* clustering of LAEs — as reionisation proceeds, larger Hii bubbles will form and more LAEs will appear out of the dark. This will produce a rapid decrease in the observed number density of LAEs with redshift, which would be difficult to attribute to the evolution of the intrinsic properties of LAEs.

2.2.2 LAE and Lyman Break Galaxies (LBG)

Searches for high redshift galaxies using the redshifted Lyα line have proved very successful, providing large samples of star-forming galaxies. Before moving on from LAEs, it is worthwhile to consider their relationship to high redshift galaxies discovered using other methods. In particular, we will consider Lyman Break Galaxies.

Partridge & Peebles (1967) predicted that primordial galaxies have a sharp cut-off in intensity at the Lyman limit. Recall that the Lyα photons emitted by star-forming galaxies are at the expense of ionising photons, so that their
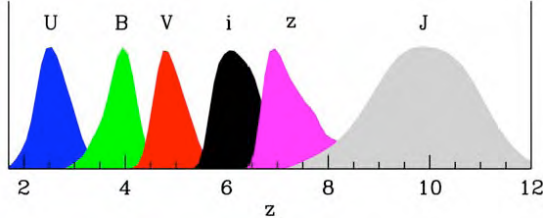
Figure 2.4: The redshift range searched by the Lyman-break technique using the different filters as labelled in the figure. Figure taken from Illingworth & Bouwens (2005)

spectra are likely to be lacking in photons energetic enough to ionise hydrogen. There is an additional spectral feature at high redshift that is very important — the intervening Lyα forest will dim the continuum between the Lyman limit and Lyα frequencies. If we then observe galaxies using photometric filters that are sensitive to light from either side of these features, high redshift galaxies will "drop-out" of the images taken through the highest frequency filters. This provides an approximate photometric redshift that can be followed up spectroscopically.

Most early Lyman-break searches looked for objects that were not visible in U-band images (but were visible at longer wavelengths). This U-dropout technique has since been correspondingly expanded into include B-dropouts, V-dropouts etc, that cover higher redshift ranges. A diagram of the redshift ranges searched by different photometric bands is found in Figure 2.4. Daddi et al. (2004) showed that IR bands can extend such colour-based methods into the redshift range $1.4 < z < 2.5$. Adelberger et al. (2004) showed that other spectral features (such as the Balmer break) can be used to probe redshifts of $z \sim 2$, with selection criteria chosen to identify galaxies with approximately the same intrinsic properties (UV luminosity, reddening by dust) as the $z \sim 3$ LBGs. These surveys have yielded large and well-controlled samples of star-forming galaxies. For a more complete review, see Giavalisco (2002).

Since the Lyman break and Lyα emission are physically related, it is likely that there is a relationship between the LAE and LBG populations. Naively, we would expect the two methods to choose members of the same underlying population — primeval star-forming galaxies. However, each method has its own selection bias: LAE surveys consider only emitters with a relatively large Lyα equivalent width, but are sensitive to objects with fainter continuum emission than LBG surveys. Systematic comparisons of the properties of the two populations are found in Steidel et al. (2000), Shapley et al. (2001, 2003), Pentericci et al. (2007), Kashikawa et al. (2007). We will present a brief summary here.
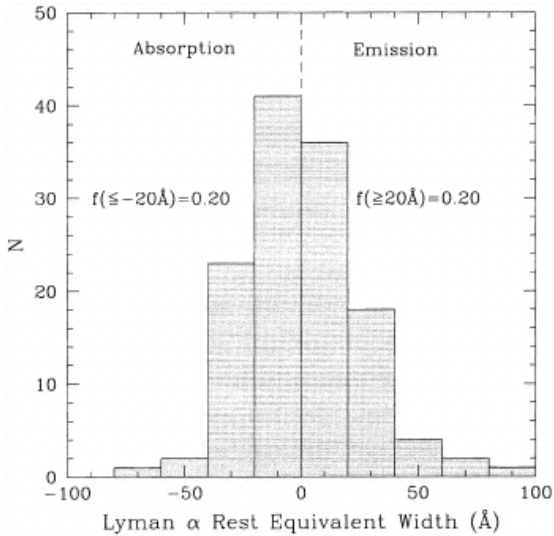
Figure 2.5: Distribution of spectroscopically measured Lyα rest equivalent widths of LGBs, taken from Steidel et al. (2000). Later studies are consistent with the fractions shown (e.g. Shapley et al. 2003, Pentericci et al. 2007). About 20% of LBGs have sufficient Lyα emission to be detected in a Lyα survey. The median Lyα equivalent width is near zero, indicating that LBGs are just as likely to be Lyα absorbers as emitters.

Figure 2.5 shows the Lyα properties of LBGs, in the form of the distribution of Lyα rest equivalent widths. The most interesting feature is that the median Lyα equivalent width is near zero, indicating that LBGs are just as likely to be Lyα absorbers as emitters.

To study a possible evolutionary link between LAEs and LBGs, a number of groups have studied how the Lyα properties of LBGs vary with age. Shapley et al. (2001) reported that young galaxies have significantly dustier interstellar media than more mature LBGs. They concluded that their sample of young galaxies contains objects with large star formation rates, where large amounts of dust obscure the sites of star formation. As time passes, this dust is either destroyed or blown out by large-scale outflows (or both), resulting in lower extinction and thus a larger Lyα luminosity. Thus, LBGs supposedly evolve into LAEs. Shapley et al. (2003) reiterated this conclusion, emphasising the importance of large-scale outflows in explaining many of the trends seen in LBGs. However, Pentericci et al. (2007, and references therein) reach the opposite conclusion: LBGs with Lyα emission are on average much younger than LBGs without Lyα emission. They propose that galaxies begin as LAEs with strong Lyα emission and then evolve into LBGs as dust extinguishes the Lyα line. Because of this tension, some authors have suggested that there are two Lyα emission phases — an early phase before significant dust has built up in the ISM, and a later phase, when galactic

winds aid the escape of Lyα (Thommes & Meisenheimer 2005). Such models await observational testing.

2.2.3 Fluorescent Lyman Alpha Emitters (FLEs)

Hogan & Weymann (1987) predicted that the UV ionising background falling on clouds of H<small>I</small> in the IGM would produce detectable Lyα fluorescence. This emission would allow us to study the size and morphology of these clouds. Such information cannot be gleaned from H<small>I</small> absorption in quasar spectra, as they are one-dimensional probes, while observations of galaxies probe only the densest regions of the Universe. Furthermore, cosmological structure simulations predict that the IGM is characterized by diffuse, sheet-like, and filamentary structures, meaning that 3D information is crucial in testing these models. Fluorescent emission has the potential to map the full structure of the cosmic web.

The calculations of Hogan & Weymann (1987) were refined by Gould & Weinberg (1996), who correctly predicted that detecting FLEs would be difficult even with a 10m telescopes; Cantalupo et al. (2007) report that despite the observational efforts of themselves and others in finding a handful of plausible candidates, there is still some doubt about whether FLEs have actually been detected.

Recently, more sophisticated models of FLEs have been developed. Cantalupo et al. (2005) modelled FLEs as follows. They first perform a hydrodynamic simulation of structure formation to compute the distribution of baryons in the Universe at $z \sim 3$. They then incorporate two radiative transfer schemes: one to propagate ionising radiation through the simulation, allowing the computation of the H<small>I</small> distribution and recombination rate, and a Monte Carlo code to follow the paths of the Lyα photons. They consider the case of uniform ionising radiation from the UV background, and also consider the effect of ionising flux from a nearby quasar. In the absence of a nearby quasar, they find that the simple models of Hogan & Weymann (1987) and Gould & Weinberg (1996) overestimate the Lyα flux because they assumed a static configuration of H<small>I</small>. For a realistic model of the IGM, there will be velocity gradients that affect different parts of the spectrum. This "velocity-field effect" is found to reduce the overall Lyα flux by $\sim 25\%$ compared to the static case. In the presence of ionising radiation from a quasar, there is an additional "geometric effect" — previous models used the

simple geometry of a slab to represent the self-shielding layer where Lyα is produced, beneath which ionising photons cannot penetrate. The assumption was that this layer would be small compared to the rest of the cloud. However, the quasar's strong ionising flux means that the shielding layer is very deep along the quasar direction, so that a slab model is not a good approximation. The result is that more Lyα photons are emitted perpendicular to the direction of the quasar than is the case assuming a slab geometry.

A similar study was conducted more recently by Kollmeier et al. (2009), tracing Lyα fluorescence photons through SPH simulations. Figure 2.6 illustrates some of their results: the top panels show the emitted (pre-scattering) Lyα surface brightness (left) and spectrum (right). The bottom panels show the effect of scattering by neutral hydrogen. The figure illustrates that the scattering of Lyα photons by H I makes the spatial surface brightness distribution more diffuse, and the spectrum broader.

Currently, a number of groups are trying to make the first definite detection of fluorescent Lyα emission from the IGM. Success is hopefully not far away.

2.2.4   Lyman Alpha Blobs (LABs)

While most high redshift Lyα emitting objects appear pointlike, there is a small class of objects that have been discovered that are extremely luminous, very large ($\sim 10 - 150$ kpc) and radio quiet. They are also rather rare, with a number density of $\sim 10^{-3.8}$ comov.Mpc^{-3} (Dijkstra & Loeb 2009), as compared to $\sim 10^{-2.7}$ comov.Mpc^{-3} for the population of Lyα emitters in van Breukelen et al. (2005). These objects have been dubbed "Lyα Blobs" (LABs) and have been studied extensively (Fynbo et al. 1999, Keel et al. 1999, Steidel et al. 2000, Francis et al. 2001, Palunas et al. 2004, Matsuda et al. 2004, Chapman et al. 2004, Bower et al. 2004, Villar-Martín et al. 2005, Dey et al. 2005, Matsuda et al. 2006, Nilsson et al. 2006). In spite of this, their physical nature remains mysterious, and it is not clear where they stand in relation to the astrophysical sources of Lyα outlined above. There are three mechanisms suggested as the energy source for LABs.

- Obscured ionising sources: LABs are the Lyα fuzz predicted by Haiman & Rees (2001), or the Lyα coronae predicted by Furlanetto et al. (2005). In other words, LABs contain obscured sources of ionising radiation in the
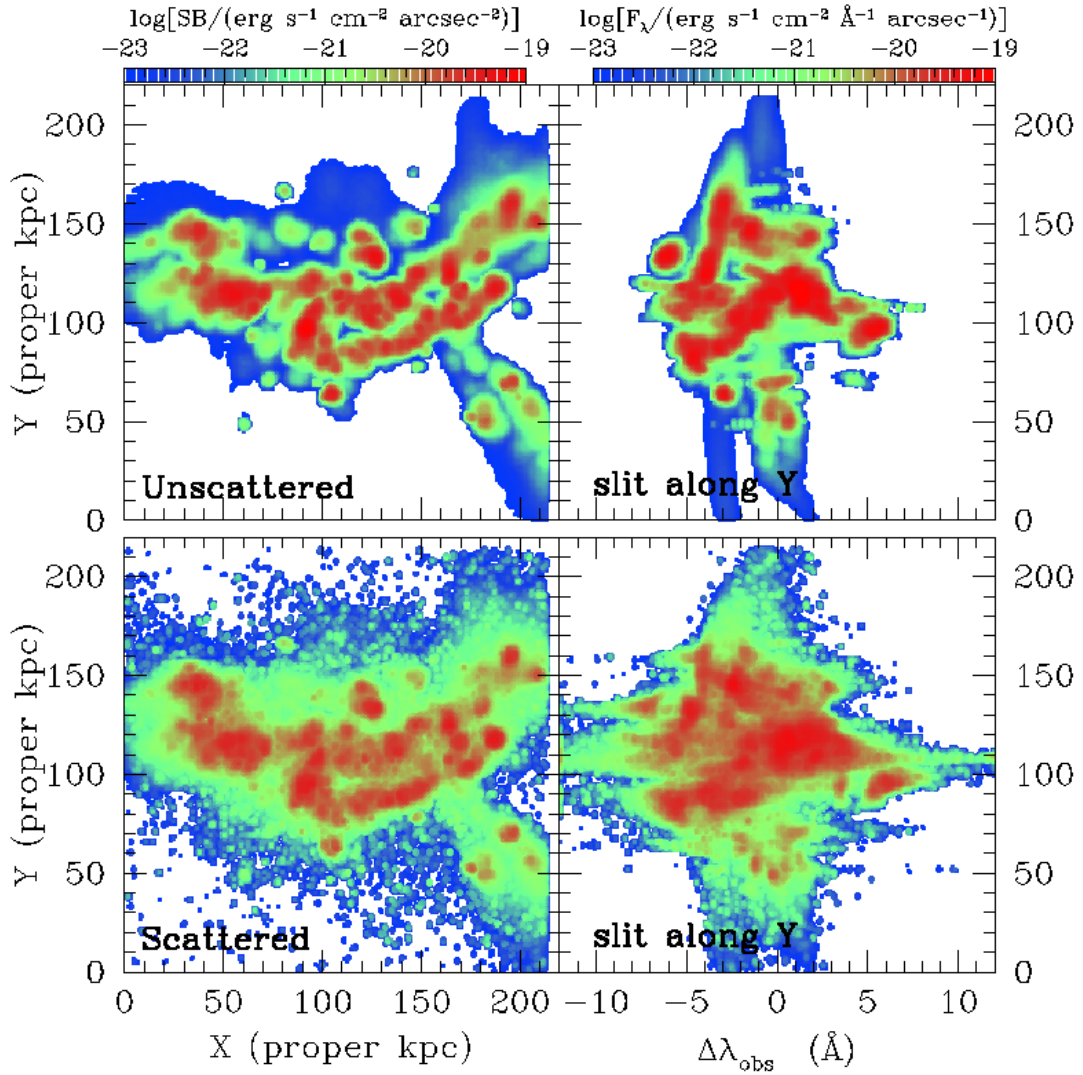
Figure 2.6: A Lyα map of a simulation of a cosmological volume at $z = 3$ by Kollmeier et al. (2009). The top panels are the emitted (pre-scattering) Lyα surface brightness (left) and spectrum (right). The bottom panels show the effect of scattering by neutral hydrogen.

form of an AGN or star-forming galaxy. This is the scenario suggested, for example, by the multiwavelength study of an LAB carried out by Chapman et al. (2004),

- Cooling radiation: LABs consist of gas that is radiating away its gravitational potential energy as it cools into massive galaxies (Haiman et al. 2000, Fardal et al. 2001, Birnboim & Dekel 2003, Kereš et al. 2005, Sommer-Larsen 2005, Dijkstra et al. 2006a,b, 2007, Dijkstra & Loeb 2009). This scenario is also known as cold accretion, and is argued for observationally by Nilsson et al. (2006).

- Galactic superwinds: starburst activity results in enough supernova to sweep cooling, dense, radiating shells of H I into the IGM (Taniguchi & Shioya 2000, Mori et al. 2004), a scenario favoured observationally by Ohyama et al. (2003).

In reality, LABs will almost certainly be powered by a combination of these sources. The question remains as to which one dominates.

Extended Lyα emission is also associated with another population of high redshift galaxies — radio galaxies. Selecting sources by their radio emission generally finds the most massive high redshift objects, either galaxies or AGN. Giant Lyα haloes (or nebulae) have been discovered around many radio galaxies, and their properties have been studied by Reuland et al. (2003), Villar-Martín et al. (2005), van Breugel et al. (2006), Villar-Martín et al. (2007a), Geach et al. (2007), Villar-Martín et al. (2007b). These objects resemble LABs, except that they are radio loud, have a higher surface brightness (by a factor of ~ 5) and contain large, multi-component galaxies (van Breugel et al. 2006). Reuland et al. (2003) have suggested the following evolutionary sequence: LABs represent the very first stage in the formation of a large galaxy (or a set of smaller galaxies that later merge), and evolve into radio-loud Lyα haloes when galaxy merging triggers an AGN. Thus, Lyα emission is able to probe the environment and evolution of radio galaxies and AGN.

2.2.5 The Faint Lyα Emitters of Rauch et al.

Rauch et al. (2008) carried out an ultra-deep spectroscopic survey for low surface brightness Lyα emitters at redshift $z \sim 3$. A 92-hour long exposure with the
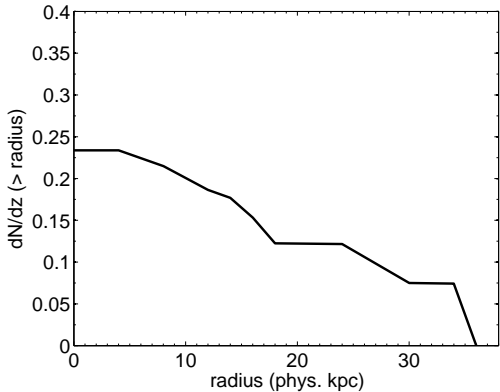
Figure 2.7: The size distribution of the population of faint Lyα emitters discovered by Rauch et al. (2008, fig. 19). The data have been corrected for slit losses — adopting the extent along the slit for the diameter of the object will underestimate its real diameter if the slit is not centred on the object. The spatial resolution limit is ~ 4.5 physical kpc.

ESO VLT FORS2 instrument yielded a sample of 27 faint line emitters with fluxes of a few times 10^{-18} erg s^{-1}cm^{-2}. Based on their large number density, they argue that the sample is dominated by Lyα emitters, rather than low redshift interlopers. The most important results of the survey are the size distribution, in the form of incidence rate as a function of the observed radius $dN/dz(> r)$, and the luminosity function. These are shown in Figures 2.7 and 2.8.

The size distribution shows that the Lyα emission typically extends to tens of kpc. The rapid decline in $dN/dz(> r)$ at $r \sim 35$kpc is most probably an artefact of slit losses, in combination with the effects of a finite survey volume. The total incidence rate is $dN/dz = 0.23$, which is remarkably similar to the incidence rate of DLAs, for which $dN/dz|_{\mathrm{DLA}} = 0.26$.

The luminosity function shows a rather steep decline in the number density above 10^{41} erg s^{-1}. The flattening below this value is strongly affected by the sensitivity limits of the observations and thus needs to be interpreted with caution. Rauch et al. (2008) claim that the emission is most likely powered by star formation at rates of $0.07 - 1.5 M_\odot \mathrm{yr}^{-1}$. In particular, they claim that Lyα fluorescence and cooling radiation are unable to produce the observed luminosities. We will return to this claim in Chapter 4.

A number of lines of evidence led Rauch et al. (2008) to claim that the emitters that they have discovered are the long sought host galaxies of DLAs. These are:

- Both must be extended, optically thick neutral hydrogen.

- The similarity between the incidence rate (dN/dz) for the emitters and for
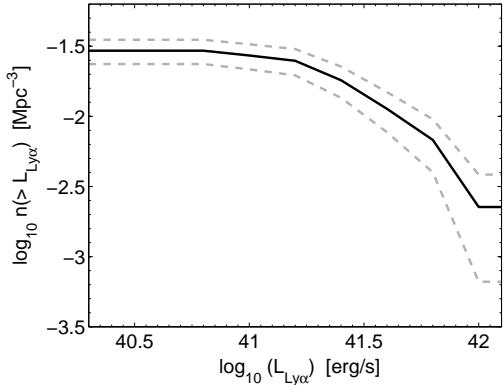
Figure 2.8: The comoving number density of emitters with luminosity exceeding $L_{\text{Ly}\alpha}$, from the observations of Rauch et al. (2008, fig. 9), assuming that they are all Lyα emitters.

DLAs — the combination of the large sizes and high space density of the emitters mean that they can account for the high incidence rate of DLAs.

- Low star formation rate, which explains the low success rate for direct searches for the counterparts of DLAs and the low observed metallicity of DLAs.

- Low dust content, assuming that a high dust content would extinguish the line.

- If the large sizes of the emitters are due to radiative transfer effects (which seems likely given that Wolfe & Chen (2006) placed strict upper limits on *extended* star formation in DLAs), then the emitters must contain significant amounts of neutral hydrogen, the majority of which resides in DLAs.

If these emitters really are the host population of DLAs, then these observations give us — for the first time — a way of directly observing the dominant reservoirs of neutral, star-formation-feeding gas in the early Universe. However, many of the conclusions of Rauch et al. (2008) are speculative. More realistic and sophisticated models are required, and it is to such modelling that we now turn.

Chapter 3

Lyman Alpha Radiative Transfer

Some of the contents of this chapter have been submitted for publication in Monthly Notices of the Royal Astronomical Society, as an appendix to *Faint extended Lyα emission due to star formation at the centre of high column density QSO absorption systems* (see Chapter 5).

The resonant nature of the Lyα transition makes the problem of radiative transfer through neutral hydrogen non-trivial. Lyα photons will typically undergo many scatterings before escaping an HI region, diffusing in both real and frequency space. The properties of the emergent radiation depend sensitively on the spatial distribution, kinematics, temperature and dust content of the gas.

Studies of the radiative transfer of Lyα have a long history. The first investigations employed approximate calculations and simple physical arguments (Zanstra 1949, Unno 1952, Osterbrock 1962, Adams 1971, 1972). Later, analytic solutions were found for simple geometries in the limit of large optical depth (Harrington 1973, Neufeld 1990). It was soon realised that Monte Carlo simulations provided the most flexible method for investigating arbitrary geometries, density distributions, and velocity structures. Many investigations have employed such techniques: Avery & House (1968), Auer (1968), Caroff et al. (1972), Panagia &

Ranieri (1973), Bonilha et al. (1979), Natta & Beckwith (1986), Ahn et al. (2000, 2001, 2002), Zheng & Miralda-Escudé (2002), Cantalupo et al. (2005), Hansen & Oh (2006), Tasitsiomi (2006), Verhamme et al. (2006), Dijkstra et al. (2006a, hereafter DHS06), Laursen et al. (2009a).

In this chapter, we will outline the algorithm for a Monte-Carlo Lyα radiative transfer code. We will then present tests of our implementation of the code.

3.1 Lyα Radiative Transfer (RT) Algorithm

The basic idea of a Monte-Carlo radiative transfer algorithm is to create a photon and propagate it in a random direction for a certain distance (that depends on the optical depth), at which point the photon will interact with an atom. After the interaction, the photon will have a new frequency and a new direction. We repeat until the photon escapes the system. The details of each step in our Monte Carlo code for Lyα RT are outlined below — throughout, R_i (for $i = 1, 2, 3, \ldots$) denotes a random number generated uniformly between 0 and 1.

1. We begin by specifying, as a function of position $\boldsymbol{r}$,

   - $n_{\mathrm{HI}}(\boldsymbol{r})$, the number density of HI,

   - $\epsilon(\boldsymbol{r})$, the Lyα emissivity (in photons/s/cm^3),

   - $\boldsymbol{v}_{\mathrm{b}}(\boldsymbol{r})$, the bulk velocity field of HI, and

   - $T(\boldsymbol{r})$, the temperature of HI.

2. We generate a photon at an initial position $\boldsymbol{r}_i$ according to the emissivity. We then choose the photon's initial direction $\hat{\boldsymbol{n}}$ from an isotropic distribution,

$$\hat{\boldsymbol{n}} = (\sin\theta\cos\phi, \sin\theta\sin\phi, \cos\theta), \qquad (3.1)$$

where,

$$\theta = \cos^{-1}(2R_1 - 1) \qquad \text{(the polar angle)}, \qquad (3.2)$$

$$\phi = 2\pi R_2 \qquad \text{(the azimuthal angle)}. \qquad (3.3)$$

We generate the photon's initial frequency as follows. The emission (and absorption) profile in the rest frame of the emitting atom is assumed to be Lorentzian,

$$\phi_{\mathrm{L}}(\nu) = \frac{\Delta\nu_{\mathrm{L}}/2\pi}{(\nu - \nu_0)^2 + (\Delta\nu_{\mathrm{L}}/2)^2},\tag{3.4}$$

where $\nu_0 = 2.47{\times}10^{15}$ Hz is the central Lyα frequency and $\Delta\nu_{\mathrm{L}} = 9.936{\times}10^7$ Hz is the natural line width. We take into account the thermal Doppler broadening with a Maxwell-Boltzmann distribution of the velocity of the scattering atoms. The line profile can then be written as an average of the Lorentz profile over the atoms' velocities,

$$\phi(\nu) = \int_{-\infty}^{\infty} \phi_{\mathrm{L}}\left(\nu - \frac{\nu_0 v_z}{c}\right) \frac{1}{v_{\mathrm{th}}\sqrt{\pi}} \exp\left(-\frac{v_z^2}{v_{\mathrm{th}}^2}\right) \, \mathrm{d}v_z \tag{3.5}$$

$$\Rightarrow \phi(x) = \frac{1}{\Delta\nu_{\mathrm{D}}\sqrt{\pi}} H(a, x),\tag{3.6}$$

where the argument of ϕ_{L} takes into account the Doppler shift in the frequency of the photon as seen by an atom with velocity component v_z in the direction of the photon's motion. The other quantities are

$$v_{\mathrm{th}} = \left(\frac{2kT}{m}\right)^{1/2} = 12.85 \text{ km s}^{-1} \left(\frac{T}{10^4 \text{ K}}\right)^{\frac{1}{2}},\tag{3.7}$$

$$a = \frac{\Delta\nu_{\mathrm{L}}}{2\Delta\nu_{\mathrm{D}}} = 4.693 \times 10^{-4} \left(\frac{T}{10^4 \text{ K}}\right)^{-\frac{1}{2}},\tag{3.8}$$

$$\Delta\nu_{\mathrm{D}} = \left(\frac{v_{\mathrm{th}}}{c}\right) \nu_0,\tag{3.9}$$

$$x = \frac{\nu - \nu_0}{\Delta\nu_{\mathrm{D}}},\tag{3.10}$$

the thermal velocity dispersion (times $\sqrt{2}$), relative line width, Doppler frequency width and frequency displacement in units of $\Delta\nu_{\mathrm{D}}$, respectively. We will use x as our frequency variable. We have also made use of the Voigt function,

$$H(a, x) \equiv \frac{a}{\pi} \int_{-\infty}^{\infty} \frac{e^{-y^2}}{(x - y)^2 + a^2} \, \mathrm{d}y.\tag{3.11}$$

The Voigt function can be approximated as a Doppler core and Lorentz wings,

$$H(a, x) \sim \begin{cases} e^{-x^2} & \text{core, } |x| < x_c, \\ \frac{a}{\sqrt{\pi} x^2} & \text{wing, } |x| > x_c. \end{cases} \tag{3.12}$$

The transition between the two occurs at a 'critical' frequency x_c, defined as the solution to $e^{-x_c^2} = a/\sqrt{\pi} x_c^2$. For $T = 10^4$ K, we have $x_c \approx 3.255$. We will use the approximation to the Voigt function given in Tasitsiomi (2006).

Equation (3.5) assumes that the "laboratory frame" (in which we are measuring the photon's frequency) is the same as the fluid rest frame. In order to take account of the bulk fluid velocity, we replace the frequency in the lab frame, x, with the frequency as seen by the fluid,

$$\bar{x} = x - \frac{\boldsymbol{v}_{\mathrm{b}} \cdot \hat{\boldsymbol{n}}}{v_{\mathrm{th}}}. \tag{3.13}$$

In practice, the photons are very likely to be emitted close to line-centre, and because a typical photon suffers a large number of resonant scatterings, any "memory" of the initial frequency is quickly erased (DHS06). Thus, we will usually inject all photons at line-centre in the fluid frame ($\bar{x} = 0$).

3. The distance travelled depends on the optical depth. The probability that the photon propagates a physical distance corresponding to an optical depth between τ and $\tau + \mathrm{d}\tau$ is $e^{-\tau} \mathrm{d}\tau$. We choose an optical depth for the photon from this distribution,

$$\tau = -\ln(R_3). \tag{3.14}$$

To find the physical distance travelled, we perform the following line integral, solving for s_f,

$$\tau = \int_0^{s_f} \sigma_x(\boldsymbol{r}(s)) \, n_{\mathrm{HI}}(\boldsymbol{r}(s)) \, \mathrm{d}s, \tag{3.15}$$

where $\boldsymbol{r}(s) = \boldsymbol{r}_i + \hat{\boldsymbol{n}} s$ is the path travelled by the photon, σ_x is the scattering cross-section of Lyα photons,

$$\sigma_x = f_{12} \pi c r_e \phi(x), \tag{3.16}$$

$f_{12} = 0.4167$ is the Lyα oscillator line strength, and $r_e = 2.81794 \times 10^{-13}$ cm is the classical electron radius. It is worth noting how the integrand depends on position. The most obvious dependence is that of a spatially varying number density $n_{\text{HI}}(\boldsymbol{r})$. The dependence of σ_ν is two-fold. Firstly, in case of a spatially-varying bulk velocity, $\sigma_\nu(\phi(\bar{x}(\boldsymbol{v}_{\text{b}}(\boldsymbol{r}))))$. Secondly, if T depends on position, then so will both x and a in $\phi(x)$ via $\Delta\nu_{\text{D}}$ and v_{th}.

Once s_f is found, the position of the next scattering is $\boldsymbol{r} = \boldsymbol{r}_i + \hat{\boldsymbol{n}}s_f$. If this is outside the HI region, then the algorithm is terminated.

4. Next, we choose the velocity of the scattering atom. Naïvely, one might think that this step involves generating the three components of the atom's velocity from the Maxwell-Boltzmann distribution. However, we are choosing the velocity of an atom *given* that it scatters a photon with frequency x. We can therefore divide the velocity of the atom into one component parallel ($v_{\text{\textbardbl}}$) and two components perpendicular to the direction of motion of the photon ($v_{\perp 1}$, $v_{\perp 2}$). The two perpendicular components do not alter the frequency of the photon as seen by the atom, and are thus chosen from a Maxwell-Boltzmann distribution. From Equations (3.5)-(3.11) it can be seen that the probability that a photon with frequency x scatters off an atom with velocity (along the direction of propagation of the photon) between $v_{\text{\textbardbl}}$ and $v_{\text{\textbardbl}} + \mathrm{d}v_{\text{\textbardbl}}$ is,

$$f(u_{\text{\textbardbl}}) \, \mathrm{d}u_{\text{\textbardbl}} = \frac{a}{\pi} \frac{e^{-u_{\text{\textbardbl}}^2}}{(x - u_{\text{\textbardbl}})^2 + a^2} \frac{1}{H(a, x)} \, \mathrm{d}u_{\text{\textbardbl}}, \qquad (3.17)$$

where $u_{\text{\textbardbl}} = v_{\text{\textbardbl}}/v_{\text{th}}$. A scheme for generating random numbers from this distribution is given in Zheng & Miralda-Escudé (2002), who use a rejection method (Press et al. 1992) with two comparison functions for greater efficiency. Zheng & Miralda-Escudé (2002) do not specify the function $u_0(x, a)$, which defines the joining point of the functions. We have found that the following function gives satisfactory results,

$$u_0(x, a) = \begin{cases} \frac{x}{1.01 + x/210 + x^2/105} & \text{for } |x| < 5, \\ 5 \exp\left(-\left(\frac{0.088x}{\sqrt{a}}\right)^{-0.36}\right) & \text{for } |x| \geq 5. \end{cases} \qquad (3.18)$$

5. Now that we have calculated $\boldsymbol{v}_a$, the velocity of the atom that scatters the photon, we perform a Lorentz transform into the rest frame of the atom. In this frame, we assume that the frequency of the scattered photon differs from the frequency of the incident photon only by the recoil effect (Rybicki & Lightman 1979, pg. 196). We choose a new direction for the photon. Our code can incorporate either an isotropic or a dipole distribution for the direction of the re-emitted photon; the results are often insensitive to the choice. For a dipole distribution, the new direction ($\mu = \hat{\boldsymbol{n}} \cdot \hat{\boldsymbol{n}}_f$) is chosen by solving,

$$R_4 = \frac{3}{8} \int_{-1}^{\mu} (1 + \mu') \, \mathrm{d}\mu', \tag{3.19}$$

which is a cubic polynomial with solution,

$$\mu = (A + B)^{\frac{1}{3}} - (A - B)^{\frac{1}{3}}, \qquad B = 4R_4 - 2, \; A = \sqrt{B^2 + 1}. \tag{3.20}$$

We then transform back into the laboratory frame. At speeds much less than c, for an initial photon direction $\hat{\boldsymbol{n}}$, and having chosen a final photon direction $\hat{\boldsymbol{n}}_f$, we find that the final frequency of the photon is,

$$x_f = x - \frac{\hat{\boldsymbol{n}} \cdot \boldsymbol{v}_a}{v_{\mathrm{th}}} + \frac{\hat{\boldsymbol{n}}_f \cdot \boldsymbol{v}_a}{v_{\mathrm{th}}} + \frac{h \Delta \nu_{\mathrm{D}}}{2kT}(\hat{\boldsymbol{n}} \cdot \hat{\boldsymbol{n}}_f - 1). \tag{3.21}$$

In general, the final term, known as the recoil term (Adams 1971), is negligible for our modelling.

We now return to step 3 and repeat until the photon escapes the HI region.

Once the photon escapes the region, its properties (frequency, angle of escape etc.) are recorded. We then return to step 2 and generate another photon.

The code incorporates the presence of a cosmic abundance of deuterium, following the method presented in DHS06. This has only a minimal effect on the results.

3.1.1 Accelerating the Code

Monte Carlo Lyα RT codes can be significantly accelerated by skipping scatterings in the core of the line profile. We define the core-to-wing transition to occur at a critical frequency x_{crit}, which is not the same as x_c. Whenever a photon is in

the core $|x| < x_{\mathrm{crit}}$, we force it into the wing by choosing the scattering atom's velocity to be large. We follow the method presented in Ahn et al. (2002) and DHS06, choosing the perpendicular components of the atom's velocity such that $u_{\perp 1}^2 + u_{\perp 1}^2 \geq x_{\mathrm{crit}}^2$.

We choose the value of x_{crit} by requiring that, for a uniform sphere, less than a fraction f of the photons that emerge have $|x| < x_{\mathrm{crit}}$. Using the analytic solution for the emergent spectrum of a sphere (DHS06, Equation (9)), this gives,

$$x_{\mathrm{crit}} = \left(\sqrt{\frac{54}{\pi^3}} a\tau_0 \tanh^{-1} f \right)^{\frac{1}{3}}, \tag{3.22}$$

where τ_0 is the line-centre optical depth from the centre to the edge. We find that setting $f = 0.01$ up to $\max(x_{\mathrm{crit}}) = 3 \ (\approx x_c)$ gives an acceptable compromise between speed and accuracy.

3.1.2 Spherically Symmetric Shells

In cases where n_{HI}, T and/or $\boldsymbol{v}_{\mathrm{b}}$ have a complicated dependence on $\boldsymbol{r}$, solving for s_f in Equation (3.15) can be computationally expensive. In spherical symmetry, we use a similar approach to DHS06, dividing the sphere into uniform shells. Within each shell, the integral (3.15) becomes trivial, $\tau = s_f \sigma_x n_{\mathrm{HI}}(r_{\mathrm{shell}})$. If the photon encounters a shell edge, the optical depth to the edge of the shell is subtracted from τ and a new s_f is calculated using the new value of r_{shell}. We space the shells so that each shell has equal column density. We choose the number of shells to keep the frequency dispersion within each shell small compared to the jump in frequency as the photon crosses a shell; 1000 shells are usually sufficient.

3.2 Testing the Code

It is important to test our implementation of the Lyα radiative transfer algorithm. We can do this against a range of analytical solutions found in the literature.

3.2.1 The Redistribution Function

Hummer (1962) calculated the redistribution function for the case of coherent scattering in the atom's frame with radiation damping (i.e. incorporating the
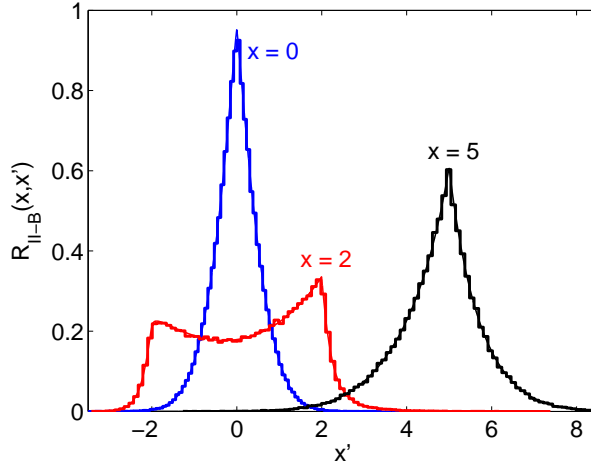
Figure 3.1: The redistribution function $R_{\text{II-B}}(x, x')$ gives the probability that a photon, whose frequency prior to absorption was x, is re-emitted with frequency in the range $[x', x' + \mathrm{d}x']$. The thin, smooth curve is the analytic solution and the thick histogram is the output from our code for $x = 0, 2, 5$ (blue, red, black respectively), and $T = 10$ K ($a = 0.0149$). The two lines are indistinguishable.

Lorentzian natural line width). The result (Equation 3.12.2 of Hummer (1962)) is $R_{\text{II-B}}(x, x') \, \mathrm{d}x'$, defined as the probability that a photon, whose frequency prior to absorption was x, is re-emitted with a frequency in the range $[x', x' + \mathrm{d}x']$. Comparing the results of our code with this function provides an excellent test of our implementation of the scattering of the atom, especially the calculation of $u_{\shortparallel}$.

The comparison of the analytic formula with the output of our code is found in Figure 3.1. The thin, smooth curve is the analytic solution and the thick histogram is the output from our code for $x = 0, 2, 5$ (blue, red, black respectively), and $T = 10$ K ($a = 0.0149$). The two curves are almost indistinguishable.

3.2.2 Static Slab and Sphere

Harrington (1973) and Neufeld (1990) derived an analytic expression for the spectrum $J(x, \tau_0)$ of radiation emerging from an optically thick ($\sqrt{\pi}\tau_0 \gtrsim 10^3/a$), uniform, static slab of neutral hydrogen, where line-centre photons are injected at the centre of the slab, atomic recoil is neglected and τ_0 is the centre-to-edge optical

depth at line-centre,

$$J(x, \tau_0) = \frac{\sqrt{6}}{24\sqrt{\pi}} \frac{x^2}{a\tau_0} \frac{1}{\cosh\left[\sqrt{\pi^3/54} \, |x^3|/a\tau_0\right]} \, , \qquad (3.23)$$

which is normalised to $(4\pi)^{-1}$. The comparison of our code with this analytic solution (for $T = 10$ K) is shown in the top panel of Figure 3.2. The agreement is very good, especially as τ_0 increases.

We can also compare the results of our code to the analogue of the above solution for a uniform, static sphere (DHS06, Equation (9)). As the bottom panel of Figure 3.2 shows ($T = 10$ K), the agreement is again very good.

It is worth pausing to gain an intuitive understanding of the features of Figure 3.2. The key to understanding this spectrum is the realisation that the photon executes a random walk in *both frequency and physical space*. When a photon is in the Doppler core, its mean free path is very short, meaning that there is very little spatial diffusion. Most scatterings will be with atoms with the same velocity along its direction of motion as the atom that emitted it. Occasionally, however, the photon will collide with a very fast moving atom from the tail of the Maxwell-Boltzmann distribution, with large velocities perpendicular to the photon's direction. When this photon is re-emitted, it will be far from line-centre — i.e. it will be in the wings of the distribution. The photon is now travelling through a slab that is comparatively optically thin. What happens next depends on the optical depth of the slab (τ_0).

In the case of moderate optical depth ($a\tau_0 \lesssim 10^3$), a single "catastrophic" scattering into the wings is enough to render the slab optically thin to the photon. A rough estimate of the frequency of the escaping photons (x_e) is given by,

$$\tau \approx \tau_0 e^{-x_e^2} \approx 1 \qquad \Rightarrow \qquad x_e \approx \pm\sqrt{\ln \tau_0}. \qquad (3.24)$$

This case is discussed in Osterbrock (1962). Adams (1972) introduced the term *single longest flight* to describe this scenario.

For extremely optically thick media ($a\tau_0 \gtrsim 10^3$), however, the optical depth in the damping wings is enough to prevent the photon from escaping from the medium in a single long flight. Instead, the photon will execute a random walk in physical space with a relatively long mean free path. Osterbrock (1962) showed that during this 'walk in the wings', there will also be a random walk in frequency
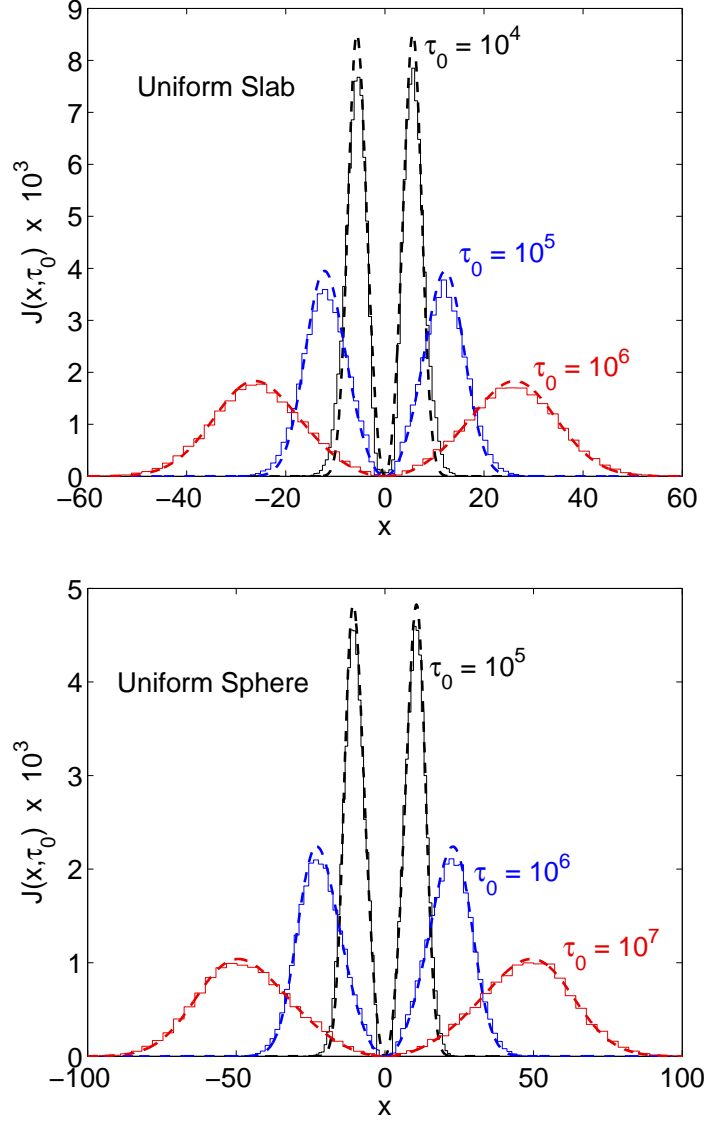
Figure 3.2: *Upper panel:* the emergent spectrum from an optically thick ($\sqrt{\pi}\tau_0 \gtrsim 10^3/a$), uniform, static slab of neutral hydrogen, where line-centre photons are injected at the centre of the slab. The solid histogram shows the results of our code. The dashed line shows the analytic solution of Harrington (1973) and Neufeld (1990). We set $T = 10$ K, and τ_0 is the centre-to-edge optical depth at line-centre, labelled for the different curves. The agreement is very good, especially as τ_0 increases. *Lower panel:* As before, but for a uniform sphere. The agreement is again very good.

space: the rms Doppler shift of each scatter is $x \sim 1$, with a mean shift per scatter of $1/|x|$, with a bias that tends to return the photon to line-centre. Thus, after a large number of scatterings, the photon will return to the Doppler core and once again experience very little spatial diffusion. The cycle of an initial scatter to the wings followed by the random walk back to the core (in frequency space) is termed an *excursion* (Adams 1972).

It is at this point that Adams (1972) points out a mistake in Osterbrock (1962), the resolution of which is quite illuminating. Osterbrock (1962) assumes that, in extremely optically thick media, the distance travelled in any particular excursion will be small compared to the size of the region. Thus, each excursion can be considered to be a single step in an ordinary random walk. However, Adams (1972) points out that we can test this assumption by asking which is more likely to happen first: the photon uses a large number of small excursions to random-walk out of the medium, or the photon uses one large excursion to escape? Adams (1972) showed that it is the second option — photons will escape the medium on their *single longest excursion*.

We can again give a rough estimate of the escape frequency of the photons. If a photon is scattered to frequency x in the wings, and each scattering sends the frequency on average $1/|x|$ back to the core, then each excursion will contain $\mathcal{N} \sim x^2$ scatterings. Between each scattering, the photon will travel a physical distance Δs defined by $\sigma_x n_{\mathrm{HI}} \Delta s \sim 1$. If this distance were travelled at line-centre, it would correspond to an optical depth of $\Delta \tau_0 = \sigma_0 n_{\mathrm{HI}} \Delta s = \sigma_0/\sigma_x$. Now, $\sigma_0/\sigma_x \approx 1/H(a,x) \sim x^2/a$, where we have (reasonably) assumed that we are in the damping wings. Thus, between each scattering, the photon will travel a line-centre optical depth of $\Delta \tau_0 \sim x^2/a$. Further, after $\mathcal{N}$ scatterings, the photon will have travelled an rms line-centre optical depth of $\tau_0^{\mathrm{rms}} \sim \sqrt{\mathcal{N}} \Delta \tau_0 = |x|^3/a$ (see, e.g. Rybicki & Lightman 1979, pg. 35).

Now, the photon will escape when, in the course of an excursion, it can diffuse a distance comparable with the size of the medium i.e. $\tau_0^{\mathrm{rms}} \sim \tau_0$. Putting the above equations together, we find that the critical escape frequency is $x_e \sim \pm(a\tau_0)^{1/3}$. This agrees very well with the analytic solution of Harrington (1973) and Neufeld (1990) for a static slab, which has its peak at $x_p = \pm 1.06(a\tau_0)^{1/3}$. The static sphere solution of Dijkstra et al. (2006a) has its peak at $x_p = \pm 0.92(a\tau_0)^{1/3}$. This means that if we modelled a DLA as a static sphere of HI at temperature T with
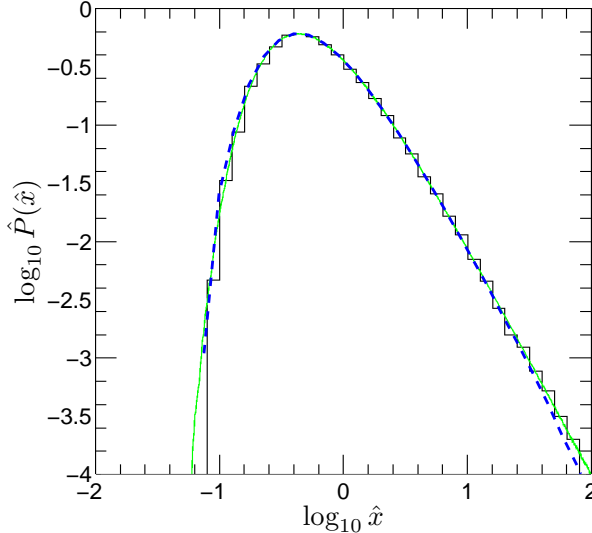
Figure 3.3: Lyα RT through uniform H I undergoing Hubble expansion with $\boldsymbol{v}_{\mathrm{b}} = H(z)\boldsymbol{r}$. The histogram is the result from the code of DHS06, the green solid curve is the solution of Loeb & Rybicki (1999), and the dashed blue curve is the result of our code. The agreement is again excellent.

maximum edge-to-edge column density N_{HI}, a Lyα photon emitted at the centre of the system will emerge with a characteristic frequency (expressed as a velocity) of:

$$v_p = 165.7 \text{ km s}^{-1} \left(\frac{T}{10^4 \text{ K}}\right)^{\frac{1}{6}} \left(\frac{N_{\mathrm{HI}}}{2 \times 10^{20} \text{ cm}^{-2}}\right)^{\frac{1}{3}}. \tag{3.25}$$

3.2.3 Hubble Flow

To test the code for a scenario with significant bulk motions of the gas, we compare with the modelling of Loeb & Rybicki (1999). Loeb & Rybicki (1999) investigated Lyα RT for a uniform H I distribution undergoing homogeneous expansion with $\boldsymbol{v}_{\mathrm{b}} = H(z)\boldsymbol{r}$, where $H(z)$ is the Hubble constant at redshift z. If a photon is blueward of line-centre (in the fluid frame), then the expansion of the Universe will eventually redshift the photon back into resonance. Only photons redward of line-centre can then propagate to infinity. The optical depth to infinity is

$$\tau_\infty(\bar{x}) = -\frac{n_{\mathrm{HI}} \, \sigma_0 \, a \, v_{\mathrm{th}}}{\sqrt{\pi} H(z)\bar{x}} \equiv \frac{x_*}{\bar{x}}, \tag{3.26}$$

where $\bar{x}$ is the frequency in the fluid frame. This defines a critical frequency x_*. Photons with $\bar{x} \ll x_*$ have redshifted enough to stream freely. We follow Loeb & Rybicki (1999) and use a new frequency variable $\hat{x} = \bar{x}/x_*$. We refer the reader to Appendix B2 of DHS06 for a careful discussion of the modifications necessary to permit a meaningful comparison between the two codes.

In Figure 3.3 we compare the results of our code with those of Loeb & Rybicki (1999) and DHS06. We set $z = 10$, $n_{\mathrm{HI}} = 2 \times 10^{-7}(1 + z)^3$ cm^{-3} and $T = 10$ K. Note that $\int \hat{P}(\hat{x}) \, \mathrm{d}\hat{x} = 1$. The agreement is again excellent.

3.2.4 NFW Haloes

DHS06 considered Lyα radiative transfer through a spherically symmetric halo with an NFW-like (Navarro et al. 1996) profile for the neutral hydrogen and a power-law bulk velocity profile. We will have much more to say about such models in Chapter 5. For the purposes of this chapter, we can test our implementation of the spherical shells as a method to deal with density gradients and velocity fields by comparing the results of our code with those of DHS06. The results are shown in Figure 3.4.

The top two panels show the "1c" model of DHS06, whose parameters can be found in Appendix A of that paper. The "c" stands for "central", such that all photons are created at the centre of the halo. Similarly, the bottom panels show the "2c" model. These models differ in their dependence of the bulk velocity on radius. In the top panels, the bulk inflow velocity increases toward the outer parts of the halo. The opposite is the case in the bottom panels. The left panels show the emergent spectra. The right panels show the surface brightness profile as a function of the impact parameter. The solid black curve is the result of DHS06, while the dashed red curve is the result of our code. The two lines are in excellent agreement.

3.3 Lyα Radiative Transfer in a 3D Grid

In Chapter 6, we will apply our radiative transfer code to a 3D distribution of neutral hydrogen, using a Cartesian grid. 3D Lyα radiative transfer has been studied by Cantalupo et al. (2005), Tasitsiomi (2006) and Laursen et al. (2009a),
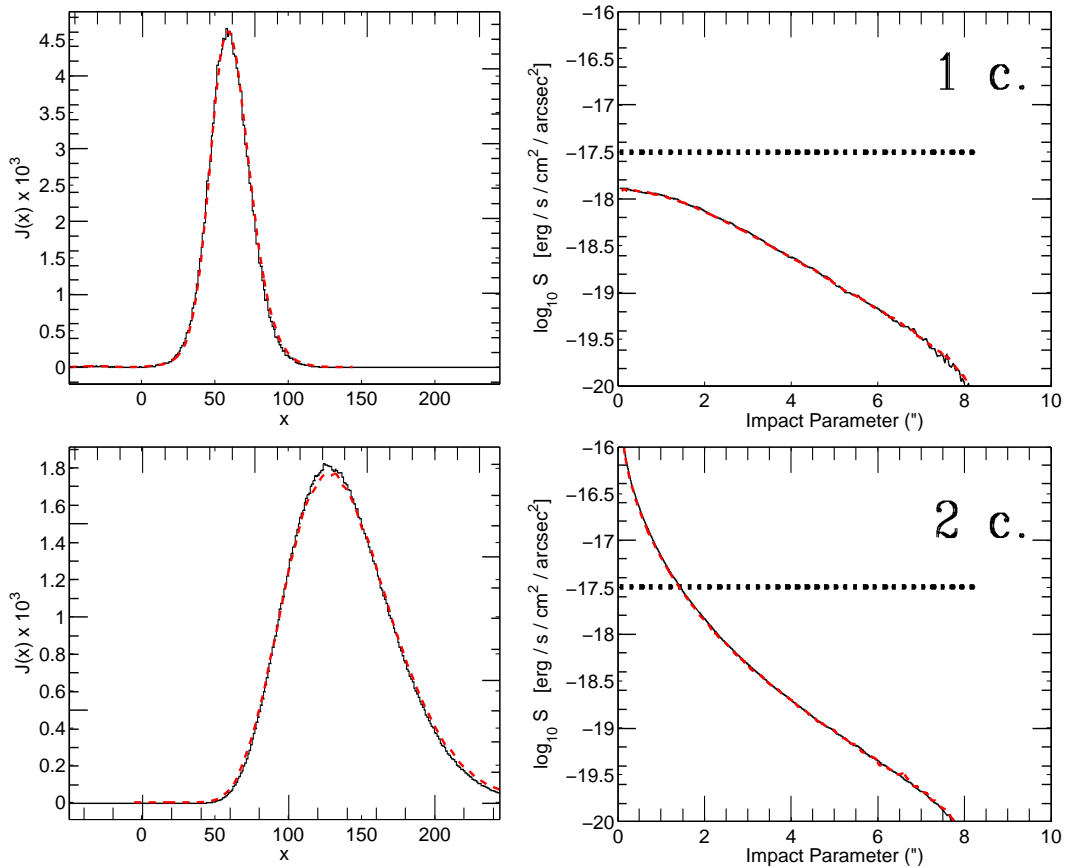
Figure 3.4: Lyα radiative transfer through an NFW-like halo, where the gas is infalling with a power-law bulk velocity profile. The parameters of these models can be found in Appendix A of DHS06. In the top two panels, the bulk velocity decreases toward the centre of the halo. The opposite is the case in the bottom two panels. The left panels show the emergent spectra. The right panels show the surface brightness profile as a function of the impact parameter. The solid black curve is the result of DHS06, while the dashed red curve is the result of our code. The two lines are in excellent agreement.

in the context of fluorescent emission from the IGM, bright Lyα emitters at $z \approx 8$ and young Lyman break galaxies, respectively. A number of changes to the code are required to trace a photon through a 3D density field sampled on a grid.

Firstly, as the temperature can change from cell to cell, we need to take into account the corresponding change in x, even when the frequency itself does not change. The choice of $x_{\rm crit}$ for the acceleration scheme also needs to be adapted to the conditions in the current cell. We use the prescription given in Laursen et al. (2009a), where $x_{\rm crit}$ depends on the value of $a\tau_0$ in the current cell.

The emergent spectrum will depend on the angle from which the system is viewed. Rather than waiting for enough photons to emerge in a given direction, we implement the "peeling-off" algorithm, first described in Yusef-Zadeh et al. (1984); see also the summary in Wood & Reynolds (1999). At each scattering, the probability of escape in the direction of the observer is calculated and a suitable weight added to the corresponding 2D pixel. We place observers at $\pm\infty$ on the x-, y- and z-axes, for a total of six viewpoints. The photons that eventually escape the system are used to calculate the angularly-averaged spectrum and surface brightness profile.

We inject photons at the centre of mass of the halo. The photons are created with line-centre frequency ($x_{\rm initial} = 0$) in the fluid frame of the gas.

We have run standard test problems to test our grid-based code. Figure 3.5 shows that code successfully reproduces the spectrum for a uniform sphere (Section 3.2.2). The NFW haloes of Section 3.2.4 are also reproduced very well.
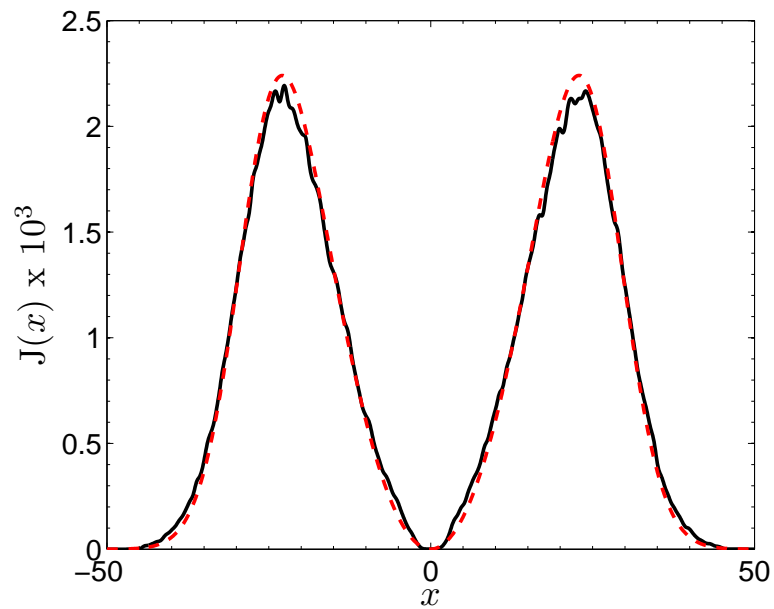
Figure 3.5: 3D grid-based Lyα RT through a static, uniform sphere with centre-to-edge optical depth $\tau_0 = 10^6$ and a temperature of $T = 10^4$ K. The solid line is the result of our code, while the dashed line is the analytical solution of DHS06. The agreement is very good.

Chapter 4

The Emission and Absorption Properties of DLAs

The contents of this chapter have been published as: Luke A. Barnes, Martin G. Haehnelt, 2009, "A Joint Model for the Emission and Absorption Properties of Damped Lyman Alpha Absorption Systems", *Monthly Notices of the Royal Astronomical Society*, 397, 511-519. It is reproduced here in full. As a result, Section 4.1 will overlap somewhat with the introduction to DLAs given in Chapter 2.

4.1   Introduction

Quasar absorption spectra provide excellent probes of the distribution of baryons in the high-redshift Universe. Damped Lyman Alpha systems (DLAs, historically defined as having a neutral hydrogen column density $N_{\text{HI}} > 2 \times 10^{20}\text{cm}^{-2}$) are particularly useful as they are likely to play an important role as a reservoir of gas for the formation of stars and galaxies at high redshift. They dominate the neutral

gas content of the Universe between $z \sim 0 - 5$, and at $z \sim 3.0 - 4.5$ their neutral gas content is comparable to visible stellar mass in present-day galaxies (Wolfe 1986, Storrie-Lombardi et al. 1996, Storrie-Lombardi & Wolfe 2000). DLAs thus form an important link between primordial plasma and the stellar structures that form from it.

In spite of observations of over 1000 DLAs, Wolfe et al. (2005) still conclude that the question "what is a damped Lyα system?" has not yet been answered conclusively. One of the reasons for this is that absorption spectra provide only indirect information in velocity space, and only probe the gas along one line-of-sight through the galaxy. The Lyα absorption feature itself provides no information about the velocity structure of the DLA, because of the large optical depth even in the damping wings. This has led observers to look at the absorption profiles of low-ionisation metals associated with DLAs. Low-ionisation species like SiII, CII and FeI are believed to be good tracers of the neutral gas in DLAs. Prochaska & Wolfe (1997) developed the velocity width distribution of these low-ion absorption profiles into an important diagnostic tool for DLAs. Their much lower absorption optical depth allows us to extract detailed kinematical information about the gas in DLAs. The absorption profiles are typically clumpy and asymmetric, with the strongest absorption feature often occurring at one edge of the profile. Velocity widths range from 30 km s^{-1} up to several hundred km s^{-1}. Note that there are few systems with narrow absorption profiles with velocity width < 30 km s^{-1}.

Kinematical models aiming to reproduce the velocity width data fall into two categories. Wolfe (1986) suggested a close connection between DLAs and disks of present-day spiral galaxies. Prochaska & Wolfe (1997) modelled DLAs as thick rotating disks with a rotation speed (~ 200 km s^{-1}) typical of present-day galaxies (see also Jedamzik & Prochaska (1998)). Haehnelt et al. (1998) challenged this interpretation and demonstrated that it is not unique. The merging of protogalactic clumps expected in Cold Dark Matter (CDM) models for structure formation can explain the shape of the profiles equally well. Galactic winds have also been suggested to play an important role (e.g. Fabian 1999). They further showed that for the same virial velocity, merging clumps produce significantly larger velocity width and argued that the latter interpretation is favoured by the observed velocity width distribution in the context of the CDM paradigm for structure formation (Haehnelt et al. 2000, Maller et al. 2001). Zwaan et al.

(2008) use 21cm emission to study the kinematics of the neutral hydrogen in the THINGS sample of nearby galaxies. They conclude that the velocity width of the neutral gas in present-day disk galaxies with $\log N_{\mathrm{HI}} > 20.3$ is much smaller than that observed in DLAs at $z \sim 3$.

The level of enrichment with metals provides another important clue as to the nature of DLAs — see Pettini (2004, 2006), Wolfe et al. (2005) for reviews. Metal absorption is observed in all DLAs, though as a population they are metal poor. DLAs are also relatively dust free (Ellison et al. 2001, Wild et al. 2006). Initially, the low metallicity was used to argue that DLA host galaxies are the chemically unevolved but otherwise very similar counter-parts of typical present-day spiral galaxies (Wolfe 1986). In the model of Haehnelt et al. (1998), DLAs instead preferentially probe the outer parts of much less massive galaxies, many of which end up as building blocks of typical present-day galaxies that form by hierarchical merging in CDM-like models for structure formation. Recently, Pontzen et al. (2008) demonstrated that such a model fits the observed metallicity of DLAs at $z \sim 3$ very well.

As already mentioned, absorption is measured along a single line of sight and thus is a one-dimensional probe of the properties of the DLA. To explore the spatial extent and structure of the DLA, we need to observe DLAs in emission. Attempts to do this have focussed on both line and continuum emission. Lyα emission holds great potential in this respect. Star formation, cooling radiation and fluorescent re-emission of the meta-galactic UV background are all expected to contribute at different levels. In addition, stellar continuum emission from the newly formed stars should also be bright enough to be detectable.

Many observers have attempted to find the galaxy counterparts of DLAs at high redshift in emission by searching adjacent to quasar sightlines with known absorption systems (Fynbo et al. 1999, Bunker et al. 1999, Kulkarni et al. 2000, 2001, Warren et al. 2001, Christensen et al. 2007). This is a difficult task, as the light of the extremely bright quasar must be accurately subtracted to study the light of the galaxy, which is very faint in comparison. Kulkarni et al. (2000) and others caution of the possibility that a given emission feature is a Point Source Function (PSF) artefact rather than a real source. Christensen et al. (2007) report that, for $z > 2$, six DLA galaxies have been confirmed through spectroscopic observation of Lyα emission, with other techniques producing a few additional

candidates. Christensen et al. added another six Lyα emission candidates to this group. A quantitative statistical interpretation of the many (largely unsuccessful) searches is difficult if not impossible, but the rather low success rate appears to be consistent with their interpretation as galaxies of rather low mass and star formation rate.

Rauch et al. (2008) reported the results of a long-slit search for low surface brightness Lyα emitters at redshift $z \sim 3$, which reached flux levels that are about a 10 times lower than previous Lyα surveys at this redshift. They found 27 faint line emitters, many of which are extended in wavelength and real space. They argue that the majority of the emitters are likely to be Lyα (rather than low-z interlopers). The angular size of the Lyα emission regions of the resolved sources is surprisingly large and corresponds to radii of 10-30 kpc. Wolfe & Chen (2006) searched for spatially extended low surface brightness continuum emission in the Hubble Ultra Deep Field and placed stringent upper limits on extended star formation in DLAs at $z \sim 3$. This result also argues against the possibility that we are seeing a distribution of several compact knots of stellar emission that are smeared out due to seeing effects. As discussed by Rauch et al. (2008) their observation can be reconciled with those of Wolfe & Chen (2006) if the emitters are powered by a central region of star formation and processed by radiative transfer through surrounding neutral hydrogen. This would, however, require scattering of Lyα photons to large radii. The Lyα radiative transfer simulations of Dijkstra et al. (2006a), for more massive haloes in a different context, suggest that this is – at least in principle – possible. Detailed radiative transfer modelling will be required to see whether this is indeed a realistic proposition for the observed sample of faint Lyα emitters. Rauch et al. (2008) note that the incidence rate inferred from the space density and the size distribution of the emitters is similar to that of DLAs, and suggest that they are the host population of DLAs and high column density Lyman Limit Systems (LLS). If the emitters are indeed the host galaxies of DLAs, then the observations of Rauch et al. (2008) give us the size distribution and space density of DLA host galaxies at $z \sim 3$.

Models predicting the velocity width and size distribution of DLAs have been constructed based on the observed luminosity function of galaxies (Fynbo et al. 1999, 2008) and on the Press-Schechter formalism (Press & Schechter 1974) in conjunction with numerical simulations (Gardner et al. 1997a,b, Haehnelt et al.

1998, 2000, Gardner et al. 2001, Nagamine et al. 2004, 2007). More recently, numerical simulations have attempted to model the entire DLA population self-consistently (Razoumov et al. 2006, 2008, Pontzen et al. 2008). Note that these models, like all models that reproduce the observed dN/dz of DLAs with host galaxies that have space densities similar to observed galaxies, require that the HI distribution responsible for Lyα absorption extends well beyond the stellar distribution of the host galaxies.

In this chapter, we revisit models for the absorption properties of DLAs in the light of the size distribution data of Rauch et al. (2008), improved data on the velocity width distribution from metal absorption lines (which has presented a challenge to purely numerical simulations — see Razoumov et al. (2008)) and numerical simulations with increased resolution, box size and sophistication incorporating the additional physics of radiative transfer, gas chemistry and star formation.

Throughout this chapter we use cosmological parameters of the 5 year WMAP data (Hinshaw et al. 2009): $(h, \Omega_M, \Omega_b, \Omega_\Lambda, \sigma_8, n) = (0.701, 0.279, 0.046, 0.721, 0.817, 0.96)$.

4.2 A Joint Model for the Kinematical Properties of DLAs and the Cumulative Size Distribution of the Faint Lyα Emitters

4.2.1 The Haehnelt et al. Model

Rauch et al. (2008) argued that their population of faint Lyα emitters is the same as or has at least a large overlap with that of DLA/LLs host galaxies. They further pointed out that the space density and sizes should agree well with those predicted by the DLA model of Haehnelt et al. (1998), which models DLAs in the context of CDM models of structure formation.

We here revisit and update this model to investigate whether it can explain the properties of DLAs and the new population of faint emitters, assuming that these are the same objects. We start with summarizing the salient properties of the model. As discussed in the introduction, *ab initio* numerical simulation of the gas at the centre of galaxies, where complex non-linear gas physics including star

formation and the associated feedback are important, is still very challenging. The Haehnelt et al. model therefore takes a hybrid approach, using a combination of Press-Schechter formalism and results from numerical simulations to model the kinematic properties of DLAs (see Johansson & Efstathiou (2006) for a semi-analytical model of DLAs that explicitly models feedback).

The model uses the space density of DM haloes as a proxy for the space density of DLA host galaxies. With the refinement to the Press-Schechter formalism introduced by Sheth & Tormen (2002), the number of dark matter haloes per unit comoving volume at redshift z with mass (baryonic + CDM) in the interval $(M, M + \mathrm{d}M)$ can be estimated as,

$$n_M(M, z) \, \mathrm{d}M = A \left(1 + \frac{1}{\nu'^{2q}} \right) \sqrt{\frac{2}{\pi}} \frac{\rho_0}{M} \frac{\mathrm{d}\nu'}{\mathrm{d}M} \exp \left(-\frac{\nu'^2}{2} \right) \, \mathrm{d}M, \qquad (4.1)$$

where σ_M is the rms fluctuation amplitude of the cosmic density field in spheres containing mass M, ρ_0 is the present cosmic matter (baryonic + CDM) density, $\nu' = \sqrt{a}\nu$, $\nu = \delta_c/[D(z)\sigma_M]$. $D(z)$ is the growth factor at redshift z (Carroll et al. 1992), $\delta_c = 1.686$, $a = 0.707$, $A \approx 0.322$ and $q = 0.3$. We have used the fitting formula in Eisenstein & Hu (1999) to calculate the matter power spectrum.

We will be interested in the kinematic properties of DLAs, for which the virial velocity is a more convenient quantity to characterize the DM halo than the mass. The two are related as follows (e.g. Maller & Bullock 2004),

$$v_c = 106 \text{ km s}^{-1} \left(\frac{\Delta_v}{174} \right)^{\frac{1}{6}} \left(\frac{\Omega_M h^2}{0.137} \right)^{\frac{1}{6}} \left(\frac{1+z}{4} \right)^{\frac{1}{2}} \left(\frac{M}{10^{11} M_\odot} \right)^{\frac{1}{3}}, \qquad (4.2)$$

where Δ_v is the overdensity of the halo (see Bryan & Norman 1998).

We use a simple power-law relation between the virial velocity of the DM halo and the DLA cross-section,

$$\sigma(v_c) = \pi r_0^2 \left(\frac{v_c}{200 \text{ km s}^{-1}} \right)^{\beta}, \qquad (4.3)$$

where β and r_0 are parameters. The value of β has been the source of some controversy, due to numerical simulations still finding it challenging to reliably model the spatial distribution of the gas in the high-density region probed by DLAs and LLs. Gardner et al. (1997a) originally favoured a value of $\beta = 2.94$ (at $z = 3$, for a ΛCDM cosmology), but their later work revised this to $\beta = 1.569$.

Prochaska & Wolfe (2001) pointed out that this low value of β is incompatible with the observed DLA velocity widths. Haehnelt et al. (2000) found that the observed velocity width distribution of metal-lines is reproduced well with a value of $\beta \sim 2.5$, which we also use here.

Haehnelt et al. further found that they needed to introduce a lower cut-off in virial velocity in order to fit the velocity width distribution of low-ionisation absorption systems. Otherwise, their model predicted too many very narrow metal absorption systems, which are not observed. They therefore assumed that DM haloes with virial velocities smaller than a minimum velocity v_{min} do not host DLAs.

Here we will slightly relax this assumption and model the suppression of the cross-section of DLAs in haloes with small circular velocities as a gentler exponential decline,

$$\sigma(v_{\text{c}}) = \pi r_0^2 \left(\frac{v_{\text{c}}}{200 \text{ km s}^{-1}} \right)^{\beta} \exp\left(- \left(\frac{v_{\text{c},0}}{v_{\text{c}}} \right)^{\alpha} \right). \qquad (4.4)$$

We consider a range of values for the parameters $v_{\text{c},0}$ and α. Note that a sharp cut-off corresponds to $\alpha = \infty$.

It remains to choose the parameter r_0. We will follow Haehnelt et al. (2000) by fixing r_0 so that the overall rate of incidence of absorbers per unit redshift $\text{d}\mathcal{N}/\text{d}z$ agrees with the observational value,

$$\frac{\text{d}\mathcal{N}}{\text{d}z} = \frac{\text{d}l_p}{\text{d}z} \, (1+z)^3 \int_0^{\infty} \sigma(M,z) \, n_M(M,z) \ \text{d}M. \qquad (4.5)$$

We take the value of $\text{d}\mathcal{N}/\text{d}z = 0.24$ at $z = 3$, which is consistent with $\text{d}\mathcal{N}/\text{d}X = 0.067$ (Prochaska et al. 2005, Péroux et al. 2005). The ratio of proper distance interval to redshift interval is given by,

$$\frac{\text{d}l_p}{\text{d}z} = \frac{c}{H(z)(1+z)} \ , \qquad (4.6)$$

and the so-called absorption distance, X, is defined by,

$$\text{d}X \equiv \frac{H_0}{H(z)}(1+z)^2 \ \text{d}z \ . \qquad (4.7)$$

The resulting values of r_0 are given in the caption of Figure 4.1.

Further, it is useful to define the line density distribution (N), such that the number of intersections ($\mathrm{d}^2\mathcal{N}$) of a random line of sight with systems that have mass in the interval $(M, M + \mathrm{d}M)$, located in the redshift interval $(z, z + \mathrm{d}z)$ is,

$$\mathrm{d}^2\mathcal{N} \equiv N(M, z)\ \mathrm{d}M\ \mathrm{d}z \tag{4.8}$$

$$= (1 + z)^3\ n_M(M, z)\ \sigma(M, z)\ \frac{\mathrm{d}l_p}{\mathrm{d}z}\ \mathrm{d}M\ \mathrm{d}z. \tag{4.9}$$

4.2.2 The Velocity Width Distribution of Low-Ionisation Absorption

To calculate the velocity width distribution, Haehnelt et al. used a conditional probability distribution: $p(v_\mathrm{w}|v_\mathrm{c})\ \mathrm{d}v_\mathrm{w}$ is the probability that a DLA in a halo with circular velocity v_c has a velocity width in the interval $(v_\mathrm{w}, v_\mathrm{w} + \mathrm{d}v_\mathrm{w})$. On the basis of their numerical simulations, they assumed it to be a function of the ratio $v_\mathrm{w}/v_\mathrm{c}$. The number of systems along a random line of sight in the interval $(X, X + \mathrm{d}X)$ with velocity width greater than v_w is given by,

$$l(> v_\mathrm{w}, X) = \int_{v_\mathrm{w}}^{\infty} \left[\int_0^{\infty} p(v_\mathrm{w}|v_\mathrm{c}(M)) \frac{\mathrm{d}^2\mathcal{N}}{\mathrm{d}X\ \mathrm{d}M} \mathrm{d}M \right] \mathrm{d}v_\mathrm{w}. \tag{4.10}$$

We will use here the conditional probability distribution as given in Haehnelt et al. (2000, Figure 1). The distribution peaks at $v_\mathrm{w}/v_\mathrm{c} \approx 0.6$, dropping to zero below $v_\mathrm{w}/v_\mathrm{c} \approx 0.1$ and above $v_\mathrm{w}/v_\mathrm{c} \approx 2$. The numerical simulations on which the distribution is based did not contain star formation feedback. Simulations have become more sophisticated since then. We have therefore compared the $p(v_\mathrm{w}|v_\mathrm{c})$ distribution used here with that from the simulations of Pontzen et al. (2008, and private communication), which incorporate the effects of star formation and supernovae on the kinematics and spatial distribution of the gas in a simple manner. The differences in $p(v_\mathrm{w}|v_\mathrm{c})$ are small. Unless there is a fortuitous cancellation of different effects, this suggests that star formation in the simulations has a small effect on $p(v_\mathrm{w}|v_\mathrm{c})$. This is somewhat surprising, given the significant differences in resolution, cosmological volume, and additional physics, albeit reassuring for our modelling. Note, however, that the simulations still fail to produce realistic galactic winds, probably due to the rather simplistic fashion in which stellar feedback is incorporated. The much larger differences in $l(> v_\mathrm{w}, X)$ between our

model and the numerical simulations must therefore be mainly due to the different respective dependence of the DLA cross-section on the virial velocity of the host halo.

Figure 4.1 compares the predicted velocity width distribution with the observational data of Wolfe et al. (2005). The data of Prochaska & Wolfe (1997) are also shown in the bottom panels and is reasonably well fit with $v_{c,0} = 50$ km s^{-1}. This is very similar to what was found by Haehnelt et al. (2000). The new compilation of velocity width data by Wolfe et al. (2005) extends to significantly larger velocities and appears to require a somewhat larger value of $v_{c,0} = 70$ km s^{-1}. The apparent lack of neutral gas in small dark matter haloes can be plausibly attributed to the feedback effects of star formation and/or photoheating due to the meta-galactic UV background and perhaps even AGN. In most numerical simulations and models of galaxy formation, the feedback mainly affects haloes with somewhat smaller virial velocities than this. Therefore, either haloes with small virial velocities have larger velocity widths than we have assumed here (i.e. $p(v_{\mathrm{w}}|v_{\mathrm{c}})$ is different), or else feedback in haloes with virial velocities of $v_{c,0} = 50$ km s^{-1} is more efficient than generally assumed. Note also that many of these simulations overproduce the number of observed galaxies at the faint end of the luminosity function. The cumulative velocity width distribution is not very sensitive to the shape of the cut-off for $\alpha \geq 2$.

The high velocity tail of the velocity distribution as compiled by Wolfe et al. (2005) has proven difficult to reproduce with numerical simulations, which attempt to model the spatial distribution of the neutral gas in DLAs self-consistently rather than assume a scaling of the absorption cross-section with the virial velocity of DM haloes. Generally, the simulations fail to produce a sufficient number of absorption systems with velocity widths as wide as observed. This is normally attributed by the authors of these studies to the fact that momentum and energy input into the gas due to star formation may not have been modelled with sufficient sophistication (Nagamine et al. 2004, Razoumov et al. 2006, Nagamine et al. 2007, Razoumov et al. 2008, Pontzen et al. 2008).
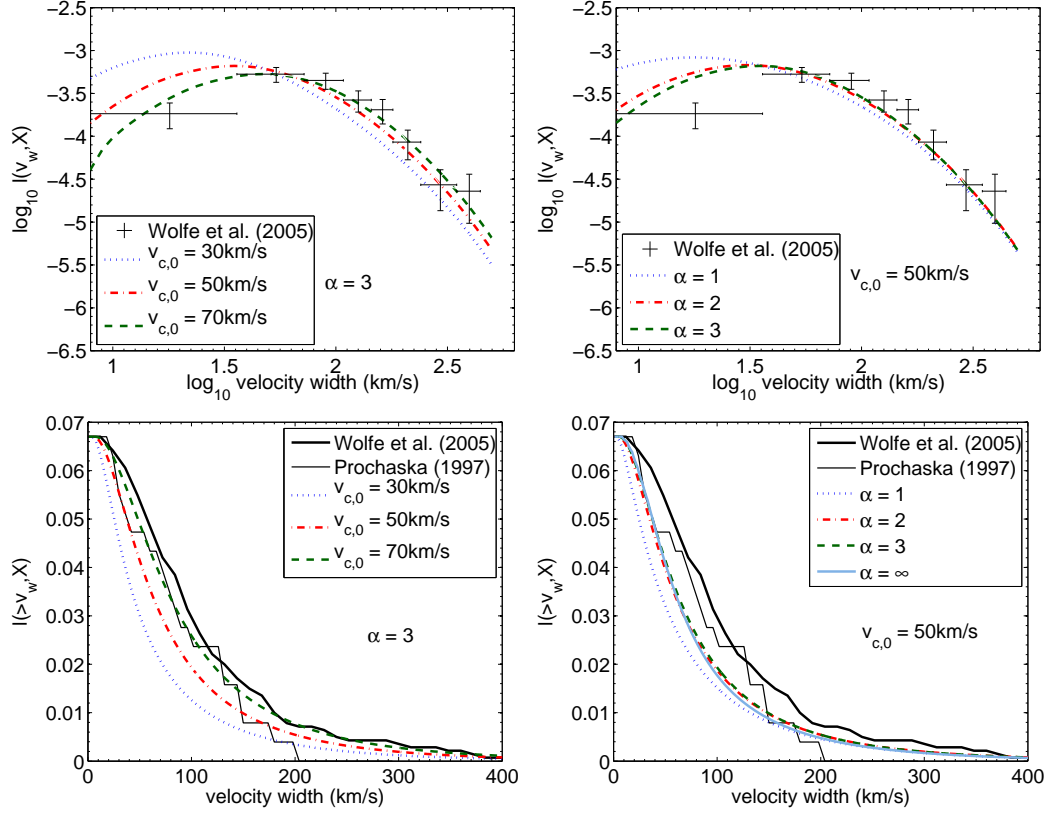
Figure 4.1: *Top Panels:* The velocity width distribution $l(v_{\mathrm{w}}, X)$ of the low-ionisation metal absorbers associated with DLAs. The black crosses show the observational data compiled in Figure 10 of Wolfe et al. (2005). *Bottom Panels:* The cumulative velocity width distribution $l(> v_{\mathrm{w}}, X)$ of the low-ionisation metal absorbers associated with DLAs. The thick solid black curve shows the observational data compiled in Figure 10 of Wolfe et al. (2005). The thin, solid black curve shows the older observational data of Prochaska & Wolfe (1997). *Left Panels:* The velocity width distribution of our model for an exponential suppression at small virial velocities of the cross-section for damped Lyα absorption as given by Equation (4.4) with $\alpha = 3$ and $v_{\mathrm{c},0} = 30, 50, 70$ km s^{-1}, respectively. The cross-section normalization for these models as given by Equation (4.5) is characterised by $r_0 = 18.5, 23.5, 28.4$ kpc. *Right Panels:* The velocity width distribution for $v_{\mathrm{c},0} = 50$ km s^{-1} and a range of values of $\alpha = 1, 2, 3, \infty$. For these models, $r_0 = 21.9, 23.6, 23.9, 23.5$ kpc.
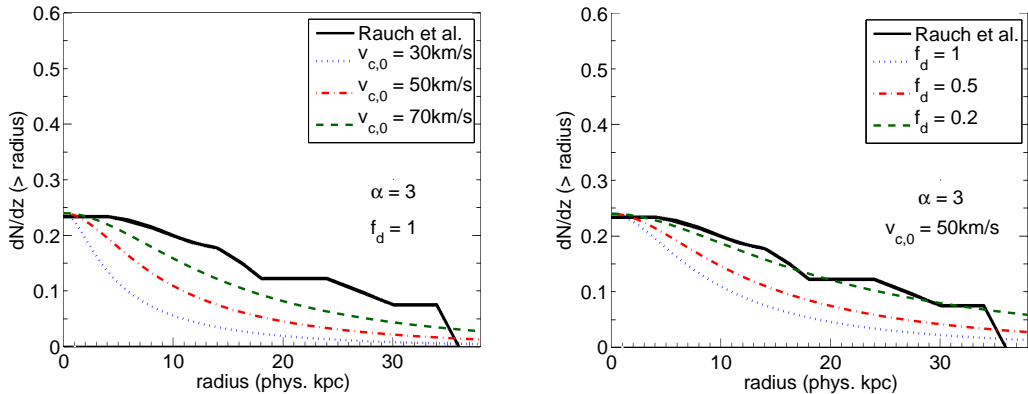
Figure 4.2: The cumulative incidence rate inferred from the size distribution of the population of faint Lyα emitters. The solid black curves are the observational data of Rauch et al. (2008). *Left:* Cumulative incidence rate in our model for $\alpha = 3$ and a range of values of $v_{c,0} = 30, 50, 70$ km s^{-1}. *Right:* The cumulative incidence rate in our model for $v_{c,0} = 50$ km s^{-1} and a range of values of the duty cycle $f_d = 1, \ 0.5, \ 0.2$.

4.2.3 The Cumulative Size Distribution

We now ask whether our model, which successfully fits the velocity width distribution of low-ions associated with DLAs, can also reproduce the cumulative size distribution of the emission regions of the new population of faint Lyα emitters, as shown by the black solid curve in Figure 4.2 (Rauch et al. 2008, figure 19, HI corrected). It asymptotes to $d\mathcal{N}/dz = 0.23$, which is very similar to the observed incidence rate of DLAs at the same redshift. To calculate the cumulative incidence rate for the DLA host galaxies in our model, we must relate the size of the emission region to the mass of the corresponding DM halo. The Lyα radiative transfer calculations of Dijkstra et al. (2006a) show that Lyα photons can be scattered to radii comparable to the virial radius. However, in the absence of simulations directly aimed at the scenario we are considering, we have chosen a different approach.

We calculate the radius of the emission from the absorption cross-section, assuming that the absorber is a sphere. The dependence of the cross-section on v_c then gives the radius as a function of mass. The cumulative incidence rate is

given by,

$$\frac{\mathrm{d}\mathcal{N}}{\mathrm{d}z}(> r, z) = \int_{M(r)}^{\infty} N(M', z) \, \mathrm{d}M'. \qquad (4.11)$$

The result is shown[1] in the left panel of Figure 4.2. The predicted sizes are consistently smaller than the observed sizes by a factor of 1.5 to 3, suggesting that the emission regions of the Lyα emitters are larger than the cross-section for damped absorption. Even though the integrated inferred incidence rate is similar to that of DLAs, in our model the emission regions of the Lyα emitters can thus not be identical to the regions responsible for damped Lyα absorption. Nevertheless, the two can be closely related.

To demonstrate this, we now explore a simple model where only a fraction f_d of the haloes is emitting Lyα radiation above the detection threshold at any one time. To keep the total inferred incidence rate fixed, we allow the cross-section of the individual Lyα emission regions to be larger than those for damped Lyα absorption by a corresponding factor f_d^{-1}. The Lyα emitters show typical signs of radiative transfer effects, like large velocity widths and asymmetric line profiles (Rauch et al. 2008, Section 6.3), and should thus be optically thick to Lyα radiation. However, we have no good handle here on the actual column density required to scatter emitted Lyα at large radii effectively. It may well be lower than that required for damped absorption, in which case it is certainly plausible that the region for Lyα emission extends beyond that for damped Lyα absorption. In the right panel of Figure 4.2, the cumulative incidence rate is shown for three values of the duty cycle $f_\mathrm{d} = (1, \ 0.5, \ 0.2)$ with $v_{\mathrm{c},0} = 50$ km s^{-1} and $\alpha = 3$. Our simple assumption of a duty cycle for the Lyα emission reconciles the cumulative incidence rate predicted by our model with the observed distribution for sizes below 35 kpc for $f_\mathrm{d} = 0.2$ ($f_\mathrm{d} = 0.4$ for $v_{\mathrm{c},0} = 70$ km s^{-1}). Our DLA host galaxies have large extended Lyα haloes and shine with a high duty cycle ($f_\mathrm{d} \geq 0.2$). The sudden drop in the observed distribution at $r \sim 35$ kpc is likely attributable to the following two effects. The first is the surface brightness limit of the instrument. Light from sources with large radii may be too diffuse to be detected. The second is the effect of searching a small survey volume. Large systems are more rare, so there is a limit to the size of sources that can be expected to be found within the

---

[1]We do not show the impact of altering α here. The effect is small, especially beyond a radius of 10 kpc.

rather small survey volume. Note that the size of the Lyα emitting region in our model is comparable to the virial radius of the corresponding DM halo hosting it.

4.3 Modelling the Luminosity Function of the Lyα Emitters

4.3.1 The Contribution of Lyα Cooling Radiation

Rauch et al. (2008) considered a number of astrophysical origins for the Lyα emission that they observe. They conclude that the most likely mechanism for producing Lyα photons is star formation. We here consider in more detail the argument that cooling radiation is unlikely to be the dominant source of Lyα for the observed emitters.

Dijkstra et al. (2006a) derive the following formula for the Lyα luminosity ($L_{\mathrm{Ly}\alpha}^{\mathrm{c}}$) of a collapsing protogalaxy due to cooling radiation, assuming that the gravitational binding energy is radiated as Lyα on a dynamical time scale,

$$L_{\mathrm{Ly}\alpha}^{\mathrm{c}} = 5.8 \times 10^{41} \left(\frac{M_{\mathrm{tot}}}{10^{11}}\right)^{5/3} \left(\frac{v_{\mathrm{amp}}}{v_{\mathrm{c}}}\right) \left(\frac{1+z_{\mathrm{vir}}}{4}\right)^{5/2} \left(\frac{2-\alpha_{\mathrm{d}}}{2.5}\right)^{1.2} \mathrm{erg\ s^{-1}} \quad (4.12)$$

where M_{tot} is the total (dark matter + baryons) mass of the halo, z_{vir} is the redshift at which the system virialises, and the bulk velocity of the infalling material, $v_{\mathrm{bulk}}(r)$, is parameterised by v_{amp} and α_{d} as a power law, $v_{\mathrm{bulk}}(r) = v_{\mathrm{amp}}(r/r_{\mathrm{vir}})^{\alpha_{\mathrm{d}}}$, where r_{vir} is the virial radius.[1] We will set $z_{\mathrm{vir}} = 3$, $v_{\mathrm{amp}} = v_{\mathrm{c}}$ and consider the lower limit of the range of α_{d} discussed in Dijkstra et al. (2006a), namely $\alpha_{\mathrm{d}} = -0.5$, so that we have an upper limit on $L_{\mathrm{Ly}\alpha}^{\mathrm{c}}$.

Equation (4.12) gives a relation between the mass of a halo and the luminosity due to Lyα cooling, which we can combine with the Press-Schechter formalism of Section 4.2 to predict the number of DLAs per unit comoving volume with Lyα luminosity greater than some $L_{\mathrm{Ly}\alpha}^{\mathrm{c}}$,

$$n(> L_{\mathrm{Ly}\alpha}^{\mathrm{c}}, z) = \int_{M(L_{\mathrm{Ly}\alpha}^{\mathrm{c}})}^{\infty} n_M(M', z)\ \mathrm{d}M' \quad (4.13)$$

---

[1]See Equation (10) of Dijkstra et al. (2006a) for a correction to this formula when $\alpha_{\mathrm{d}} < 0$ and r is small.
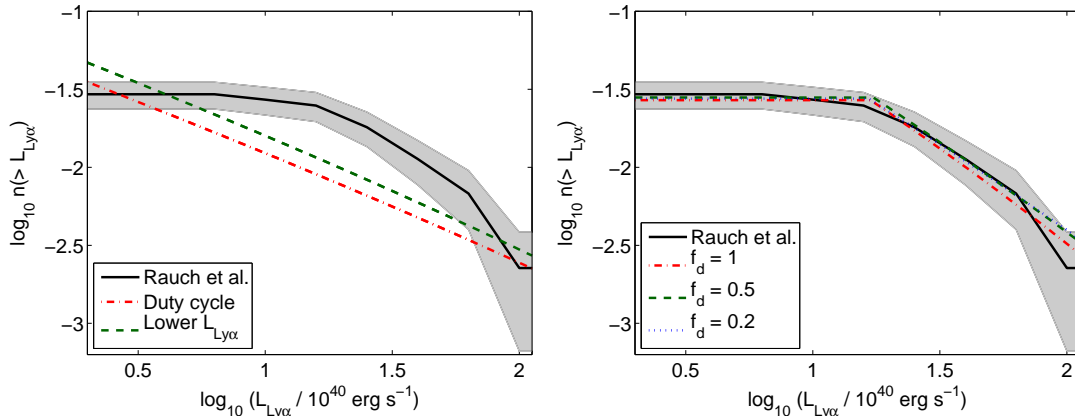
Figure 4.3: The cumulative luminosity function of the Lyα emitters. The black solid curve in both panels is the data taken from Fig. 9 of Rauch et al. (2008). The grey, shaded region is an estimate of the 1-σ confidence interval. *Left:* The green dashed curve and the dot-dashed red curve are for optimistic models for the Lyα emission due to Lyα cooling radiation as described in the text. *Right:* A simple model for the Lyα emission due to star formation as described in the text. The relevant parameters for $f_\mathrm{d} = (1,\ 0.5,\ 0.2)$ are $(L_0^\mathrm{s}, v_\mathrm{min}[\mathrm{km\ s}^{-1}]) = (4 \times 10^{41}, 75), (8 \times 10^{41}, 60), (1.8 \times 10^{42}, 45)$ respectively.

There is, however, an inconsistency here. As already mentioned, Equation (4.12) assumes that the cooling radiation will be emitted over the dynamical time t_dyn of the halo,

$$t_\mathrm{dyn} \approx \frac{r_v}{v_\mathrm{c}} = \left(\frac{1}{\frac{4}{3}\pi G \Delta_\mathrm{v} \bar{\rho}_m(z)} \right)^{1/2} \approx 353 \text{ Myrs.} \tag{4.14}$$

The proper time corresponding to the redshift interval [3.75, 2.67] of the Lyα survey is $t_z = 789$ Myrs. Thus, all the haloes cannot radiate at the luminosity $L_\mathrm{Ly\alpha}^\mathrm{c}$ given by Equation (4.12) for the entire redshift interval over which observations were taken. There are two ways to make the model consistent. The first is to impose a duty cycle, so that at any one time, only a fraction $f_\mathrm{d} = t_\mathrm{dyn}/t_z \approx 0.45$ of the haloes will be radiating. The second is to reduce the luminosity of each emitter, so that the gravitational energy of the halo is radiated over 789 Myrs.

The left panel of Figure 4.3 compares our prediction of $n(> L_\mathrm{Ly\alpha}^\mathrm{c}, z)$ with the observed luminosity function as given in Figure 9 of Rauch et al. (2008), shown in black. The red dot-dashed curve shows the model assuming a duty cycle. The

green dashed curve is for the reduced luminosity. Both curves are significantly below the data.

So far we have assumed (following Dijkstra et al. 2006a) that all gravitational binding energy is converted into Lyα radiation. In reality, hot accretion flows could result in substantial amounts of bremsstrahlung and He$^+$ line emission (Kereš et al. 2005), at the expense of $L_{\mathrm{Ly}\alpha}^{\mathrm{c}}$. Furthermore, the observed luminosities have not been corrected for slit losses, which can be as large as a factor of a few. The models shown in the left panel of Figure 4.3 are thus optimistic upper limits. We conclude that cooling radiation is indeed unlikely to contribute significantly to the majority of the faint Lyα emitters. We therefore agree with the suggestion of Rauch et al. (2008) that the most plausible remaining alternative is that the emitters are predominantly powered by centrally concentrated star formation surrounded by extended Lyα haloes. As already briefly mentioned in the introduction, detailed radiative transfer simulation will be required to decide if this is indeed a viable explanation. Note that by stacking the spectra of a subset of the emitters, Rauch et al. (2008) showed that the emission from these haloes appears to extend to radii even larger than those for the individually detected emission plotted in Figure 4.2 by a factor of at least two.

4.3.2 A Simple Model for the Lyα Luminosity Function

We will demonstrate now that a simple model where the Lyα luminosity due to stars $L_{\mathrm{Ly}\alpha}^{\mathrm{s}}$ is proportional to the total mass ($M \propto v_{\mathrm{c}}^3$) of the haloes with virial velocity above a threshold v_{min},

$$L_{\mathrm{Ly}\alpha}^{\mathrm{s}} = \begin{cases} L_0^{\mathrm{s}} \left(\frac{v_{\mathrm{c}}}{100 \text{ km s}^{-1}} \right)^3 \text{ erg s}^{-1} & \text{if } v_{\mathrm{c}} > v_{\mathrm{min}} \\ 0 & \text{otherwise,} \end{cases} \tag{4.15}$$

fits the observed luminosity function remarkably well. Note that detailed numerical simulations of much brighter Lyman-break galaxies and Lyα emitters appear to be consistent with this simple scaling of the Lyα emission with the properties of the DM host halo (Nagamine et al. 2008). In the right panel of Figure 4.3, we compare the observed luminosity function of the faint Lyα emitters with a luminosity function modelled in this way for a range of values of f_{d}. The observed luminosity function is fit well for the following parameter combinations

$(f_{\rm d}, L_0^{\rm s}, v_{\rm min}[{\rm km\ s}^{-1}]) = (1, 4 \times 10^{41}, 75), (0.5, 8 \times 10^{41}, 60), (0.2, 1.8 \times 10^{42}, 45).$
The upper and lower boundary of the grey shaded region can be fit with values of $L_0^{\rm s}$ and $v_{\rm min}$ that differ from the quoted values by $\sim 25\%$ and $\sim 5\%$ respectively.

Our assumed scaling $L_{\rm Ly\alpha}^{\rm s} \propto M$ is shallower than would be inferred from the star formation in most models of galaxy formation. The simulations of Pontzen et al. (2008), for example, predict $L_{\rm Ly\alpha}^{\rm s} \propto M^{1.6}$. These models, however, are generally tuned to produce a rather shallow faint end of the luminosity function. As discussed by Rauch et al. (2008), their observations imply that the luminosity function of Lyα emitters steepens considerably at very faint luminosities (cf. Le Delliou et al. 2006). Note that the faint end of the UV continuum luminosity function is also rather steep (Reddy & Steidel 2009).

Intriguingly, the values for the velocity cut-off and duty cycle in our model are very similar to those required to fit the velocity width distribution of low-ion absorbers associated with DLAs and the size distribution inferred from the Lyα emitters. We caution, however, that the significance of the apparent turnover at $\sim 1.25 \times 10^{40}$ erg s^{-1} at the faint end of the observed luminosity function is uncertain. At faint flux levels, the luminosity function will be affected strongly by the sensitivity limit of the observations.

4.4 The Masses and Virial Velocities of DLA/LL Host Galaxies

If the population of faint Lyα emitters detected by Rauch et al. (2008) can be identified with DLA/LL host galaxies, then this constitutes the first measurement of the space density and average size of DLA/LL host galaxies. The last section supported the suggestion by Rauch et al. that the Lyα emission is powered by star formation. In this case, with standard assumptions for the conversion of Lyα emission to star formation rate as used in Rauch et al. (2008) (based on Kennicutt (1998) and Case B assumptions for the conversion between Hα and Lyα from Brocklehurst (1971)), the Lyα luminosities correspond to star formation rates of 0.07 - 1.5 $M_\odot$ yr^{-1}, similar to that inferred by Wolfe et al. (2003) from the CII* λ1335.7 absorption in DLAs. No continuum is detected, so there is no information about stellar or total masses of the objects. Our modelling is thus
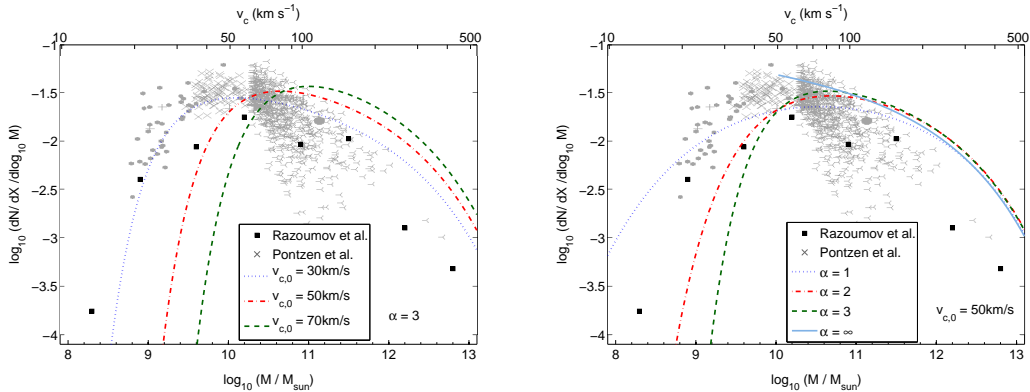
Figure 4.4: The contribution of different mass and virial velocity ranges to the incidence rate of DLAs ($\mathrm{d}^2\mathcal{N}/\mathrm{d}X/\mathrm{d}\log_{10} M$). The black squares in both panels show the results from the numerical model of Razoumov et al. (2008) for DLAs found within DM haloes, excluding intergalactic DLAs. The grey symbols in both panels show the results of the simulations of Pontzen et al. (2008). *Left:* The curves are for our model with $\alpha = 3$ and a range of values of $v_{c,0} = 30, 50, 70$ km s^{-1}. *Right:* The curves are for our model with $v_{c,0} = 50$ km s^{-1} and a range of values of $\alpha = 1, 2, 3, \infty$.

currently the only handle we have on the masses (and virial velocities) of what should be a statistically representative sample of DLA host galaxies.

In Figure 4.4, we show the contribution of DM haloes of different masses and virial velocities to the incidence rate of DLAs in our model, for the range of parameters used to model the suppression of the cross-section for damped Lyα absorption in low-mass DM haloes. We also show the results from two recently published numerical simulations of DLAs (Razoumov et al. 2008, Pontzen et al. 2008). Note that our model and the numerical simulations have similar DM halo mass functions, so that Figure 4.4 therefore allows a comparison of the respective DLA cross-sections as a function of halo mass. The differential line density for DLAs is calculated similarly to N, except that we consider intervals of $\mathrm{d}X$ and $\mathrm{d}\log_{10} M$,

$$\frac{\mathrm{d}^2\mathcal{N}}{\mathrm{d}X \; \mathrm{d}\log_{10} M} = \frac{c}{H_0} \ln 10 \; M \; n_M(M, X) \; \sigma(M, X). \tag{4.16}$$

Larger values of α result in a sharper turnover at low masses, at the expense of increasing the abundance of DLAs with high masses (the area under the plot is

normalised).

The majority of the DLAs in our model have virial velocities in the range 50 to 200 km s^{-1}, corresponding to total masses of 10^{10} to $10^{12} M_\odot$. Note that this range of virial velocities and masses is similar to that found by Nagamine et al. (2007) in their simulations. Bouché et al. (2005) suggested the use of the cross correlation of DLAs and Lyman-break galaxies (LBGs) to observationally constrain the masses of the DM haloes of DLA host galaxies. Cooke et al. (2006) applied this technique to a large observed sample of DLAs and LBGs at $z \sim 3$, and found that DM haloes in the mass range above reproduce the cross-correlation length of DLAs and LBGs.

As discussed in the previous sections, the turnover at small virial velocities is most constrained by the velocity width distribution of low-ions associated with DLAs and is most likely attributable to feedback effects due to star formation. The decline at large virial velocities and masses is due to the decline of the space density of DM haloes.

The incidence rate in the numerical simulations of Razoumov et al. (2008) shows a similar peak, albeit shifted to somewhat smaller masses/virial velocities than our model requires to fit the kinematical data of the DLAs. This is perhaps not surprising — Razoumov et al. (2008) find that the velocity widths in their simulations fall somewhat short of those observed. Their simulation also takes into account DLAs that are not contained within any halo i.e. intergalactic DLAs.

The numerical simulations of Pontzen et al. (2008) show a sharper peak centred on virial velocities of 30-80 km s^{-1}. Such a sharp peak at rather low virial velocities appears, however, at odds with the observed velocity widths of the low-ion absorption in DLAs. In the simulations of Pontzen et al., the decline of the contribution to the incidence rate with increasing mass is much faster than the decline of the space density of massive haloes. This fast decline is due to a flattening of the absorption cross-section with increasing mass in massive haloes (Pontzen et al., Figure 4). This is the main reason that the numerical simulations are a worse fit to the velocity width distribution than our model. It will be important to investigate if such a fast decline is a robust prediction of the numerical simulations. Note, however, that if this were indeed the case then the distribution of velocity width for a given virial velocity of the DM halo would have to change in order to be able to fit the data.

An observational handle on the masses of the emitters will be important for testing the models further. For this, a detection of the rest frame UV continuum radiation of the objects will be a crucial first step. Knowledge of the continuum emission would allow us to confirm that the emitters are indeed high-redshift galaxies and would give a more reliable measure of the star formation rate. Unfortunately, the expected continuum emission is very faint and detecting this emission will require imaging to the depth of the Hubble Ultra-Deep Field (Rauch et al. 2008).

4.5 Summary and Conclusions

We have considered an updated version of the Haehnelt et al. model for the kinematics of DLAs, in light of the discovery of a new population of extended low surface brightness Lyα emitters with a total inferred incidence rate similar to that of DLAs. The main differences with the modelling of Haehnelt et al. (2000) are the use of the Sheth-Tormen modification to the Press-Schechter formalism, an update of cosmological parameters, and the use of an exponential suppression of the cross-section for damped absorption for low virial velocities instead of a sharp cut-off.

Our main results are the following.

- The observed velocity width distribution of low-ions associated with DLAs can be fit with a model where the cross-section for damped absorption scales with the virial velocity of the halo as $\sigma \propto v_{\rm c}^{2.5}$, the absorption cross-section is suppressed in haloes with $v_{\rm c} \leq 50 - 70$ km s^{-1}, and the conditional velocity width is given by that in the simulations of Haehnelt et al. (or the very similar distribution of the simulations of Pontzen et al. 2008).

- The same model can fit the size distribution of the Rauch et al. Lyα emitters if the Lyα emission has a duty cycle of $f_{\rm d} = 0.2 - 0.4$, and the emission extends over an area that is larger than the cross-section for damped Lyα absorption by a factor $f_{\rm d}^{-1} = 2.5 - 5$.

- The maximum expected Lyα cooling luminosity due to collapsing gas in DM haloes falls short of the observed Lyα luminosities by a factor of three

to five, even for optimistic assumptions regarding the expected emission due to Lyα cooling. Furthermore, the expected dependence of the Lyα cooling luminosity on the virial velocity of DM haloes thereby maps into a luminosity function with a slope shallower than observed. Lyα cooling radiation should thus not contribute significantly to the Lyα emission for the majority of the objects, especially at the faint end of the Lyα luminosity function.

- The Lyα luminosity function is well fit by a simple model where the Lyα luminosity scales linearly with the mass of the DM halo and the emission is suppressed for low mass DM haloes. The Lyα luminosity function can be fit for a wide range of duty cycles including the duty cycle required to simultaneously explain the kinematic properties of DLAs and the cumulative incidence rate inferred from the observed size distribution of the Lyα emitters.

- Our model predicts that the bulk of the contribution to the incidence rate of DLAs comes from absorption systems hosted in DM haloes with virial velocities in the range from 50-200 km s^{-1} and masses in the range 10^{10} to $10^{12} M_\odot$. The cut-off for damped absorption occurs at somewhat higher virial velocities than suggested by numerical simulations, which attempt to simulate the gas distribution and kinematics of DLAs self-consistently. These simulations, however, fall short of reproducing the observed velocity width distribution of low-ions in DLAs. If the suppression of the cross-section for damped Lyα absorption in haloes with virial velocities up to 70 km s^{-1} is indeed real, then feedback due to star formation at high redshift has to be more efficient in removing gas — even from rather deep potential wells — than is assumed in most models of galaxies formation and numerical simulations. Alternatively, the simulation (and our model) may underestimate the effect of stellar feedback on the velocity width of absorbers hosted by DM haloes with small virial velocities. This is plausible given the fact that the simulations still fail to reproduce realistic galactic winds.

With the discovery of a faint population of Lyα emitters, most plausibly identified with the population of DLA/LL host galaxies, we finally have a handle

on their space density, sizes and (in conjunction with models like the one presented here) masses and virial velocities. As discussed extensively by Rauch et al. (2008), the large inferred space density of the population of faint Lyα emitters is similar to that of dwarf galaxies in the local Universe. In the picture that emerges, DLAs are hosted by the galaxies that, in the context of the now well-established ΛCDM paradigm for structure formation, are expected to become the building blocks of typical galaxies like our Milky Way.

Chapter 5

Lyα Radiative Transfer in DLAs

This chapter has been submitted for publication in the Monthly Notices of the Royal Astronomical Society under the title *Faint extended Lyα emission due to star formation at the centre of high column density QSO absorption systems*. It has been reproduced here in a similar form, with the only substantial change being the removal of the description of the radiative transfer algorithm, to avoid overlap with Chapter 3.

5.1 Introduction

Rauch et al. (2008, hereafter R08) recently reported the results of an ultra-deep spectroscopic survey for low surface brightness Lyα emitters at redshift $z \sim 3$. A 92 hour long exposure with the ESO VLT FORS2 instrument yielded a sample of 27 faint line emitters with fluxes of a few times 10^{-18} erg s^{-1}cm^{-2}, which they argue are likely to be dominated by Lyα. They further conclude that the large comoving number density, 3×10^{-2} h_{70}^3 Mpc^{-3}, and the large covering factor $dN/dz \sim 0.2 - 1$ suggest that the emitters can be identified with the elusive host population of damped Lyα systems (DLAs) and high column density Lyman

limit systems. Chapter 4, building on the successful model for DLAs of Haehnelt, Steinmetz & Rauch (1998, 2000), presented a simple model that simultaneously accounts for the kinematic properties and incidence rate of the observed DLAs *and* the luminosity function and the size distribution of the R08 emitters in the context of the ΛCDM model for structure formation. The model assumes a simple relation between the size of the damped absorption and Lyα emission regions, and proposes that the Lyα luminosity is proportional to the total halo mass. We further corroborated the claim that cooling radiation is not expected to contribute significantly to the observed Lyα emission, and that the emitters are most likely powered by star formation. In the model, DLAs are small galaxies hosted by DM haloes with masses in the range $10^{9.5}$ to 10^{12} $M_\odot$ and have rather large low surface brightness Lyα haloes that extend to radii of up to 50 kpc or larger.

In order to fit the observed size distribution of the faint Lyα emitters, in Chapter 4 we assumed that the Lyα emission extends to radii somewhat larger than is required to reproduce the incidence rate for DLAs. However, no modelling of the gas distribution or Lyα radiative transfer was done. We present such modelling here to investigate whether the sizes, surface brightness profiles and spectral line shapes can be reproduced with simple but plausible assumptions for the distribution and the physical properties of the gas in the DM haloes suggested by our previous modelling to be the hosts of the faint emitters.

Our modelling is most similar to that of Dijkstra et al. (2006a, hereafter DHS06) and Verhamme et al. (2006), who modelled Lyα radiative transfer in collapsing protogalaxies and high-redshift galaxies. In many instances, we make similar assumptions to these authors, but our code was developed independently.

This chapter is structured as follows. In Section 5.2, we discuss our assumptions for the distribution and the physical properties of the gas. We also show the dependence of the surface brightness profile and the spectral line shapes on these assumptions. In Section 5.3, we present the results for a consistent model of the size distribution and the luminosity function of the faint Lyα emitters.

5.2 Lyα Radiative Transfer in DLAs / Faint Lyα Emitters

5.2.1 A Simple Spherically Symmetric Model for the Spatial Distribution and Kinematics of the Gas

Our knowledge of the spatial distribution and kinematics of the neutral hydrogen in DLAs / faint Lyα emitters is still somewhat limited. The statistics of the occurrence of DLAs and their column density distribution give us integral constraints on the spatial distribution of the gas, while the velocity distribution of low-ionisation species tracing neutral hydrogen gives us some indication of the velocity range of bulk motions. The bulk motions of the gas appear to have velocities that range from a few tens of km/s to several hundred km/s. The relative contribution of ordered and random motions and the role of gas infall and galactic winds is, however, still very uncertain.

If the identification of the faint Lyα emitters as DLA host galaxies is indeed correct, then this gives us, for the first time, constraints on the spatial extent of the gas in individual objects for a statistically representative sample. While there is still significant ambiguity due to the unknown duty cycle for Lyα emission (as discussed in Chapter 4), theoretical modelling gives us a handle on the masses and virial velocities of the haloes expected to host the DLAs / faint Lyα emitters.

Given these uncertainties, we have decided to follow DHS06 and explore the Lyα radiative transfer for sources at the centre of DM haloes with a range of masses, simple spherically symmetric gas distributions and either inflow or outflow with velocities that change as a power law with radius. This already leads to a rich variety of predicted surface brightness profiles and spectral shapes and allows us to study the influence of important physical parameters.

5.2.1.1 The Assumed Radial Distribution of Neutral Hydrogen

We begin by specifying the radial distribution of neutral hydrogen in a given halo. The total amount of hydrogen is set relative to the cosmic[1] mass fraction of

---

[1] The relevant cosmological parameters used in this Chapter are: $(h, \Omega_M, \Omega_b, \Omega_\Lambda, \sigma_8, n) = (0.7, 0.3, 0.045, 0.7, 0.9, 1)$.

hydrogen $f_H = \Omega_H/\Omega_m$. Throughout, we assume a helium fraction of $Y_p = 0.24$. There are a number of reasons to expect that the hydrogen mass fraction in a typical halo is lower than f_H. Firstly, baryons are subject to the smoothing effects of gas pressure. Secondly, gas that forms stars is both ionised and extremely compact. Stars will also ionise the neutral gas around them — this is a source of Lyα photons but also reduces the amount of HI that remains to scatter photons. Finally, stellar and AGN driven galactic winds are expected to drive gas out of galaxies into the IGM. As a first attempt at modelling this effect, we reduce the total mass of baryons in the halo to a fraction f_e of the cosmic value.

On top of reducing the amount of neutral hydrogen in a typical halo, the UV background will significantly ionise the gas in haloes too small to self-shield. It is also easier for galactic winds to drive gas out of small, shallow haloes. In Chapter 4, this effect was implemented via an exponential suppression of the cross-section of neutral hydrogen below a critical circular velocity $v_{c,0}$. This was necessary in order to fit the observed velocity width distribution of low-ion absorbers associated with DLAs. Here, we will implement this suppression by reducing the total amount of neutral hydrogen in haloes below $v_{c,0}$, such that the total mass of neutral hydrogen in a halo of mass M_v is,

$$M_{HI} = f_e f_H \exp\left(-\left(\frac{v_{c,0}}{v_c}\right)^{\alpha_e}\right) M_v. \tag{5.1}$$

We use[1] the fiducial parameters $\alpha_e = 3$, $v_{c,0} = 50$ km s^{-1}.

For the radial distribution of the gas, we assume an NFW profile (Navarro et al. 1996) at $z = 3$. Following the simulations of Maller & Bullock (2004, Equation (9)), we alter the NFW profile to give the halo a thermal core at $\simeq 3R_s/4$. The profile is then specified by the total mass of the halo M_v and the concentration parameter, $c_v \equiv r_v/r_s$. For dependence of the concentration parameter on the mass, we take the mean value of the $c_v - M_v$ correlation as given by Macciò et al. (2007),

$$c_v = c_0 \left(\frac{M_v}{10^{11} M_\odot}\right)^{-0.109} \left(\frac{1+z}{4}\right)^{-1}. \tag{5.2}$$

For the dark matter in the halo, Macciò et al. (2007) found that $c_0 \approx 3.5$, with a log-normal distribution and a scatter around this mean value of $\Delta(\ln c_v) = 0.33$,

---

[1]Note that α_e in this chapter was simply called α in Chapter 4. This change has been made in order to avoid confusion with the parameter α from DHS06, as defined in Equation (5.3).

in agreement of the results of Bullock et al. (2001) and Wechsler et al. (2002). As we will find later, a significantly larger c_0 is appropriate for the baryons; we will use the column density distribution of DLAs to constrain c_0 in Section 5.3.2. As we discuss further in Section 5.3.4, the gas in the DLAs / faint emitters can be expected to self-shield against the meta-galactic ionising UV background at $z \sim 3$. The corresponding self-shielding radius in the DM haloes we are studying here is generally smaller than the virial radius. We therefore set the outer radius of the HI to be the virial radius in our modelling, ignoring radiative transfer through the IGM. We set $T = 10^4$ K as a fiducial temperature.

5.2.1.2   The Assumed Kinematics of Neutral Hydrogen

The biggest uncertainty in our modelling is probably the kinematical state of the gas. We follow DHS06 and for our fiducial model we assume the gas to be infalling with a power-law radial velocity profile[1] parameterised by v_{amp} and α,

$$\boldsymbol{v}_{\mathrm{bulk}}(\boldsymbol{r}) = -v_{\mathrm{amp}} \left(\frac{r}{r_{\mathrm{v}}}\right)^{\alpha} \hat{\boldsymbol{r}}, \tag{5.3}$$

where r_{v} is the virial radius, for which we follow the definition of Maller & Bullock (2004). Values in the range $\alpha \in [-0.5, 1]$ should be reasonable. The upper limit describes the collapse of a uniform sphere (i.e. the spherical top-hat), while the lower limit represents the accretion of massless shells onto a point mass ($v^2 \sim GM/r$). A spherical top-hat would have $v_{\mathrm{amp}} = v_{\mathrm{c}}$.

While gas infall will certainly be an important feature of the gas kinematics, star formation driven outflows are also likely to play a role (see Veilleux et al. 2005, for a review). Note that for a spherically symmetric gas distribution, the red and blue side of the line profiles will just be interchanged if the gas is assumed to be outflowing instead of inflowing with the same velocity profile (ignoring the very slight effects of recoil and deuterium). For the more massive and more actively star-forming LBGs, galactic winds have been suggested to sweep up an expanding shell (Pettini et al. 2000, 2002, Verhamme et al. 2006, Schaerer & Verhamme 2008, Verhamme et al. 2008, Quider et al. 2009). We investigate such a configuration in Section 5.2.3.

---

[1]We use the modification to this law for $\alpha < 0$ given in Equation 10 of DHS06.
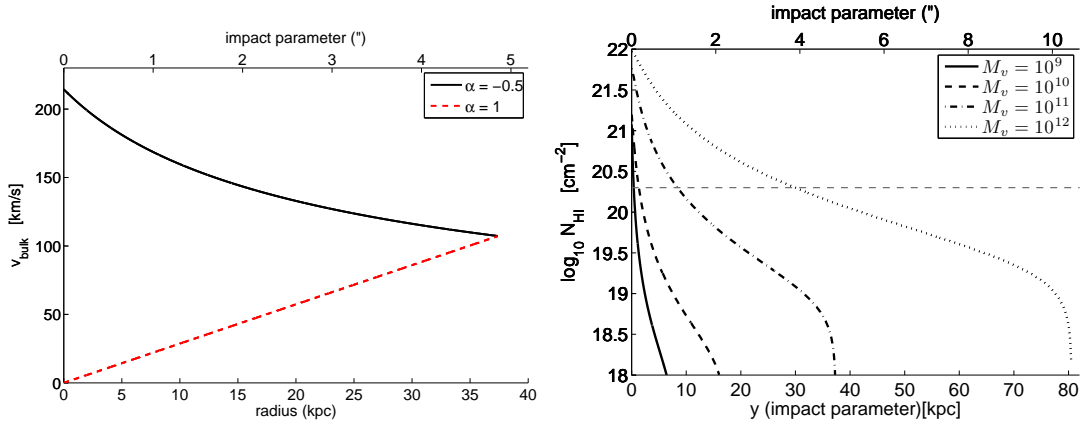
Figure 5.1: *Left*: The velocity profile for the fiducial halo, for differing values of α as shown in the legend. *Right*: The column density profiles for the fiducial model with the total mass as given in the legend in units of $M_\odot$. The column density is calculated along a sightline that passes all the way through the halo at a distance r from its centre. Note that the $10^9 M_\odot$ line has been boosted by a factor of 10^4 to make it visible on the given axes. The horizontal dashed line indicates the minimum column density of a DLA.

5.2.1.3   The Fiducial Model

In the previous chapter, we supported the conclusion of R08 that star formation is the most likely source for the faint emitters. Wolfe & Chen (2006) used continuum emission to place stringent limits on *extended* star formation in DLAs. We have thus assumed a centrally peaked emissivity — all photons are created at $\boldsymbol{r = 0}$.

Before we attempt to model the data of R08 in detail, we will consider the effect on the spectra and surface brightness distribution of altering the parameters of our model. Our fiducial model parameters are $(z, M_{\mathrm{v}}, c_0, f_{\mathrm{e}}, v_{\mathrm{amp}}, T) = (3, 10^{11} M_\odot, 25.3, 0.2, v_{\mathrm{c}}, 10^4 \mathrm{K})$. The values of c_0 and f_{e} that we have chosen will be justified in Section 5.3.2. The surface brightness S scales with the total luminosity $L_{\mathrm{Ly}\alpha}$, which will be given in the caption to each figure. The values of the luminosity chosen will be justified in Section 5.3.3. The velocity and column density profiles for the fiducial model are shown in Figure 5.1, where the column density is as seen along a sightline that passes all the way through the halo at an impact parameter y.

5.2.2 Lyα Radiative Transfer in Individual Haloes with Gas Infall

In this section, we will consider the effects of changing the most important parameters in the model: mass, concentration, velocity profile, baryon fraction and temperature.

5.2.2.1 The Effect of Halo Mass and Concentration

The models of Chapter 4 give us a handle on the masses of the haloes that host DLAs. Figure 5.2 considers haloes with masses of $M_{\rm v} = 10^9, 10^{10}, 10^{11}, 10^{12} M_\odot$, which at $z = 3$ correspond to $v_{\rm c} = 23, 50, 107, 231$ km s^{-1}, $r_{\rm v} = 8, 17, 37, 81$ kpc, $b_{\rm max} = 1.05, 2.25, 4.9, 10.5$ arcsec, where $b_{\rm max}$ is the angular radius corresponding to $r_{\rm v}$.

We see that, as the mass increases, the escaping photons emerge bluer. This is because, as we add more gas, the central column densities increase and the photons must shift further from line centre in order to escape. The $\alpha = 1$ profiles are increasingly double-peaked for lower masses, while the $\alpha = -0.5$ profiles only ever have one, blue peak. This is because the innermost region of the $\alpha = 1$ halo has the smallest bulk velocity, and thus most resembles the uniform, static sphere. As the mass of the halo increases, the bulk velocity at the centre of the halo increases, and the amount of energy transferred between the gas and photons in each scattering is increased, favouring one of the two peaks (the blue/red peak for inflowing/outflowing gas respectively). The surface brightness profile shows that the dominant effect in increasing the mass is that the virial radius (which we have assumed to be the outer radius of the Hı) increases. The $\alpha = -0.5$ profile is much more centrally peaked than the $\alpha = 1$ profile. The reason for this is that the larger bulk velocities at the centre of the $\alpha = -0.5$ halo can shift the photon into the wings of the spectral line, resulting in reduced spatial diffusion.

For the concentration parameter, we have considered the values $1.8, 3.5, 9.4$ and 25.3. The spectra and surface brightness profiles for these models are shown in Figure 5.3.

As the concentration increases, the photons generally emerge bluer. The $\alpha = 1$ profile becomes *more* double-peaked as the concentration increases, because the Hı column density increases at smaller radii, where the bulk velocity is lower. The
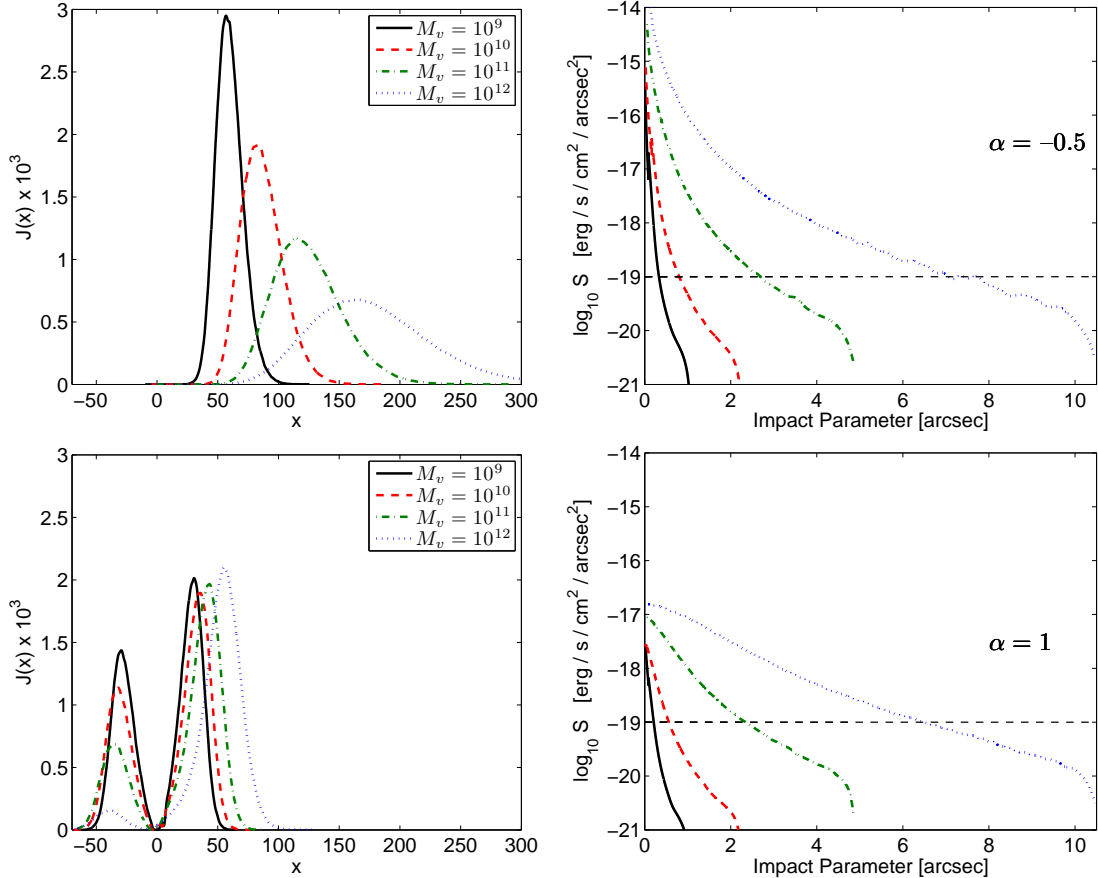
Figure 5.2: Spectra (left) and surface brightness profiles (right) for emission in haloes with total mass as given in the legend in units of $M_\odot$. The top panels are for $\alpha = -0.5$. In the order given in the legend, the luminosities are $L_{\mathrm{Ly}\alpha} = (9.6 \times 10^{-6}, 0.88, 22, 240) \times 10^{42}$ erg s^{-1}. The bottom panels are for $\alpha = 1$, with $L_{\mathrm{Ly}\alpha} = (4.8 \times 10^{-7}, 0.044, 1.1, 12.1) \times 10^{42}$ erg s^{-1}. These values for the luminosity will be justified in Section 5.3.3. Note that the surface brightness for the $M = 10^9 M_\odot$ model has been multiplied by a factor 10^4 to enable plotting on the same axes. As the mass increases, the escaping photons emerge bluer, and are scattered to larger radii in the larger haloes. The dashed horizontal line is the detection threshold of the Rauch et al. emitters.
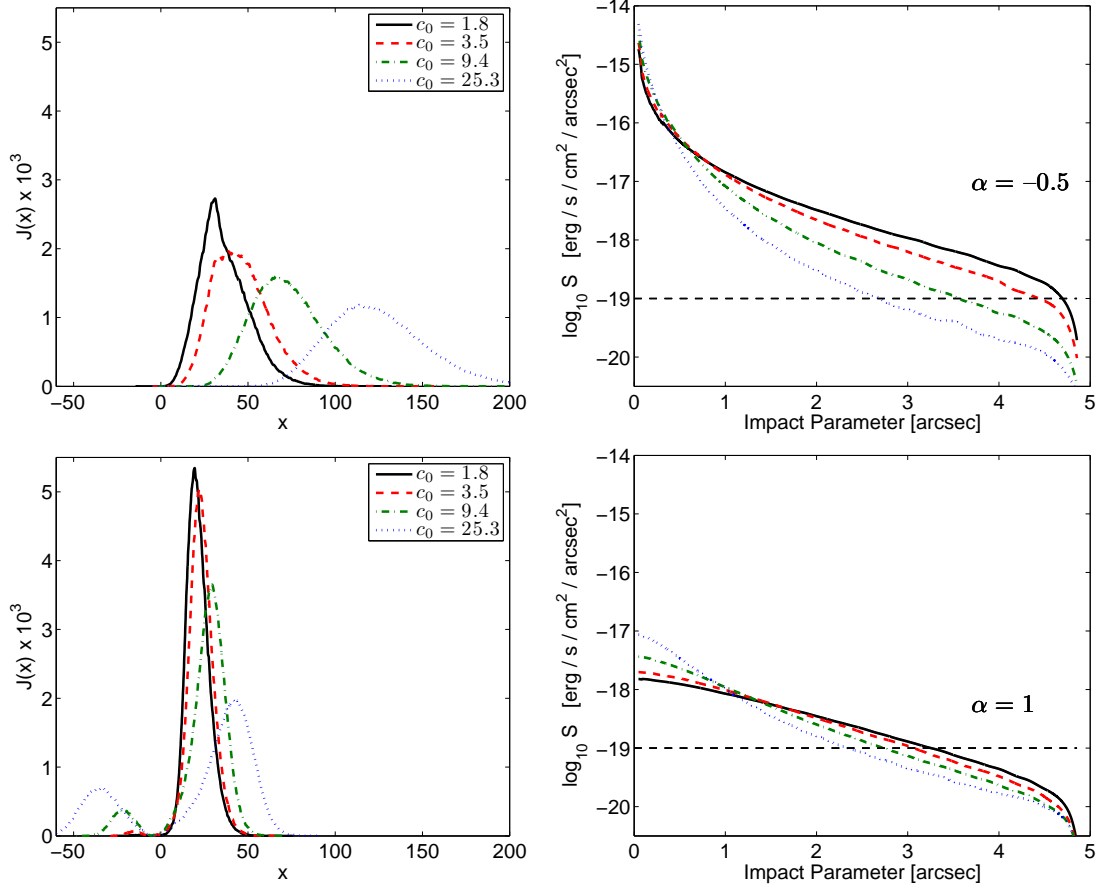
Figure 5.3: Spectra and surface brightness profiles for emission in haloes with concentration parameter c_0 as given in the legend. The top panels are for $\alpha = -0.5$, for which $L_{\mathrm{Ly}\alpha} = 2.2 \times 10^{43}$ erg s^{-1}. The bottom panels are for $\alpha = 1$, for which $L_{\mathrm{Ly}\alpha} = 1.1 \times 10^{42}$ erg s^{-1}. As the baryon distribution becomes more centrally concentrated, the photons emerge bluer. The photons are scattered at larger radii in the less concentrated haloes. The dashed horizontal line is the detection threshold of the Rauch et al. emitters.

surface brightness profile is also more centrally peaked for higher concentrations, as more scatterings occur at smaller radii.

5.2.2.2   The Effect of Baryonic Fraction/Column Density

The effect of changing the baryonic fraction f_e is shown in Figure 5.4. As baryons are removed from the halo, the spectrum shifts toward $x = 0$ and the surface brightness profile becomes more centrally peaked, as there is less gas in the outer parts of the halo to scatter the photons. The baryon fraction where the photons are not scattered efficiently anymore to the virial radius (where we have the gas distribution assumed to cut-off) corresponds to a HI column density[1] of about 10^{16} cm^{-2}. Note, however, that for $f_e \ll 0.1$, the gas in the haloes would not be able to self-shield against the meta-galactic UV background at $z \sim 3$ so the model would be internally inconsistent for such small baryonic fractions. For very small f_e and $\alpha = -0.5$, some of the photons can escape the halo without scattering at all, creating a very narrow peak at $x = 0$. Some of the spectra also show a trough at $x \approx 6$ due to deuterium.

5.2.2.3   The Effect of Velocity Amplitude

In this section, we consider the effect of decreasing v_{amp}. For this section and the next (5.2.2.4), the fiducial model is different to that used previously: $(z, M_v, c_0, f_e, v_{amp}, T) = (3, 10^{11} M_\odot, 3.5, 1, v_c, 10^4 \text{ K})$.

The results are shown in Figure 5.5. Setting $v_{amp} = 0$ would result in $J(x)$ being symmetric about $x = 0$ (ignoring the small effects of deuterium and recoil). This tendency is seen clearly in both of the left plots. These plots also show that photons emerge bluer as the velocity of infall increases. Photons gain energy from head-on collisions with atoms, and the more energetic the atoms, the more energy is transferred between photons and gas.

The surface brightness plots show that the emission becomes more extended as the velocity is reduced. A rather flat surface brightness profile is characteristic of a uniform, static HI sphere. This is because the bulk velocity can give photons a "free ride" through the halo, Doppler shifting their frequency away from line

---

[1]Which is somewhat dependent on the spatial profile of neutral hydrogen and the velocity field.
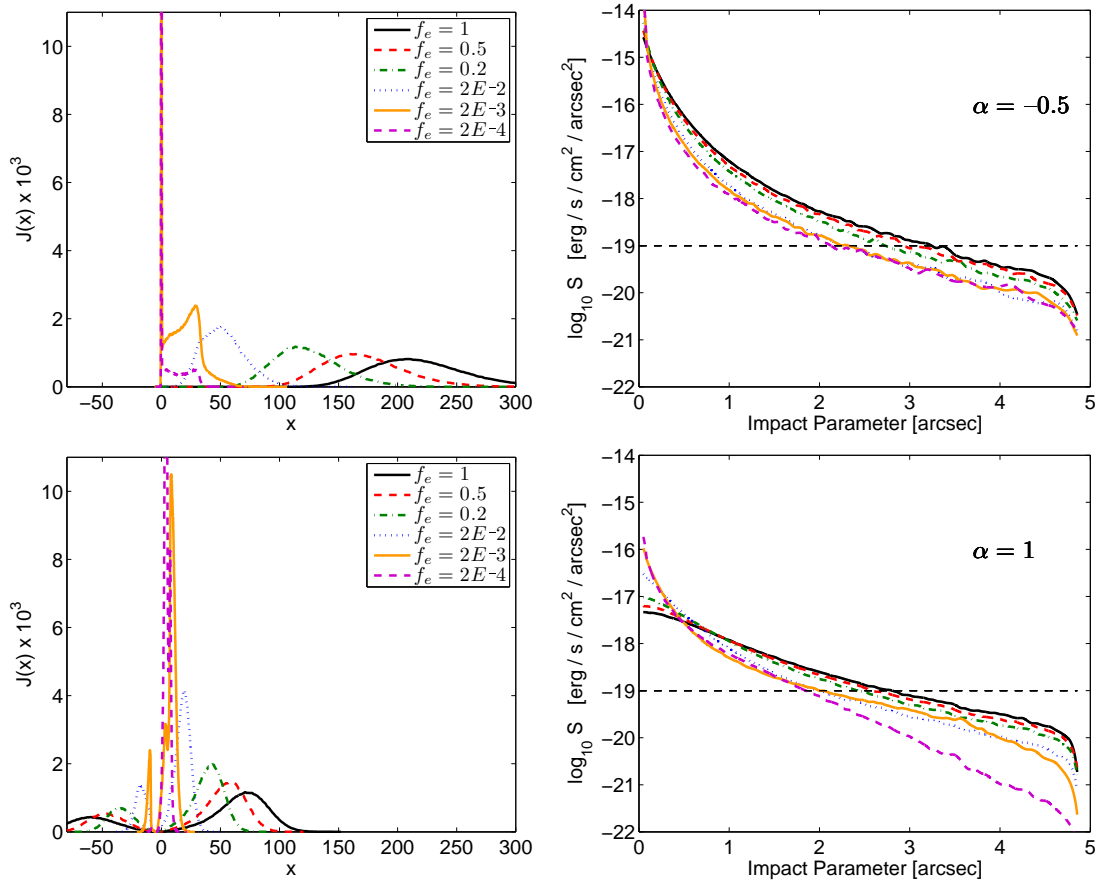
Figure 5.4: Spectra and surface brightness profiles for emission in haloes with baryon fraction f_e as given in the legend, where $f_e = 1$ corresponds to the cosmic value of the baryon fraction. The top panels are for $\alpha = -0.5$, the total luminosity is kept the same for each model at $L_{\mathrm{Ly}\alpha} = 2.2 \times 10^{43}$ erg s^{-1}. The bottom panels are for $\alpha = 1$, with $L_{\mathrm{Ly}\alpha} = 1.1 \times 10^{42}$ erg s^{-1}. As f_e decreases, the spectral shift decreases and the surface brightness becomes more centrally peaked. The dashed horizontal line is the detection threshold of the Rauch et al. emitters.

centre in the fluid frame without changing x in the laboratory frame. In the $\alpha = -0.5$ case, the peak surface brightness is reduced by more than an order of magnitude by this effect. It is also worth noting that as v_{amp} decreases, α has a reduced effect on the profile.

5.2.2.4 The Effect of Temperature

The effect of altering the temperature is shown in Figure 5.6. Note that the spectrum is given as a function of velocity ($v \equiv -x\, v_{\mathrm{th}}$), as x itself is temperature dependent ($\propto 1/\sqrt{T}$). For the $\alpha = -0.5$ case, there is no dependence on the temperature because the photon begins its flight with a frequency (in the fluid frame) in the scattering wings, and is unlikely to return to the Doppler core. Remember that the scattering cross-section does not depend on T in the Lorentz wing of the profile. In the $\alpha = 1$ case, the effect of temperature is minimal. The red peak disappears at lower temperatures due to the corresponding increase in the scattering cross-section, $\sigma_x \propto 1/\Delta\nu_{\mathrm{D}} \propto 1/\sqrt{T}$, when x is small.

5.2.3 Expanding Shells

For the much brighter Lyα emission seen in many LBGs, the emerging Lyα photons are systematically redshifted by several hundred km s^{-1}. This is generally attributed to backscattering of the Lyα radiation from a wind-driven expanding shell. Verhamme et al. (2006) used a Lyα RT code similar to ours to calculate the emergent spectrum from an expanding shell. We will investigate here whether this scenario could apply to the R08 emitters. We consider a shell of HI, where the inner radius is a fraction f_r of the outer radius r_{max}. The shell is expanding at a uniform velocity V_{exp}, and has a column density of N_{HI}. The temperature is set by the Doppler velocity[1], b_T. Our fiducial model has the parameters: $(r_{\mathrm{max}}, f_r, V_{\mathrm{exp}}, N_{\mathrm{HI}}, b_T) = (30 \text{ kpc}, 0.9, 300 \text{ km s}^{-1}, 2 \times 10^{20} \text{ cm}^{-2}, 40 \text{ km s}^{-1})$, similarly to the fiducial model of Verhamme et al. (2006). For the outer radius of the shell r_{max}, we have chosen a value similar to the models of the previous sections.

Figure 5.7 shows the effect of altering the parameters that Verhamme et al. found to be most important: the column density and the expansion velocity. Note

---

[1]This is defined in the same way as the thermal velocity dispersion, with a possible contribution from a turbulent velocity dispersion, added in quadrature.
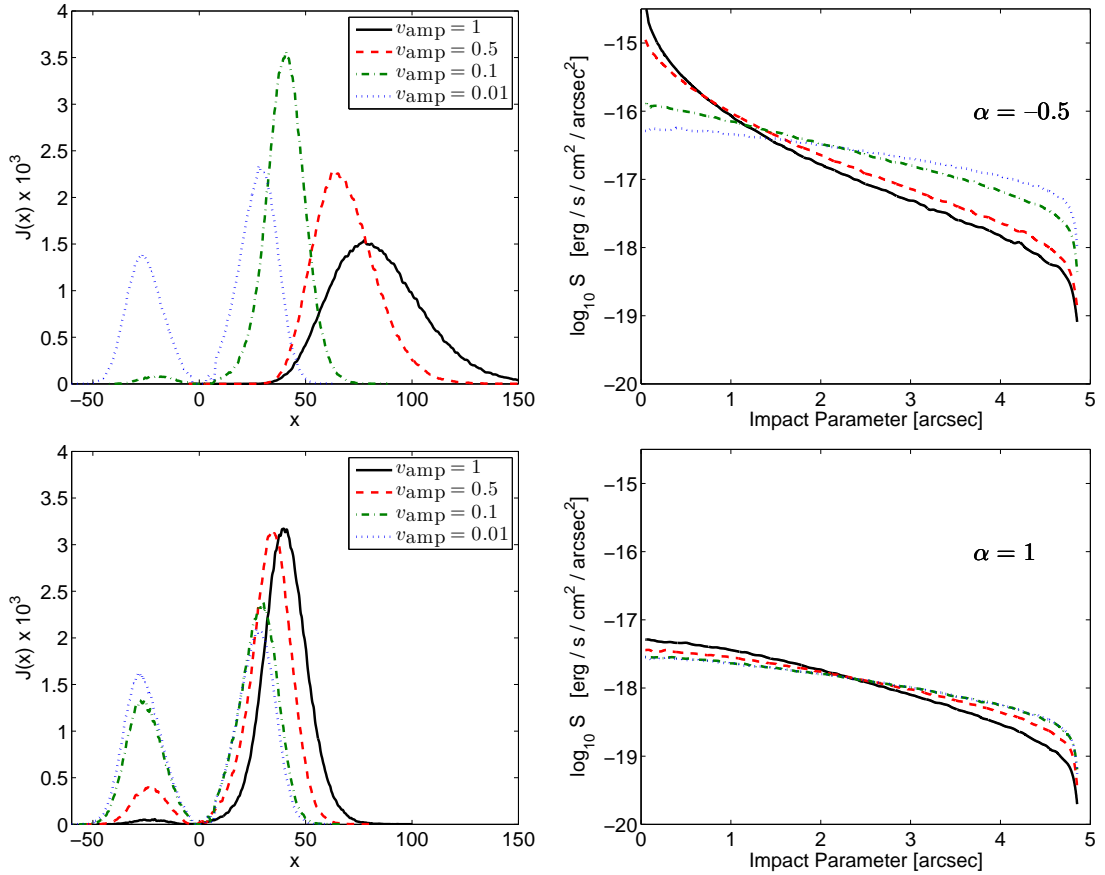
Figure 5.5: Spectra and surface brightness profiles for DLAs in haloes with v_{amp} as given in the legend in units of the virial velocity. The top panels are for $\alpha = -0.5$, for which $L_{\mathrm{Ly}\alpha} = 1.1 \times 10^{44}$ erg s^{-1}. The bottom panels are for $\alpha = 1$, for which $L_{\mathrm{Ly}\alpha} = 5.5 \times 10^{42}$ erg s^{-1}. As the velocity decreases, the spectrum begins to resemble the double-peaked static sphere profile. The surface brightness profile flattens as the velocity decreases — where the bulk velocity is low, the photons must random walk out of the Doppler core by scattering; they will not be given a "free ride" by the fluid flow.
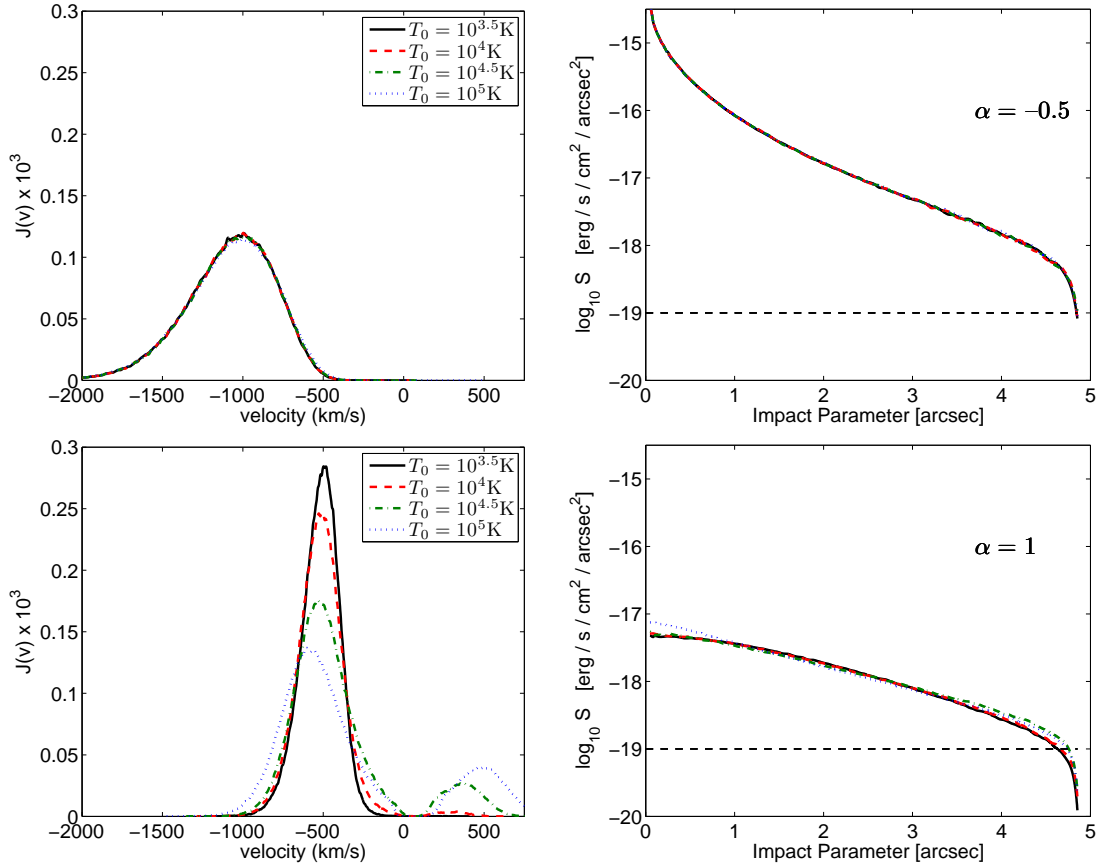
Figure 5.6: Spectra and surface brightness profiles as a function of *velocity* for DLAs in haloes with temperature T_0 as given in the legend. The top panels are for $\alpha = -0.5$, for which $L_{\mathrm{Ly}\alpha} = 1.1 \times 10^{44}$ erg s^{-1}. The bottom panels are for $\alpha = 1$, for which $L_{\mathrm{Ly}\alpha} = 5.5 \times 10^{42}$ erg s^{-1}. For the $\alpha = -0.5$ case, there is no dependence on the temperature because the photon begins its flight with frequency (in the fluid frame) in the scattering wings, and is unlikely to return to the Doppler core. In the $\alpha = 1$ case, the effect of temperature is minimal. The red peak disappears at lower temperatures due to the corresponding increase in the scattering cross-section, $\sigma_x \propto 1/\Delta\nu_{\mathrm{D}} \propto 1/\sqrt{T}$, when x is small.

that, for small column densities (upper panels), a certain fraction of photons is able to escape directly without scattering. These photons form a very sharp peak at $x = 0$, and at small impact parameter, which has been removed from these plots for clarity.

As the column density increases (top panels), the spectrum becomes redder, and the small blue peak disappears, as the photons must scatter further from line centre in order to escape. The most significant change in the surface brightness profile occurs for small column densities, where some of the photons are able to escape directly, leaving fewer to scatter at large radii.

As the expansion velocity increases (bottom panels), the back-scattering mechanism becomes more pronounced. Photons that scatter off the far side of the shell back through its interior are far enough from line centre to escape through the front of the shell. This mechanism creates the two red peaks (the reddest peak comes from photons that backscatter more than once). At small velocities, we approach a profile similar to the static sphere.

The surface brightness profiles are very flat when compared to the infall/outflow models of the gas in an NFW halo, which we considered previously. Qualitatively, they appear much flatter than the profiles of the R08 emitters, almost all of which show a central peak. One way to produce a central peak for a shell geometry is for the column density to be low enough for photons to be able to escape directly; the resolution of the instrument then broadens the delta function at $y = 0$ into a central peak. This would limit the column density of the shell to $N_{\mathrm{HI}} \lesssim 2\times10^{19}$ cm^{-2}. We conclude that the R08 emitters appear unlikely to be halo-scale expanding shells of H I around a central Lyα source.

5.2.4 Summary of General Trends of the Lyα Emission

The radial (column) density distribution and the velocity field are the physical properties that most strongly affect the spectral distribution of the Lyα emission in our modelling. For a spherical density distribution with neither outflow nor infall, the distance between the peaks increases with increasing optical depth in the same way as the uniform static slab solution. Infall and outflow lead to a suppression of the red/blue peak and an increased shift of the opposite peak. The suppression increases with increasing velocity amplitude and optical depth.
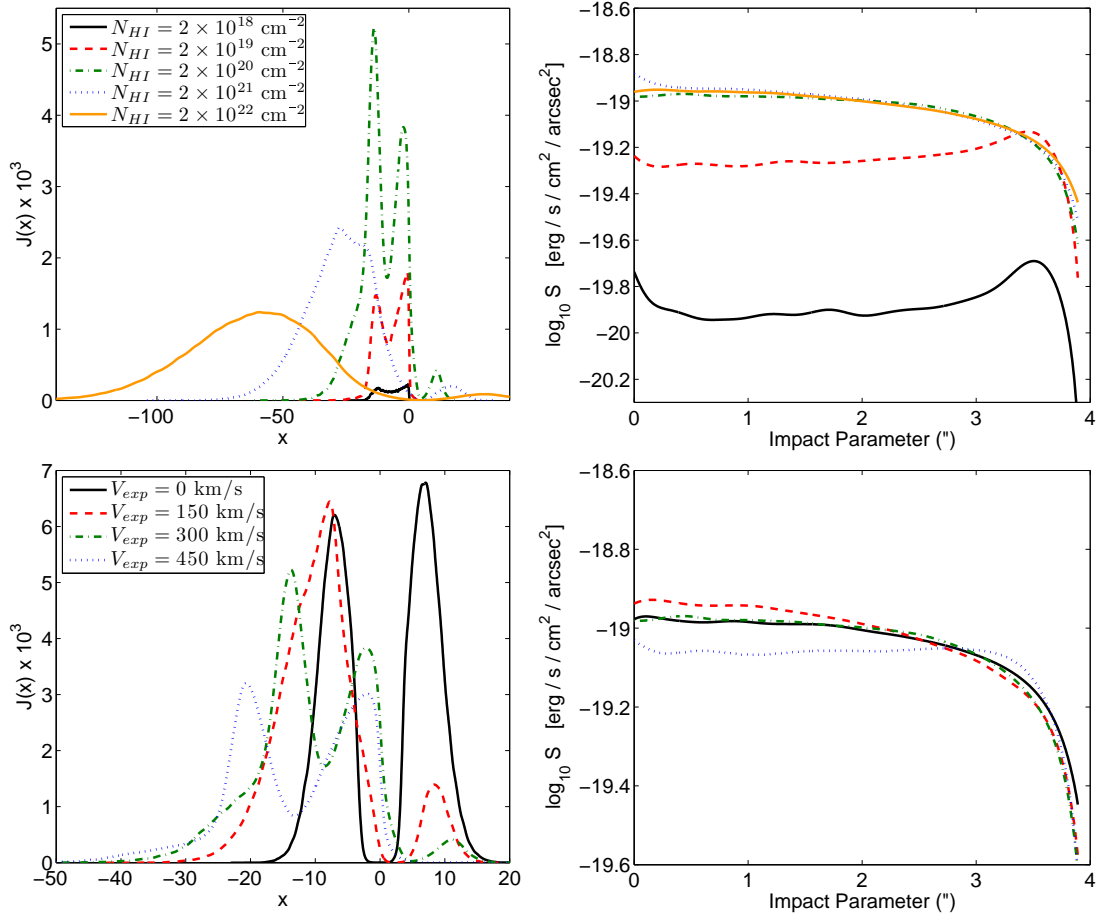
Figure 5.7: Spectra and surface brightness profiles for the modelling of expanding shells. The panels show the effect of altering the parameters that Verhamme et al. (2006) found to be most important, the column density and the expansion velocity, as given in the legend. Note that, for small column densities (in the upper panels), a certain fraction of photons are able to escape directly without scattering. These photons form a delta function at $x = 0$ and at small impact parameter, which has been removed from these plots for clarity. As the column density increases, the spectrum becomes redder, and the small blue peak disappears. The most significant change in the surface brightness profile comes at small column densities as photons are able to escape directly, leaving less to be scattered at large radii. As the expansion velocity increases, the back-scattering mechanism becomes more pronounced, creating the two red peaks. At small velocities, the results become similar to those for a static sphere.

The surface brightness profile depends strongly on the radial velocity profile. With increasing amplitude of the bulk motion, the diffusion in frequency space is accelerated and the emission becomes more centrally peaked. In our model with increasing amplitude towards decreasing radius ($\alpha = -0.5$), the average bulk motions are larger and the effect is more pronounced. For an expanding shell, the photons can travel unimpeded until they encounter the shell, which leads to a rather flat surface brightness profile.

The photons diffuse radially until the column density of neutral hydrogen density drops to values around 10^{16} cm^{-2}, a value somewhat dependent on the spatial profile of neutral hydrogen and the velocity field. The faint extended Lyα emission should thus have a rather sharp edge that is defined by the surface inside which the gas is able to self-shield and the optical depth rises rapidly.

5.3   Modelling the Rauch et al. Emitters

5.3.1   Surface Brightness Profiles and Spectral Shapes

We begin with a qualitative summary of the properties of the R08 emitters. Note that due to the faintness of the sources, the spectral and spatial profiles are rather noisy, making it difficult to identify signatures of inflow (more prominent blue peak) or outflow (more prominent red peak)[1]. As discussed in R08, for 12 of the 27 spectra only a single emission peak is visible while six/three of the spectra show a weak secondary blue/red counter-peak. The remaining spectra are extended in frequency space without a clear peak structure. The widths of the spectral peaks range from $\sim 250 - 1000$ km s^{-1}, which corresponds to $\Delta x \sim 20 - 80$ for gas with a temperature of 10^4 K. The surface brightness profiles are predominantly centrally peaked with wings that often extend well beyond the Gaussian core of the PSF. This is particularly true of the brightest sources, while the fainter sources are more difficult to characterise due to the noise.

---

[1]Recall also that this can be more complicated for the case of an outflowing shell, as there are then two red peaks.

5.3.2 Simultaneous Modelling of DLA Properties

Modelling the radial distribution of neutral hydrogen in DM haloes allows us to calculate the column density distribution along sightlines that intersect the haloes. Comparison with the observed column density distribution of DLAs provides a useful constraint in this regard.

The column density distribution is defined such that the number of systems ($d^2\mathcal{N}$) intersected by a random line of sight between absorption distance[1] X and $X + dX$, with H$_I$ column density between N_{HI} and $N_{HI} + dN_{HI}$ is,

$$d^2\mathcal{N} = f(N_{HI}, X) \ dX \ dN_{HI}. \tag{5.5}$$

For our model, we calculate this quantity using the Press-Schechter formalism. We need two ingredients. The first is $n_M(M, X)$, the mass function of dark matter haloes, as calculated by Sheth & Tormen (2002). The second ingredient is the column density of neutral hydrogen in a given halo (of mass M at absorption distance X), as a function of the (physical) impact parameter y, $N_{HI}(y|M, X)$. This is calculated from the neutral hydrogen density as a function of radius. Given that N_{HI} is a monotonically decreasing (and thus invertible) function of y, the region between N_{HI} and $N_{HI} + dN_{HI}$ is an annulus with cross-sectional area $d(\pi y^2)$. Hence, we can write the column density distribution as,

$$f(N, X) = \frac{c}{H_0} \int n_M(M, X) \left| \frac{d(\pi y^2)}{dN_{HI}}(N_{HI}|M, X) \right| \ dM. \tag{5.6}$$

The results are shown in Figure 5.8. The most important parameters (given that we integrate over all M) are the normalisation of the concentration parameter for the baryons c_0, and the baryon fraction f_e relative to the cosmic value. A good fit to the observed column density distribution is obtained for $c_0 \approx 25.3$ and $f_e \approx 0.2$. The figure demonstrates the effect of altering these two parameters. Decreasing f_e decreases the overall normalisation, while c_0 mostly affects the high column density end of the distribution. Changing $v_{c,0}$ has a comparatively small effect.

---

[1]The absorption distance is defined by

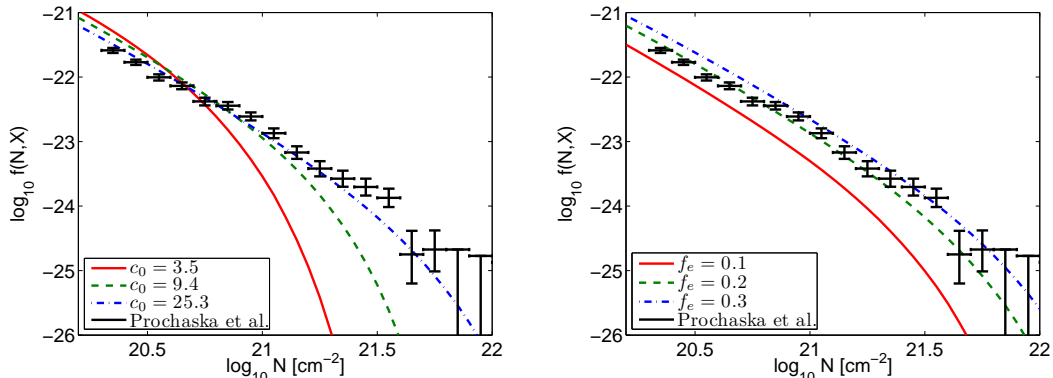$$dX \equiv \frac{H_0}{H(z)}(1+z)^2 \ dz \ . \tag{5.4}$$

.

Figure 5.8: The column density distribution $f(N, X)$ for our model; the black crosses show the data of Prochaska & Wolfe (2009). The left panel shows the effect of changing the concentration parameter of the radial gas density profiles. The right panel shows the effect of altering the baryon fraction f_e (defined relative to the cosmic value).

Note that our model somewhat overpredicts the number of absorption systems with column densities below $N_{HI} = 20.3$ cm^{-2}, in the regime of Lyman Limit systems (LLs). In this column density range, the observed $f(N, X)$ flattens significantly (O'Meara et al. 2007), an effect that can be attributed to the inability of (super) LLs to self-shield completely against the meta-galactic UV background (Zheng & Miralda-Escudé 2002). Since we have not attempted to model the ionisation of the gas, in particular the self-shielding of the gas, in any detail, it is not surprising that our model does not reproduce this. In spite of this, the UV background should not affect our results for the population of predominantly neutral DLAs. Figure 5.4 shows that in the LLs regime the inferred size of the emission region depends weakly on column density.

Similarly to Chapter 4, we calculate the predicted probability distribution of the velocity width (v_w) distribution of low-ions in DLAs for our model as follows,

$$l(v_w, X) = \frac{c}{H_0} \int_0^\infty p(v_w | v_c(M)) n_M(M, X) \sigma_{DLA}(M, X) dM, \qquad (5.7)$$

where $p(v_w | v_c(M))$ is the conditional probability distribution as discussed in Section 4.2.2. The cross-section for damped absorption is given by $\sigma_{DLA}(M) = \pi y_{DLA}^2$, where $N_{HI}(y_{DLA} | M, X) = 10^{20.3}$ cm^{-2}. The result is shown in Figure 5.9,
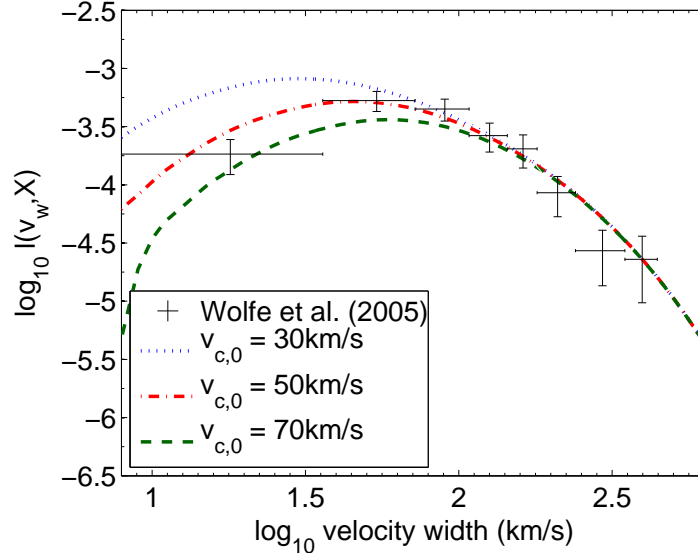
Figure 5.9: The velocity width distribution $l(v_w, X)$ of low-ionisation metal absorbers associated with DLAs. The black crosses show the observational data compiled in Figure 10 of Wolfe et al. (2005). The legend shows the parameter $v_{c,0}$, below which the baryonic fraction is assumed to be suppressed due to the effect of photoheating and/or galactic winds.

along with the observational data of Wolfe et al. (2005).

As in Chapter 4, our model fits the data well with values of $v_{c,0}$ in the range 50 - 70 km s^{-1}. We should point out that the probability distribution $p(v_w|v_c)$ was originally derived from simulations that do not include the effect of galactic winds and where the distribution of gas in a given halo is somewhat different from what we have assumed here (see Chapter 4 for a more detailed discussion).

We should emphasize that, rather than using a simple power-law scaling for the absorption cross-section of DLAs as in Chapter 4, we have used here a radial distribution of neutral hydrogen that is simultaneously consistent with the column density distribution of DLAs *and* the size distribution of the Rauch et al. emitters, as we will see in the next section.

5.3.3 The Size Distribution and Luminosity Function

We will not attempt to fit the rather noisy spectral and surface brightness profiles of individual R08 emitters here, but we will instead focus on the statistical properties of the population of emitters.

We calculate the cross-section weighted size distribution $dN/dz(> r)$ expected from our model as follows. The observations of Rauch et al. (2008) achieved a $1\,\sigma$ surface brightness detection limit of $S_0 = 10^{-19}$ erg/s/cm^2/arcsec^2. We calculate the expected observed size of our model emitters by determining the radius (r) at which the surface brightness drops below the R08 limit, $S(r) = S_0$.

This procedure gives the radius of the emitter as a function of the mass of the halo. We also need to specify the intrinsic Lyα luminosity $L_{\mathrm{Ly}\alpha}$ as a function of mass. Similarly to Chapter 4, we assume that the luminosity is proportional[1] to the total mass of neutral hydrogen,

$$L_{\mathrm{Ly}\alpha} = L_0 \left(\frac{M_{\mathrm{HI}}}{2.4 \times 10^9 M_\odot} \right) \; \mathrm{erg \; s}^{-1}. \qquad (5.8)$$

This means that the luminosity is subject to the same exponential suppression as the (neutral) gas content of DM haloes for small circular velocities.

We compare the size distribution in the form of the inferred cumulative incidence rate, $d\mathcal{N}/dz(> r)$, with the data of R08 in Figure 5.10. The curves have been normalised to $d\mathcal{N}/dz = 0.23$ by assuming that the emission occurs with a duty cycle f_{d}, $n_M^{\mathrm{emitters}} = f_{\mathrm{d}}\, n_M^{\mathrm{haloes}}$. The values of f_{d} for each model are given in the caption to the figure. The solid curves are for $\alpha = -0.5$, while the dashed curves are for $\alpha = 1$. The red and green curves assume $L \propto M_{\mathrm{HI}}$, with the values of L_0 as given in the legend. The blue curve shows the size distribution assuming that $r = r_{\mathrm{v}}$, that is, assuming that the emission is detected all the way to the virial radius.

As we have defined the size of the emitters at a fixed surface brightness level S_0, the observed size of the haloes becomes larger as L_0 increases. For fixed luminosity, the region with emission above this limit is smaller when $\alpha = -0.5$ than in the model with $\alpha = 1$, due to the more centrally concentrated surface

---

[1]The constants of proportionality are chosen so that without the suppression below $v_{\mathrm{c},0}$ and with $f_e = 0.2$, L_0 defined here has the same value as in Chapter 4.
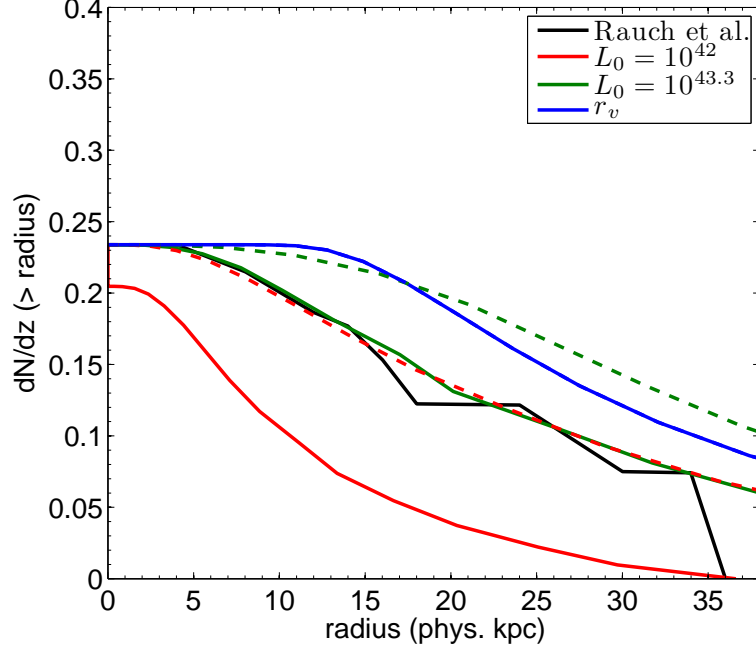
Figure 5.10: The cumulative size distribution dN/dz $(> r)$ of the Lyα emitters, compared with the observations of Rauch et al (black curve). The coloured solid curves are for $\alpha = -0.5$, while the dashed curves are for $\alpha = 1$. The red and green lines are for the $L \propto M_{\mathrm{HI}}$ model, with the values of L_0 as given in the legend. The blue curve assumes that $r = r_{\mathrm{v}}$, that is, assuming we can see emission all the way to the virial radius. The lines have been normalised to $dN/dz = 0.23$ assuming a duty cycle of the Lyα emission with f_{d}, such that $n_M^{\mathrm{emitters}} = f_{\mathrm{d}} \, n_M^{\mathrm{haloes}}$. The values of f_{d} for each model (in the order they appear in the legend) are $f_{\mathrm{d}} = 1, \mathbf{0.2}, 0.055$ for $\alpha = -0.5$ and $f_{\mathrm{d}} = \mathbf{0.28}, 0.07, 0.055$ for $\alpha = 1$. The models with the two values in bold correspond best to the data.

brightness profile. The size distribution flattens at small r due to the exponential suppression of the luminosity at low v_{c}.

Figure 5.10 shows that we can find values of L_0 that fit the observed cumulative size distribution well, where the value of L_0 depends on α. The required duty cycle is $\sim 20 - 28\%$, and is rather insensitive to α. The value of L_0 for $\alpha = -0.5$ is rather high, due to the very peaked surface brightness profiles in this case.

Figure 5.11 shows the corresponding luminosity distribution $n(> L_{\mathrm{Ly}\alpha})$, along with the R08 data (black solid curve). Note that the luminosity $L_{\mathrm{Ly}\alpha}$ predicted
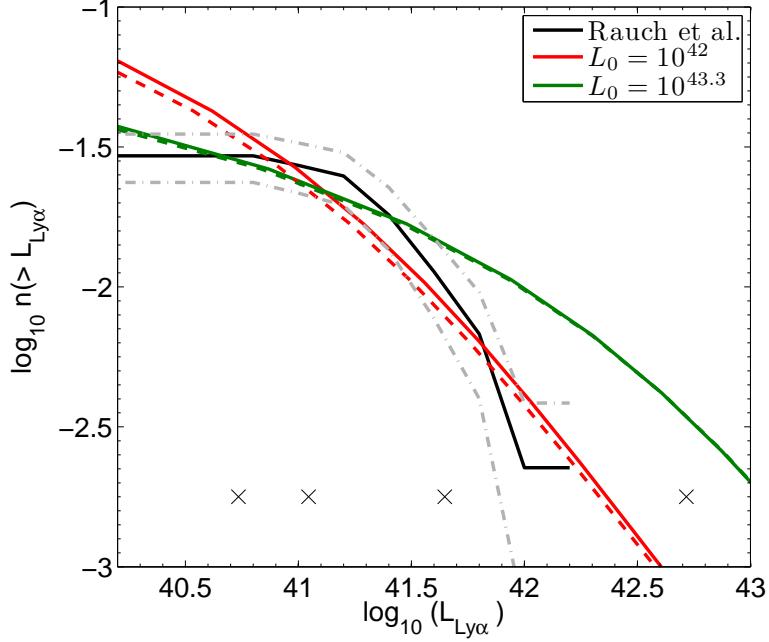
Figure 5.11: The cumulative luminosity function $n(> L_{\mathrm{Ly}\alpha})$ of our model, along with the Rauch et al. data (black solid curve with errors indicated by the grey dot-dashed curves). The same models are shown as in Figure 5.10, except that the duty cycle is chosen to match the luminosity function data. The parameters for each model (in the order they appear in the legend) are (with negligible dependence on α): $f_{\mathrm{d}} = 0.28, 0.07$. The black crosses indicate the luminosities of the four galaxies we will study in Chapter 6, arbitrarily shown at $n(> L_{\mathrm{Ly}\alpha}) = 10^{-2.75}$.

by our model is calculated by integrating the surface brightness inside the radius r where the surface brightness is above the observational limit. Photons that are scattered to radii where the surface brightness falls below this limit are lost in the noise; the observed luminosity is thus always less than the intrinsic luminosity. Note further that the observed luminosities have not been corrected for "slit losses". The actual luminosities may thus be a factor two or more larger.

Figure 5.11 shows the same models as in Figure 5.10, except that the duty cycle is chosen to fit the luminosity function data. The solid and dashed curves are very close, meaning that there is practically no dependence on α. The corresponding values of f_{d} are given in the caption to the figure.

The observed luminosity function is reproduced reasonably well by our model if we assume $L_0 = 10^{42}$ erg s^{-1}, the value required to match the observed size distribution for our model with $\alpha = 1$. This model predicts a somewhat steeper faint end slope than appears to be observed, but as discussed in R08 it is uncertain whether the turnover in the observed luminosity function is real or due to incomplete identification of emitters close to the detection threshold. Should the turnover consolidate with deeper data then this may suggest a somewhat sharper cut-off of the efficiency for Lyα emission in shallow potential wells. The required duty cycle is $f_{\rm d} = 0.28$, which is comparable to the value required to fit the observed size distribution. A model with parameters $\alpha = 1$, $L_0 = 10^{42}$ erg s^{-1}, and $f_{\rm d} \sim 0.28$ therefore fits both the observed size and luminosity distribution of the R08 emitters. As previously discussed, the model with $\alpha = -0.5$ has strongly centrally peaked emission. As is apparent from Figure 5.11, this leads to a mismatch with the observed luminosity function if we fix $L_0 = 10^{43.3}$ to fit the observed size distribution for this value of α. Even for a significantly smaller duty cycle of $f_{\rm d} = 0.07$, we cannot match the shape of the observed luminosity function, which in this case is significantly steeper than predicted by the model over the full range of luminosities.

We conclude that we can successfully reproduce both the absorption properties of DLAs and the Lyα emission data of R08 using a self-consistent model with centrally concentrated, star formation powered Lyα production with a duty cycle of $\sim 25\%$, coupled with radiative transfer effects that set the observed size of the emitters *if* the velocity field of the gas facilitates the scattering of the photons to large radii with moderate central bulk velocities as in the model with $\alpha = 1$. Our model's success in simultaneously reproducing the absorption properties of DLAs significantly strengthens the assertion of Rauch et al. (2008) that the faint emitters are in fact the host galaxies of DLAs.

Finally, we calculate $\mathrm{d}^2\mathcal{N}/\mathrm{d}X/\mathrm{d}\log_{10}M$, the contribution to the incidence rate from haloes of different masses. The result is shown in Figure 5.12. The majority of DLAs/emitters have masses in the range $10^{9.5}-10^{12}M_\odot$ for all models. This is a similar range of masses to that found in the numerical simulations of Nagamine et al. (2007), Razoumov et al. (2008), Pontzen et al. (2008), Tescari et al. (2009). We refer to Chapter 4 for a more detailed comparison of our prediction of $\mathrm{d}^2\mathcal{N}/\mathrm{d}X/\mathrm{d}\log_{10}M$ with that of numerical simulations. The success
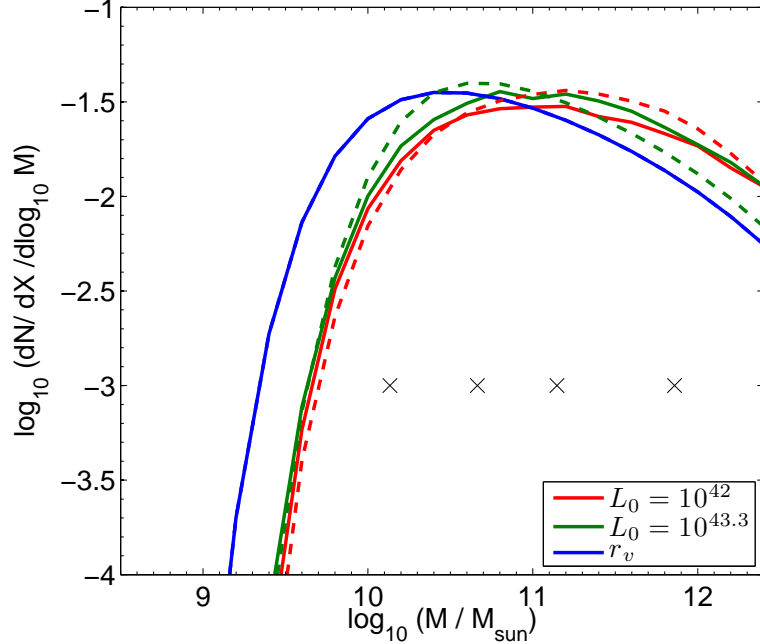
Figure 5.12: The contribution of different mass ranges to the incidence rate of DLAs/emitters ($\mathrm{d}^2\mathcal{N}/\mathrm{d}X/\mathrm{d}\log_{10} M$). The same models are shown as in Figure 5.10. The majority of DLAs/emitters have masses in the range $10^{10} - 10^{12} M_\odot$. We refer to Chapter 4 for a comparison of our prediction of $\mathrm{d}^2\mathcal{N}/\mathrm{d}X/\mathrm{d}\log_{10} M$ to that of numerical simulations. The black crosses indicate the masses of the four galaxies we will study in Chapter 6.

of Pontzen et al. (2008) in reproducing the observed metallicity distribution is additional evidence in favour of this mass range, as are the observed spatial correlation of DLAs and LBGs (Cooke et al. 2006).

5.3.4   Limitations of our Modelling

Our modelling has a number of limitations and (over-) simplifications that we will discuss in this section. Firstly, we have assumed spherical symmetry throughout. Deviations from a spherical configuration will most likely make escape easier for Lyα photons in certain directions. However, dense clumps in the outer regions of haloes may significantly increase the observed spatial extent of faint Lyα emitters. Similarly, our simple velocity field is certainly an oversimplification. More

complex velocity fields may bring photons passing through gas in the outer regions of the halo back toward line centre. This would increase the spatial extent of the emitter.

We have also ignored radiative transfer outside the virial radius of the halo. This effectively assumes not only that scattering in the outer parts of DM haloes is negligible, but also that the same is true for scattering by the neutral hydrogen in the IGM. Whether these assumptions are reasonable will depend both on the poorly constrained distribution of neutral hydrogen in the outer parts of low-mass DM haloes and on the bulk motion of the scattering gas relative to the IGM (see e.g. Santos 2004).

We have furthermore not modelled the effect of ionising radiation, either from external or internal sources, except by reducing the amount of neutral hydrogen within the virial radius of the DM haloes below its cosmic value, ostensibly due to the effects of the UV background. More sophisticated modelling should take into account the self-shielding of the gas against the meta-galactic UV background self-consistently. We have checked here that the radius at which the gas is able to maintain neutrality by self-shielding is $\gtrsim r_{\mathrm{emission}}$, the size of the emission region at the flux level of the Rauch et al. emitters as defined in Section 5.3.3. The meta-galactic UV background should thus have little effect on the size of the Lyα emission region predicted by our modelling. Note, however, that this will no longer be the case at fainter flux levels as the neutral hydrogen density/column density will drop sharply outside the region able to self-shield.

Internal sources of ionising radiation such as stars will reduce the neutral fraction of the gas, and in an inhomogeneous manner. Neither stars nor the UV background is expected to significantly ionise the bulk of the neutral gas in the protogalaxies studied here — these are the sites of DLAs after all. Spatially extended star formation is likely to increase the production of Lyα at large radii, possibly increasing the observed size of the emitters.

Finally, we have also ignored the effects of dust. This assumption is not unreasonable as DLAs are known to have a rather small dust content (Wolfe et al. 2005). The recent modelling of Lyα radiative transfer by Laursen et al. (2009b) including dust also suggests that for the majority of DLAs, with their rather low metallicity and low mass host haloes, the effect of dust is not important. Any dust present is most likely to make the surface brightness profile more centrally

peaked, as photons that emerge from the emitter at an angle have a longer path length through the dust. Note also that the effect of dust is known to depend sensitively on the clumpiness of the neutral gas (Hansen & Oh 2006).

5.4 Conclusions

We have used a Monte-Carlo radiative transfer code to model the spatial and frequency distribution of the Lyα emission due to star formation in (proto-)galaxies at the centre of DM haloes with masses of $10^{9.5}$ to $10^{12} M_{\odot}$. We have investigated a range of assumptions for the spatial distribution and the dynamical state of neutral hydrogen. DM haloes in this mass range had been previously identified as the likely hosts of DLAs and the recently detected population of faint spatially extended Lyα emitters. Our main results are the following:

- As previously found by other authors, when the dynamics of neutral hydrogen in galaxies is dominated by infall/outflow, the spectral shape of the Lyα emission from star formation is characterized by a strong blue/red peak, occasionally accompanied by a weaker red/blue peak. The spectral shape is very sensitive to the spatial distribution, velocity structure, and (to a lesser extent) the temperature structure of the gas. The larger central column densities in the more massive galaxies/haloes make escape of the Lyα photons more difficult. The photons must then scatter further in frequency and space and thus emerge with a larger frequency shift and the emission extends to larger radii. Larger bulk motions lead to more energy per scattering being transferred between the photons and the gas. This results in a larger frequency shift of the dominant spectral peak and a larger contrast between the strong and weak spectral peak.

- The surface brightness profiles for photons emitted at the centre of the haloes show a central peak with wings extending as far as our assumed neutral hydrogen distribution as long as the column density of neutral hydrogen exceeds $\sim 10^{16}$ cm^{-2}. The spatial profile of the emission is likewise sensitive to the spatial distribution, velocity, and temperature structure of the gas. The spatial distribution is significantly more centrally peaked when the amplitude of the bulk motions increases toward the centre of the halo.

- Expanding shells of neutral hydrogen, similar to those invoked to explain the Lyα emission from LBGs, produce spectra with one or more prominent red peaks. The surface brightness profiles are very flat, remaining essentially constant for 75% of the radius of the shell. This appears at odds with the observed profiles of the R08 emitters, almost all of which show a central peak.

- Our modelling simultaneously reproduces the column density distribution of the neutral hydrogen and the velocity width distribution of low-ionisation metals associated with DLAs, as well as the size distribution and the luminosity function of the Rauch et al. emitters if we assume: i) that absorbers and emitters are hosted by DM haloes that retain about 20% of the cosmic baryon fraction in the form of neutral hydrogen, with a spatial distribution that follows an NFW-like profile with concentration parameter ~ 7 times larger than that of the dark matter, ii) that absorbers and emitters are hosted by DM haloes with virial velocities $\gtrsim 50$ km s^{-1}, iii) that the central Lyα emission due to star formation has a duty cycle of $\sim 25\%$ and the luminosity is proportional to the mass of neutral hydrogen in the DM haloes, and iv) that the bulk velocity of the gas at the centre of the halo is modest, which facilitates the scattering of photons to large radii.

- The DM haloes that contribute most to the incidence rate of DLAs have masses in the range $10^{9.5}$ - $10^{12} M_\odot$ and virial velocities in the range of 35 to 230 km s^{-1}. The lower cut-off is mainly determined by the rather sharp decrease in the velocity width distribution of low-ions associated with DLAs for $v_\mathrm{w} \lesssim 30$ km s^{-1}, but may also be reflected in the turnover of the Lyα luminosity function at the faintest fluxes. The DM host halo masses are significantly smaller than those inferred for L_* LBGs, which is consistent with the much higher space density of the faint emitters.

The success of our detailed Lyα radiative transfer modelling in explaining the observed properties of both DLAs and the faint Rauch et al emitters with a consistent set of assumptions further strengthens the claim that the faint emitters are indeed the long sought host galaxies of DLA/LLs. Together with our modelling, the observed properties of the faint emitters should thus provide robust estimates

of the space density, Lyα luminosity, halo mass, the duty cycle of star formation and the gas kinematics of the host galaxies of DLAs. The current ultra-deep spectroscopic surveys in the HUDF and HDF should soon provide important additional information on the stellar content and possibly also dust content of these objects. This will allow us to further test the nature of what are almost certainly the building blocks of typical present-day galaxies like our own.

6

3D Lyα Radiative Transfer in Galaxy Formation Simulations in a Cosmological Context

The previous chapter discussed the limitations of the model considered thus far. We have used analytical methods that have been successful in modelling the average properties of typical cosmic structures. However, Lyα radiative transfer is sensitive to the finer details of the distribution and velocity of neutral hydrogen — inhomogeneity can provide channels for rapid spatial diffusion, while bulk velocities can have a similar effect in frequency space.

The complicated physics of galaxy formation — gravity, hydrodynamics, radiative cooling, star formation, supernovae, galactic winds, ionising radiation, dust and metal production — has led to numerical simulations becoming the method of choice for investigating the formation of structure in the baryonic Universe. These simulations provide us with realistic 3D density and velocity fields that take into account most of the relevant physics, at least phenomenologically.

In this chapter, we will apply the Lyα radiative transfer code developed in

previous chapters, extended for use in a 3D grid in Section 3.3, to the results of a galaxy formation simulation in a cosmological context.

6.1 The Cosmological Simulations of Tescari et al.

We will make use of the cosmological hydrodynamic simulations of Tescari et al. (2009). These simulations were aimed at reproducing the physical properties of the host galaxies of DLAs at $z \sim 3$. The numerical code is based on GADGET-2, which is a parallel Tree-PM SPH code (Springel 2005). In addition to gravity and hydrodynamics, the other physical processes that are modelled in the simulation are:

- Radiative cooling and heating, including a UVB produced by quasars and galaxies.

- Chemical evolution, tracing the following elements: H, He, C, O, Mg, S, Si and Fe. The contribution of metals is included in the cooling function. The release of metals from Type Ia and Type II supernovae, as well as low- and intermediate-mass stars, is followed.

- Star formation, using a multiphase criterion. Three distinct stellar Initial Mass Functions (IMFs) are considered.

- Galactic winds, using two different prescriptions. An energy-driven wind model is implemented in the form of a velocity kick given to a chosen particle, with a mass-loss rate proportional to the star formation rate. Tescari et al. (2009) also consider a momentum-driven wind model that mimics a scenario in which the radiation pressure of a starburst drives an outflow. In this model, the velocity kick scales with the velocity dispersion of the galaxy. These wind prescriptions are admittedly rather crude, and rely on phenomenological parameters that are poorly constrained either by observations or by more sophisticated modelling. This reflects the significant uncertainty regarding the influence of winds on galaxy formation.

Halo ID	Mass $(M_\odot)$	Mass H I $(M_\odot)$	Virial Velocity (km s^{-1})	Virial Radius (kpc)	Virial Radius (arcsec)	Lyα Luminosity ($\times 10^{40}$ erg s^{-1})
1	7.24×10^{11}	1.25×10^{10}	203	76	9.64	520
2	1.40×10^{11}	1.07×10^{9}	117	43.9	5.58	44.4
3	4.61×10^{10}	2.66×10^{8}	80.9	30.3	3.85	11.1
4	1.36×10^{10}	1.30×10^{8}	53.8	20.2	2.56	5.43

Table 6.1: The properties of the four chosen haloes.

The simulations were run with varying box size and numerical resolution. The fiducial "SW" (Strong Wind) simulation (which we will use in the sections that follow) has a box size of $10h^{-1}$ Mpc and 320^3 particles, with a mass resolution of $3.5 \times 10^5 h^{-1} M_\odot$. This simulation employed a strong (600 km s^{-1}), energy-driven wind and a Salpeter stellar IMF.

The halo mass function in the simulation is fit well by the Sheth-Tormen mass function. The observed incidence rate of DLAs is matched by the simulations, assuming that haloes below $10^9 h^{-1} M_\odot$ do not host DLAs. The observed column density distribution is also reproduced successfully, while the total neutral gas mass in DLAs (Ω_{DLA}) is underpredicted by a factor of about 2 in the SW simulation. The high velocity tail of the velocity width distribution of low-ions associated with DLAs, however, is significantly underpredicted. The simulations do not produce enough absorption systems with velocity width greater than 100 km s^{-1}.

From the simulation, four haloes at $z = 3$ were selected for further study. These haloes show a rich variety of density and velocity structures. The properties of these haloes (neutral hydrogen density, temperature and bulk velocity) were projected onto a 64^3 cube, centred on the centre of mass of the halo. Each cube has a comoving size of $200h^{-1}$ kpc, so each cell is $3.125h^{-1}$ comov.kpc across.

6.2 Results

Table 6.1 lists the properties of each halo. The Lyα luminosity is calculated using Equation (5.8) from the previous chapter, using $L_0 = 10^{42}$ erg s^{-1}. This value of L_0 was chosen to match the luminosity function of the Rauch et al. emitters for
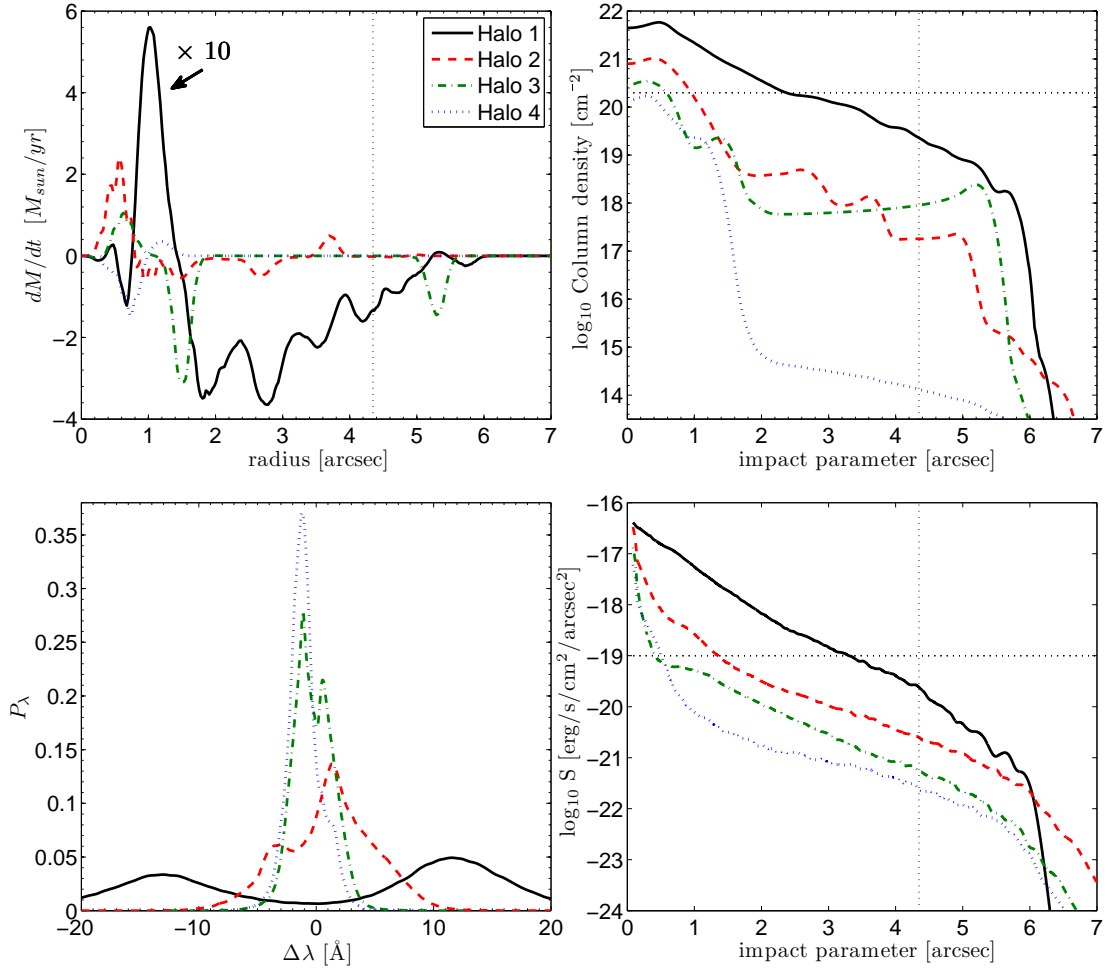
Figure 6.1: The angularly-averaged properties of each of the four haloes, as shown in the legend. The dotted vertical lines at ~ 4.5 arcsec indicate half of the size of the box. Beyond this radius, part of the sphere over which we are averaging is outside the simulation box, which lowers the average. The upper left panel shows $\mathrm{d}M/\mathrm{d}t$, which is the rate at which mass is flowing through a surface of constant radius r. Note that the curve for Halo 1 has been divided by ten. The upper right panel shows the average column density for a sightline passing at a given impact parameter from the centre of the halo. The thin dotted horizontal line indicates the minimum column density of a DLA, $N_{\mathrm{DLA}} = 10^{20.3}$ cm^{-2}. The lower left panel shows the (observed) angularly-averaged spectrum, with the area under each curve normalised to unity. The lower right panel shows the surface brightness profile. The luminosity that normalises each curve is given in the last column of Table 6.1. The thin dotted horizontal line represents the 1σ surface brightness limit of the Rauch et al. survey, $S_0 = 10^{-19}$ erg/s/cm^2/arcsec^2.

the $\alpha = 1$ model. The masses and luminosities of our four haloes are illustrated in the context of the models of the Rauch et al. emitters in the last chapter in Figures 5.11 and 5.12. The masses of the four haloes probe the peak of the predicted incidence rate of DLAs / emitters per unit log mass $(\mathrm{d}^2\mathcal{N}/\mathrm{d}X/\mathrm{d}\log_{10} M)$. The chosen luminosities are typical of those observed in the survey of Rauch et al.

Figure 6.1 summarises the angularly-averaged results for each of the four haloes, as shown in the legend. The dotted vertical lines at ~ 4.5 arcsec indicate half of the size of the box. Beyond this radius, part of the sphere over which we are averaging is outside the simulation box, which lowers the average.

The upper left panel of Figure 6.1 shows $\mathrm{d}M/\mathrm{d}t$, which is the rate at which neutral hydrogen in the haloes flows through a surface of constant radius r. Positive (negative) values correspond to outflow (inflow). Note that the curve for Halo 1 has been reduced by a factor of ten for ease of comparison within the chosen plot range. The upper right panel shows the average column density for a sightline passing at a given impact parameter from the centre of the halo. The thin dotted horizontal line indicates the minimum column density of a DLA, $N_{\mathrm{DLA}} = 10^{20.3}$ cm^{-2}. The lower left panel shows the (observed) angularly-averaged spectrum, with each curve normalised to unity. The lower right panel shows the surface brightness profile. The luminosity that normalises each curve is chosen to be the same as in the $\alpha = 1$ model of Chapter 5, which matches the observed luminosity of the Rauch et al. emitters. The values are given in the last column of Table 6.1. The thin dotted horizontal line represents the 1σ surface brightness limit of the Rauch et al. survey, $S_0 = 10^{-19}$ erg/s/cm^2/arcsec^2.

The mass flow shows a mixture of inflow and outflow, with inflow often dominating in the outer parts of the halo. The mass flow rate at the centre of all haloes is quite modest. The spectra show a variety of double-peaked profiles, with one of the peaks dominating. The width and separation of the peaks increases with the mass of H$\textsc{i}$ in the halo. As we will discuss in more detail when we consider each halo individually in the next section, there is a correlation between the dominance of inflow (outflow) in $\mathrm{d}M/\mathrm{d}t$ and the domination of the blue (red) peak in the spectrum.

As expected, the column density peaks near the centre of the halo. The "steps" in the column density profiles of Haloes 2 and 3 show the influence of separate clumps of H$\textsc{i}$ at large radii. The surface brightness profiles also peak at the centre

of the halo, and generally follow the decline of the column density whilst being much smoother. The more massive haloes are more spatially extended, while the smaller haloes display a more pronounced central peak. The size of the emitter, as measured to the surface brightness limit of the Rauch et al., is generally larger than the cross-section for damped absorption.

We will now discuss each of the haloes in turn.

Halo 1

Angularly-Averaged Properties

Halo 1 is the most massive of the haloes, with a mass of $7.24 \times 10^{11} M_\odot$. Its angularly-averaged properties are shown in Figure 6.2. The top left panel shows the average number density of H<small>I</small> atoms as a function of radius. The decrease in the number density at small radii is the result of the centre of mass of the neutral hydrogen being offset from the centre of mass of the halo. Beyond the peak at $r \approx 0.6$ arcsec, the number density drops approximately as r^{-3}, which is similar to the large-radius behaviour of the NFW-like profile used in the last chapter. The average cosmic number density of hydrogen at $z \approx 3$ is 1.2×10^{-5} cm^{-3}, while the volume-averaged neutral fraction of hydrogen in the IGM is $\lesssim 10^{-5}$.

The thick black line in the top right panel shows the average column density for a sightline passing at a given impact parameter from the centre of the halo. The thin dotted horizontal line indicates the minimum column density of a DLA. The column density is a decreasing function of radius, with sightlines containing DLAs probing the centre of the halo. The DLA cross-section has a radius of ~ 2.4 arcsec, which is approximately a quarter of the virial radius. The thin coloured lines show the column density as a function of impact parameter for lines of sight parallel to the x-, y- and z-axis. They show that there is only modest variation in the column density (when averaged over radius) with orientation.

The next panel (row 2, column 1) shows the H<small>I</small> density weighted radial velocity profile,

$$v_r(r) \equiv \langle \boldsymbol{v}_{\rm b} \cdot \hat{\boldsymbol{r}} \rangle \equiv \frac{\int_0^{2\pi} \int_0^{\pi} \left(\boldsymbol{v}_{\rm b} \cdot \hat{\boldsymbol{r}} \right) \rho_{\rm HI}(r, \theta, \phi) \sin \theta \, \mathrm{d}\theta \, \mathrm{d}\phi}{\int_0^{2\pi} \int_0^{\pi} \rho_{\rm HI}(r, \theta, \phi) \sin \theta \, \mathrm{d}\theta \, \mathrm{d}\phi}. \tag{6.1}$$

The plot shows a mixture of inflow (v_r negative) and outflow, with inflow dominating particularly in the outer regions. The typical velocities of inflow are 100
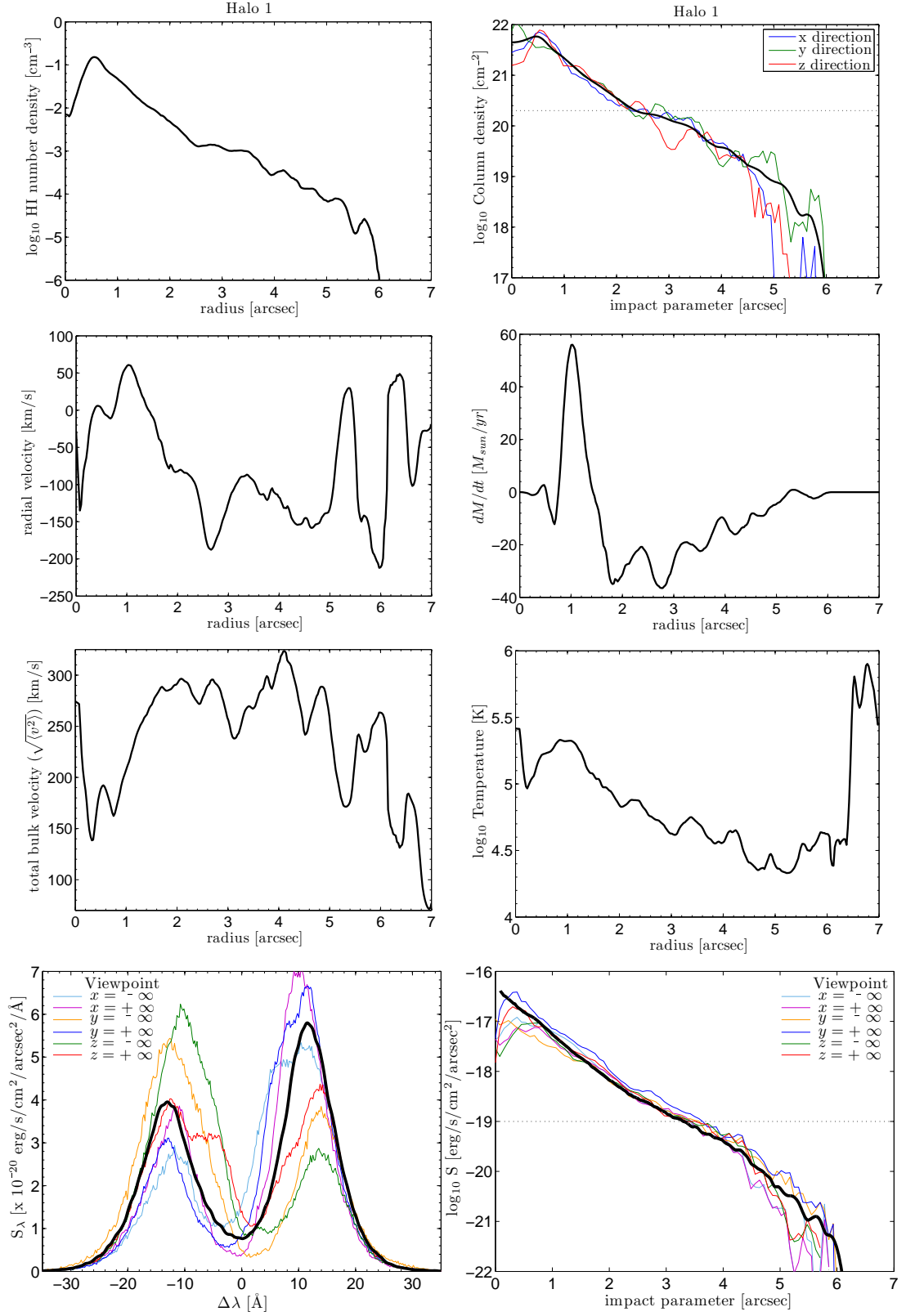
Figure 6.2: Angularly-averaged properties of Halo 1. Mass $= 7.24 \times 10^{11} M_\odot$, Mass HI $= 1.25 \times 10^{10} M_\odot$, $R_v = 76$ kpc $= 9.64$ arcsec, $v_c = 203$ km s^{-1}, $L_{\text{Ly}\alpha} = 5.20 \times 10^{42}$ erg s^{-1}.

- 200 km s^{-1}, with the largest velocities being comparable to the virial velocity. There is a general trend toward lower velocities in the centre of the halo. The velocity profile is, however, far from smooth.

The panel to the right shows $\mathrm{d}M/\mathrm{d}t$, which is related to the radial velocity as $\mathrm{d}M/\mathrm{d}t = 4\pi r^2 v_r(r)\rho_{\mathrm{HI}}^{\mathrm{av}}(r)$, where $\rho_{\mathrm{HI}}^{\mathrm{av}}$ is the average neutral hydrogen density at radius r. It shows that the outflow at $r \approx 1$ arcsec, while of relatively modest velocity, carries with it a significant amount of mass. The outer regions of the halo are dominated by inflow at rates of $20 - 40 M_{\odot}/\mathrm{yr}$.

The next panel shows the HI density weighted total bulk velocity $v = \sqrt{\langle |\boldsymbol{v}_{\mathrm{b}}|^2 \rangle}$. The velocity ranges from 150 - 320 km s^{-1}, with modest velocities at the centre of the halo. The total bulk velocity of the gas is typically larger than its radial component by a factor of 2-3. Hence, there are significant non-radial motions in the gas.

The temperature of the neutral gas is shown in the next panel, weighted by the neutral hydrogen density: $T_r = \langle T \rangle$. It shows that most of the neutral gas is in the temperature range $10^{4.5} - 10^{5.5}$ K, with the gas in the outer regions becoming slightly cooler until a jump at $r \approx 6.4$ arcsec. This hotter gas has been shock-heated, either as it falls into the halo or possibly as the result of an outflow. Note that if we perform a volume average of the temperature, then the result is an order of magnitude larger. This shows that the coolest gas is also the most dense, which is the result of the radiative cooling rate being proportional to ρ^2. The halo contains cool, dense clouds embedded in a hot, diffuse medium.

The bottom left panel shows the angularly-averaged spectrum, where we have averaged over a sphere whose maximum radius is half of the diagonal of the box. The thick black curve shows the spectrum as a function of the observed wavelength offset ($\Delta\lambda = (1+z)\,\Delta\lambda_{\mathrm{emitted}}$). The spectrum shows a classic double-peaked profile, peaking at $|\Delta\lambda| \approx 12 - 13$ Å, which corresponds to a velocity offset of 750 - 800 km s^{-1}. The spectrum does not drop to zero in between the peaks, indicating that bulk velocities allow some line-centre photons to escape. The red peak is slightly larger than the blue peak, indicating the influence of the outflow at $r \approx 1$ arcsec. The thin coloured lines show the emergent spectra along the six different lines of sight. The position of the observer is labelled in the legend. The curves are calculated by an average over the 2D spectra (e.g. Figure 6.3) and normalised to the *same value* as the angularly-averaged curve. These lines show

the variation in the observed spectrum with viewing angle. An observer sees only one of these lines — the angularly-averaged spectrum is obviously not observable — and will thus see a spectrum dominated by either the red or the blue peak, depending on the orientation.

The thick black curve in the bottom right panel shows the angularly-averaged surface brightness profile. The luminosity that normalises each curve is given in the last column of Table 6.1. The thin dotted horizontal line represents the 1σ surface brightness limit of the Rauch et al. survey, $S_0 = 10^{-19}$ erg/s/cm^2/arcsec^2. The surface brightness profile peaks at the centre, and decreases smoothly until $r \approx 5$ arcsec, at which point it decreases more rapidly as the column density drops off. The radius corresponding to the Rauch et al. surface brightness cut-off is 3.3 arcsec, which is approximately 1.4 times larger than the radius at which the column density drops below the threshold for a DLA. The thin coloured lines show the surface brightness profile as viewed from the six different lines of sight. The peak surface brightness varies with viewing angle by up to an order of magnitude.

2D Images and Spectra

Figure 6.3 shows a 2D view of the halo, looking along the x-axis from $-\infty$ (left) and $+\infty$ (right). Note that some of the axes have been flipped so that the left and right columns have their axes pointing in the same direction.

The top panels show the column density along a line of sight parallel to the x-axis. Each panel corresponds to a line of sight that passes through the nearer half of the box. In other words, the colours in the legend to the right of each figure represent the column density of neutral hydrogen that the photon (emitted at the centre of the halo) must pass through in order to reach the observer. The solid line in the top two panels is a contour representing $N_{\mathrm{DLA}} = 10^{20.3}$ cm^{-2}, calculated for sightlines passing through the *entire* box; it is thus the same in the left and right top panels. A sightline passing through the region inside the contour would encounter a DLA.

The next two panels are an image of the halo that is coloured according to the surface brightness of Lyα, calculated[1] assuming the luminosity as described previously and given in Table 6.1. The solid contour represents the surface brightness

---

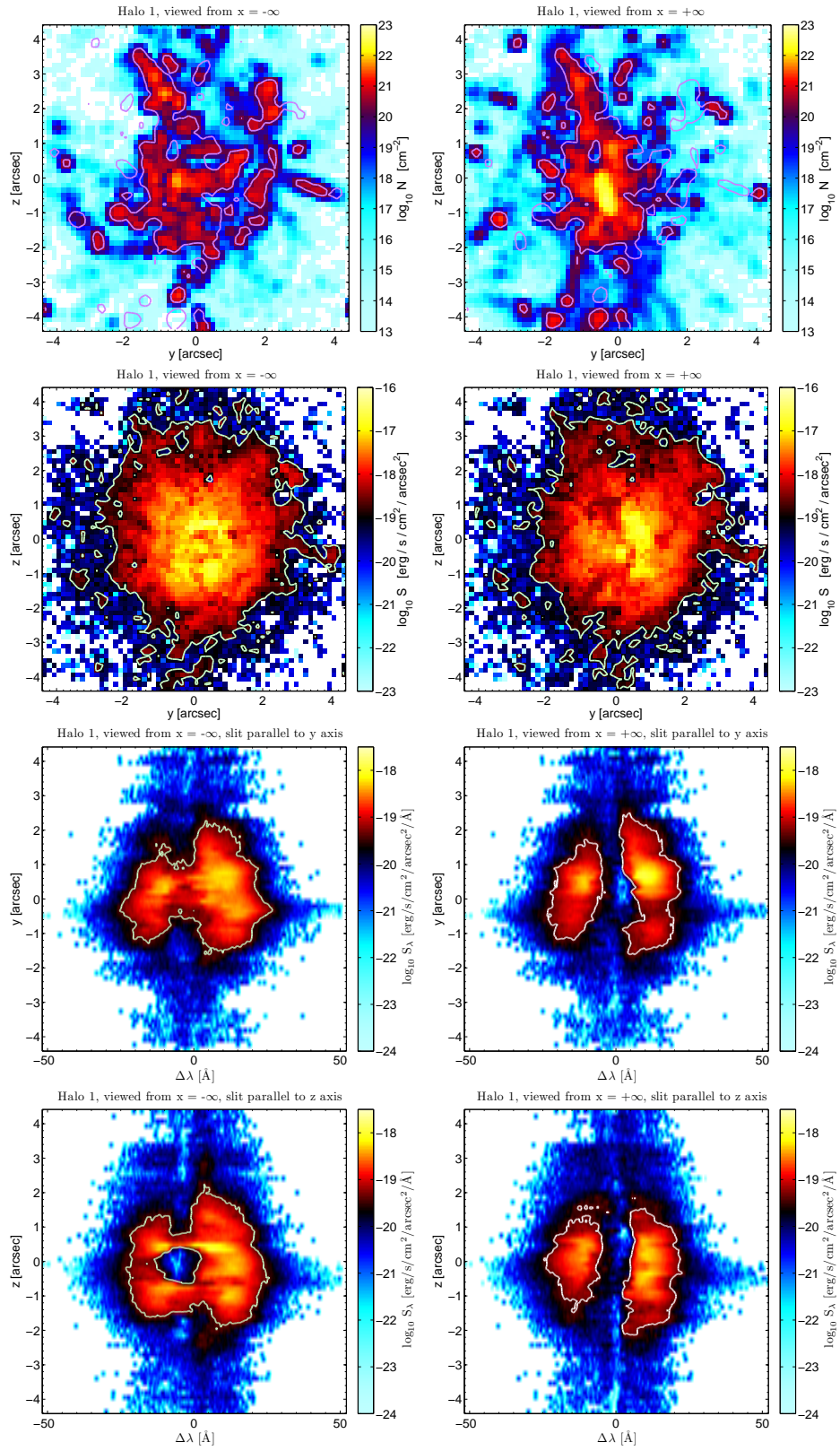[1]See equation (20) of Laursen et al. (2009a).

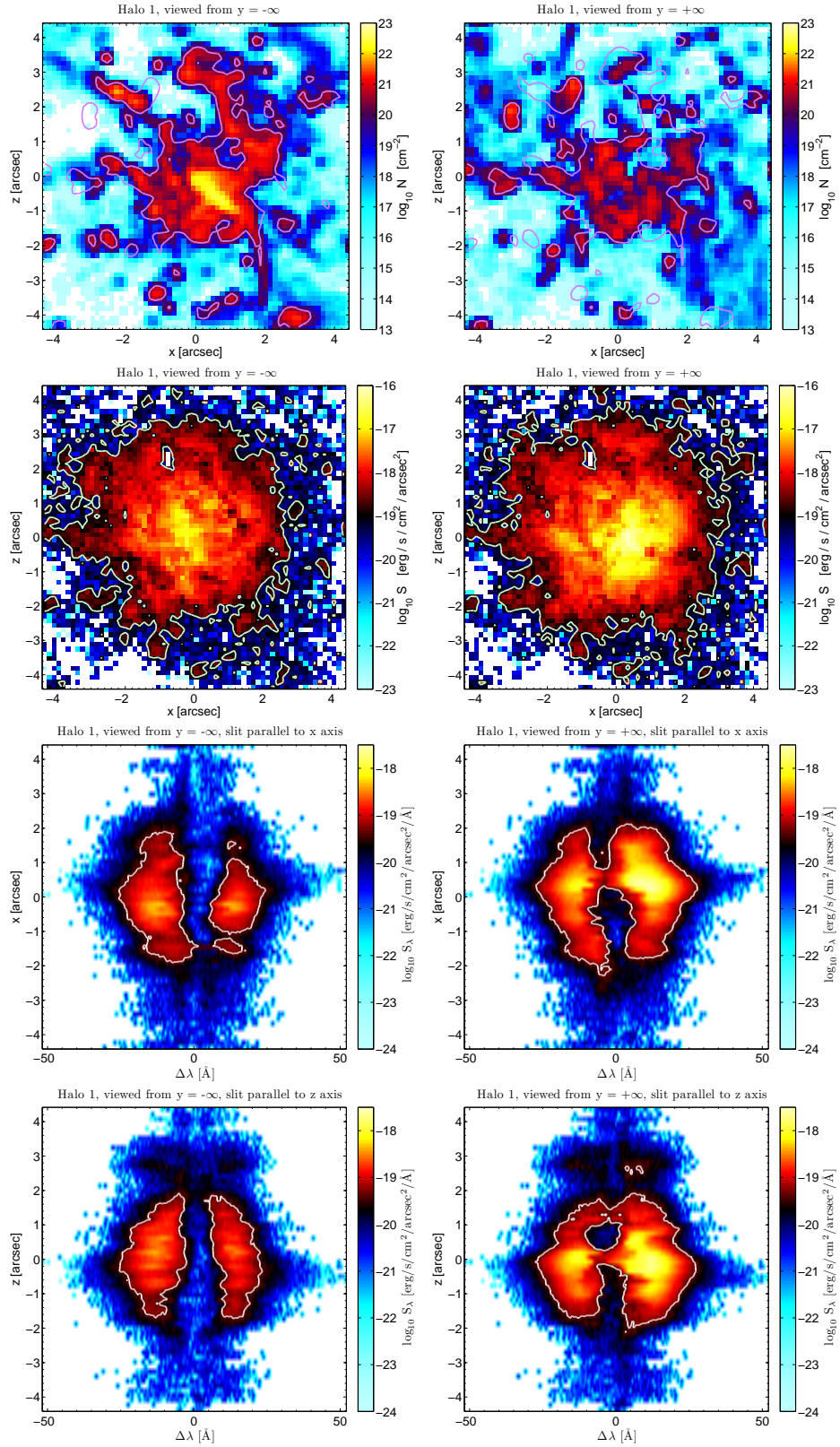Figure 6.3: 2D images and spectra for Halo 1, x-direction

117

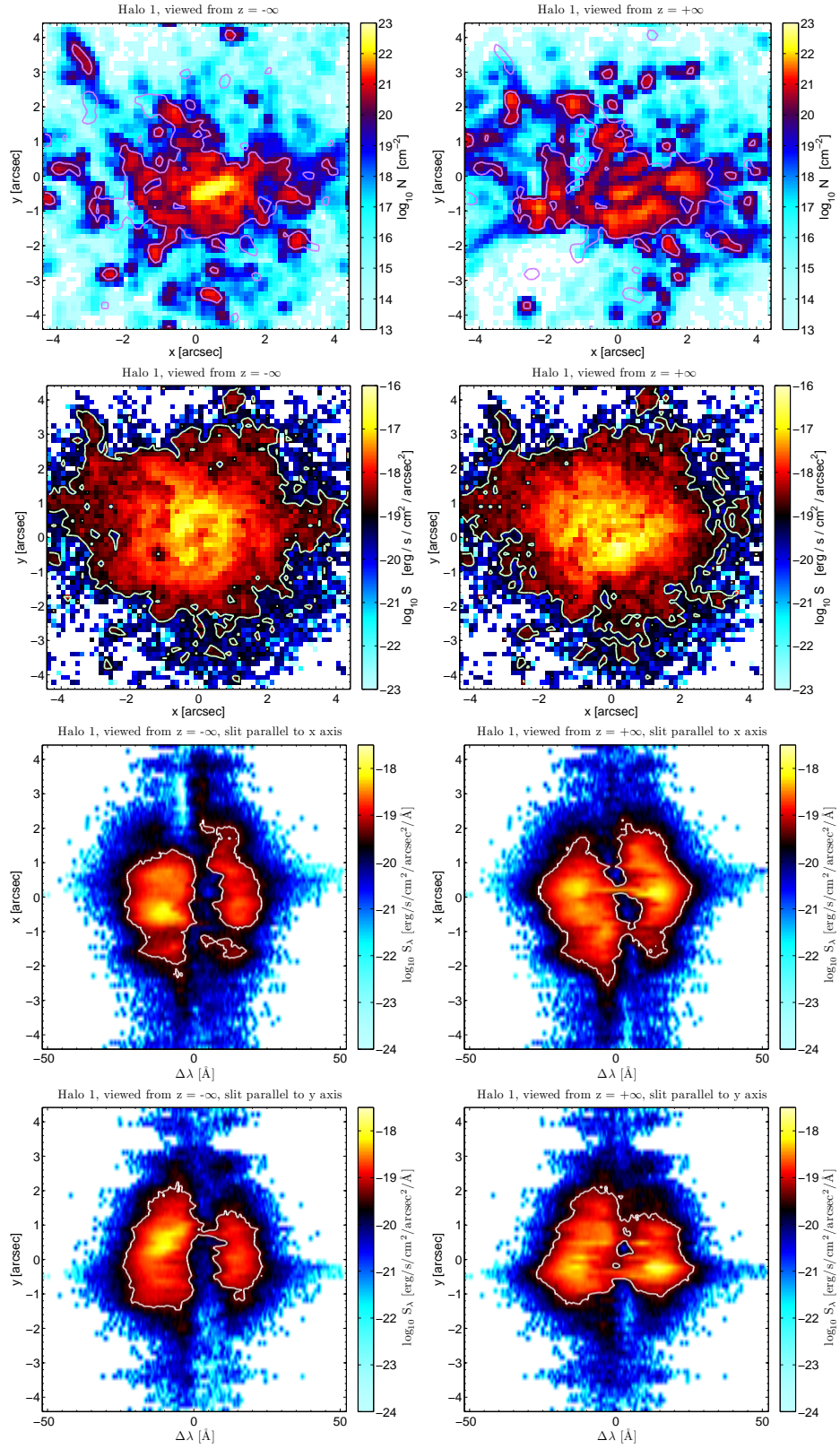Figure 6.4: 2D images and spectra for Halo 1, y-direction

Figure 6.5: 2D images and spectra for Halo 1, *z*-direction

limit of the Rauch et al. survey, $S_0 = 10^{-19}$ erg/s/cm^2/arcsec^2.

The bottom four panels are 2D spectra, calculated using a "slit" placed along either the y- or z-direction (labelled in the title to each panel) and with a width of 2 arcsec, which is the same width as in Rauch et al. (2008). The contour shows the spectral intensity limit of the Rauch et al. survey (Rauch, M., private communication), which is $S_\lambda \approx 4 \times 10^{-20}$ erg/s/cm^2/arcsec^2/Å.

Figures 6.4 and 6.5 show the corresponding images and spectra for observers looking along the y- and z-directions.

The column density images show that the gas is clumpy and irregular. The spatial distribution of neutral hydrogen shows a mix of more spherical features and some outlying filaments. The column density of individual clumps of neutral hydrogen drops rapidly below $\sim 10^{17}$ cm^{-2}. The differences between pairs of panels in each figure show the asymmetry in the distribution of gas. In particular, there is a rather dense cloud at $(x, y, z) \approx (0.4, -0.2, -0.5)$ arcsec that accounts for the angularly-averaged number density peaking at $r \approx 0.6$ arcsec in Figure 6.2.

The surface brightness images show that the Lyα emission generally traces but is much less clumpy than the underlying neutral hydrogen distribution. In particular, the S_0 contour encloses a larger area than the DLA contour both by being slightly larger but also by having fewer "holes". The Lyα photons are scattered effectively out to large radii, until the column density drops below $\sim 10^{17}$ cm^{-2}. Our central Lyα source is able to illuminate clouds of neutral gas that are detached from the central clump, such as in the top left corner of the panels in Figure 6.3.

The images further show that Lyα photons are able to find low-density paths of escape. This is most clearly seen in Figure 6.4. The top panels show that the photons face a much smaller column density in the positive y-direction than in the negative, and the surface brightness images correspondingly show that the halo looks significantly brighter when viewed from the positive direction.

The spectra generally show the classic double-peaked profile, most often with a slightly brighter red peak. Note, however, that the spectrum as viewed from $z = +\infty$ shows a more prominent blue peak. As expected, the separation of the peaks is largest where the column density is largest. The two peaks often merge into one central peak as the density of the gas drops in the outer parts of the
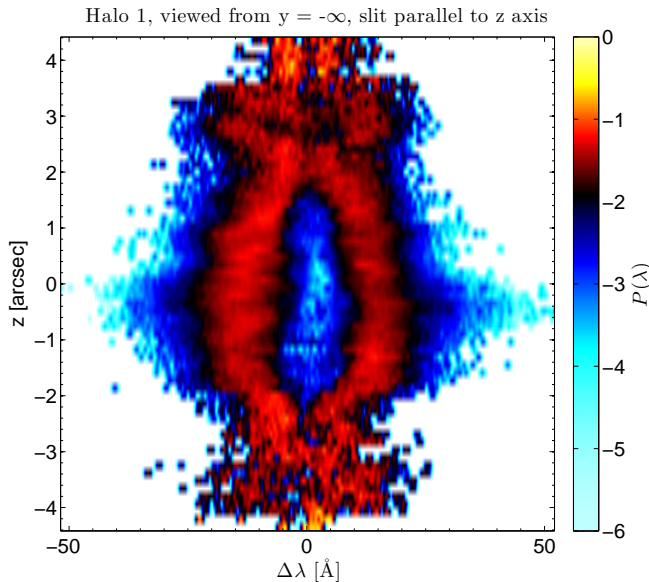
Figure 6.6: The same spectrum as the bottom left plot of Figure 6.4, except that each row of the spectra has been normalised to unity.

halo. This is clearly seen in Figure 6.6, which shows the same spectrum as the bottom left plot of Figure 6.4, except that each row of the spectrum has been normalised to unity. The spectrum is remarkably symmetric about $\Delta\lambda = 0$, with peaks that are furthest apart in the centre of the figure, and merge as the column density drops. Note that at the top of the figure ($z \approx 3$ arcsec) the two peaks reappear, due to a corresponding increase in the column density seen at the top of the top left panel in 6.4.

Halo 2

Angularly-Averaged Properties

Halo 2 is an order of magnitude less massive than Halo 1, meaning that the virial velocity is smaller by a factor of two. The properties of Halo 2 are similar to the brightest emitters in the Rauch et al. survey, and its mass coincides with the peak of our preferred model for $d^2\mathcal{N}/dX/d\log_{10} M$ (red dashed line) in Figure 5.12. The angularly-averaged properties of Halo 2 are shown in Figure 6.7, similarly to Figure 6.2. The dashed vertical line indicates the virial radius of the halo. The number density is much less smooth than in Halo 1, due to the presence of several clumps of HI. The column density profile again shows that the DLA sightlines pass near the centre of the halo. Outlying clumps, as seen in the number density

distribution, cause "steps" in the column density distribution, which contribute to the LLS cross-section.

The radial velocity profile, as before, shows a mixture of inflow and outflow, with somewhat lower typical velocities of 50 km s^{-1}. The outflow in the densest, central regions of the halo occurs at rates of $\sim 2M_\odot/\text{yr}$, which is more than an order of magnitude less than in Halo 1. The total velocity of the gas is again larger than the radial velocity by a factor of 2-3, with velocities ranging from 80 to 180 km s^{-1}. The temperature shows little variation, ranging between $10^{4.2}$ to $10^{4.8}$ K.

The angularly-averaged spectrum (thick black curve) is dominated by a red peak at $\Delta\lambda = 1.4$ Å (86 km s^{-1}), accompanied by a smaller blue bump. This is indicative of the dominance of outflow over inflow in the kinematics of the gas. The coloured lines show the range of observed spectra, which differ remarkably from the angularly-averaged spectrum and each other. The surface brightness profile shows a central peak with a tail that flattens out as the column density does the same. The radius corresponding to the Rauch et al. surface brightness cut-off is 1.35 arcsec, which is again approximately 1.4 times larger than the radius at which the column density drops below the threshold for a DLA.

2D Images and Spectra

Figures 6.8, 6.9 and 6.10 show 2D perspectives on Halo 2, in the same way as for Halo 1. The dashed black line shows the virial radius. The column density shows the irregular distribution of gas, with a mixture of thin filaments and relatively isolated clumps of neutral hydrogen. The cross-section for damped absorption is composed of a number of isolated clumps, scattered around the innermost parts of the halo.

The surface brightness images again show that the Lyα emission generally traces the neutral hydrogen whilst smoothing out its clumpy substructure. The size of the emission region is again both larger than the DLA cross-section and more connected. Figure 6.10 shows the central Lyα source illuminating a filament running along the bottom of the image.

The spectra viewed along the x-direction (Figure 6.8) show a red peak in one direction and a blue peak in the other. The largest, central concentration of H$\textsc{i}$ is slightly offset from the centre in the x-direction, so that the column density in

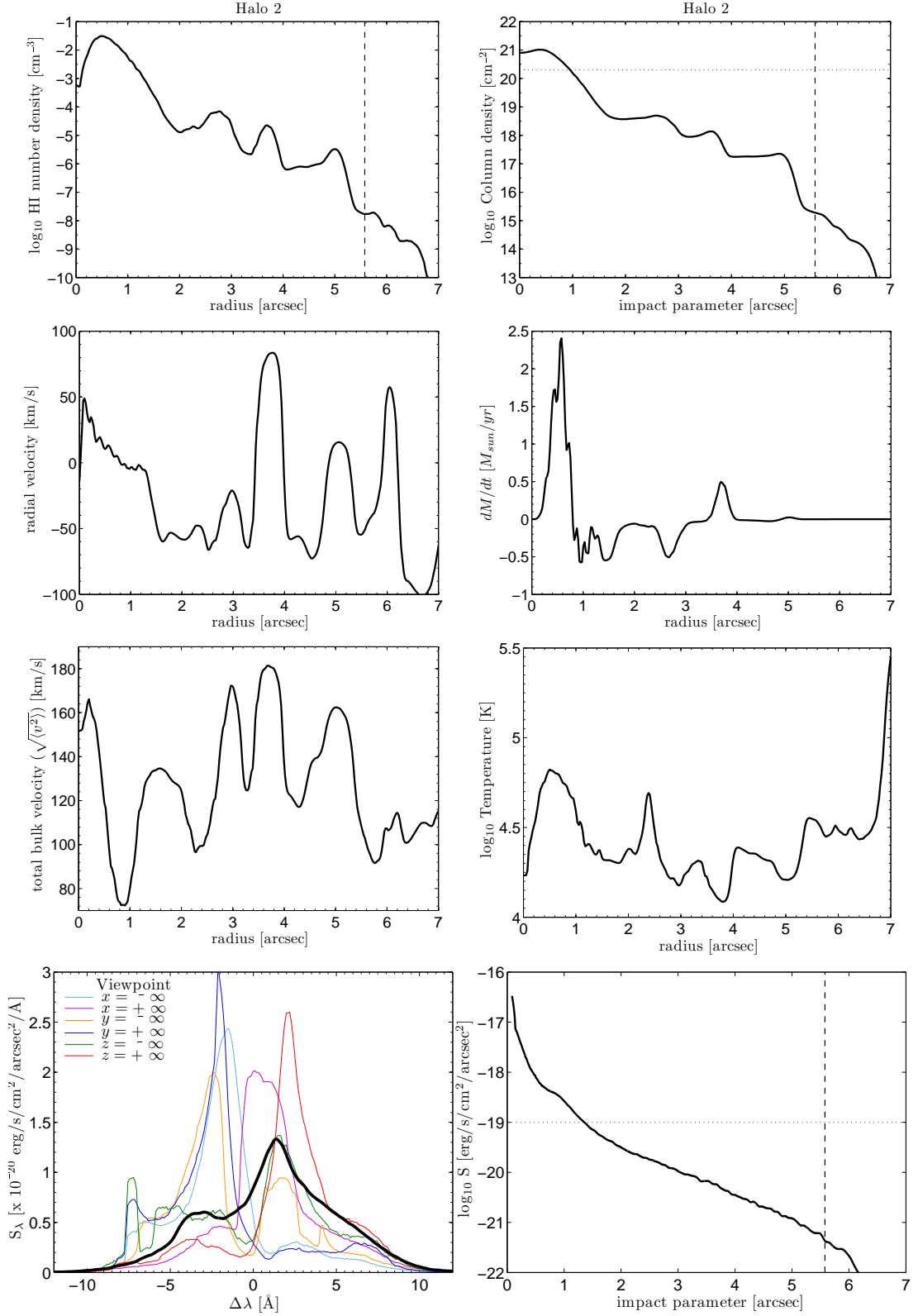Figure 6.7: Angularly-averaged properties of Halo 2. Mass $= 1.4 \times 10^{11} M_\odot$, Mass HI $= 1.07 \times 10^9 M_\odot$, $R_v = 44$ kpc $= 5.58$ arcsec, $v_c = 117$ km s^{-1}, $L_{\text{Ly}\alpha} = 4.44 \times 10^{41}$ erg s^{-1}.
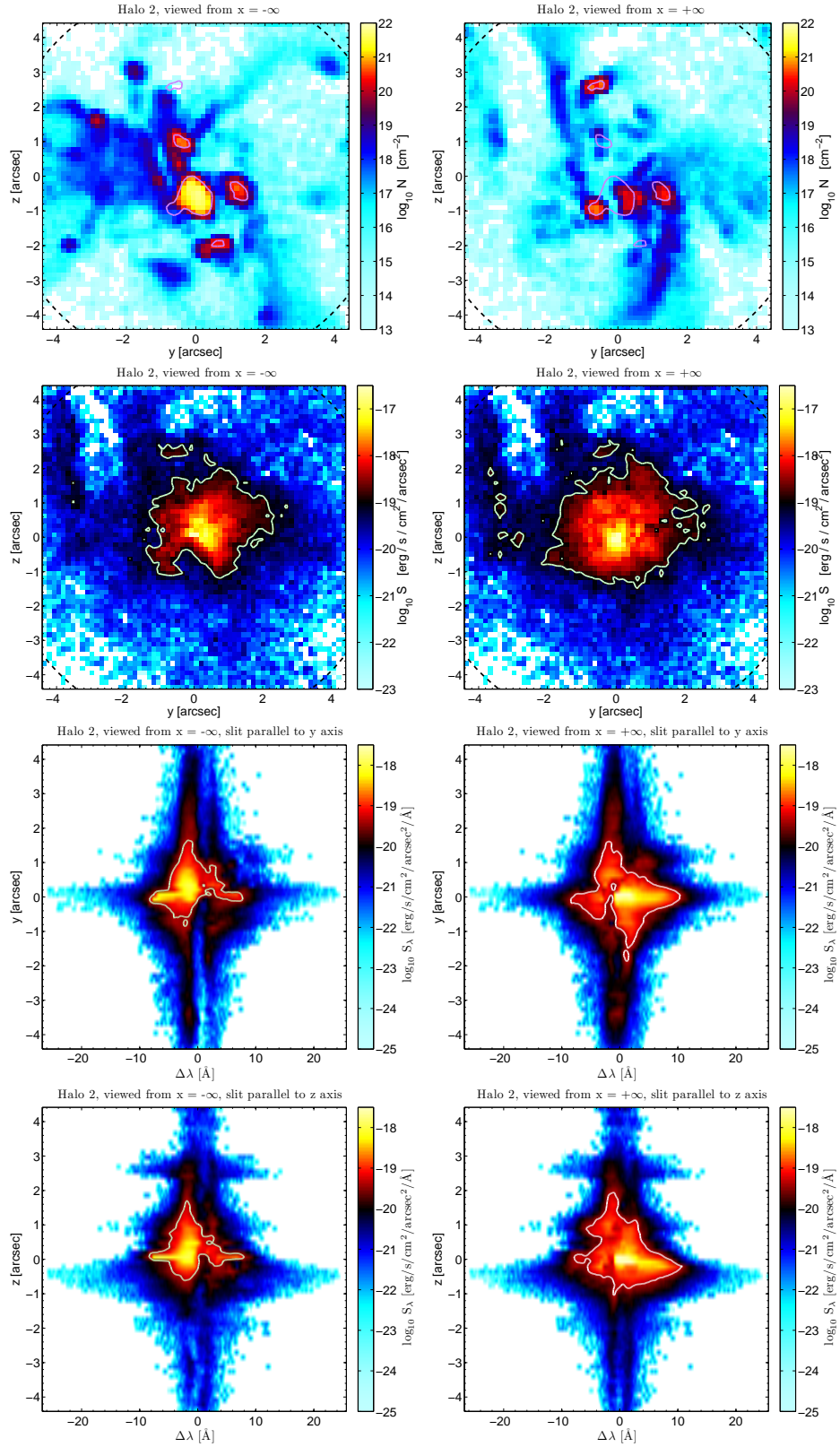
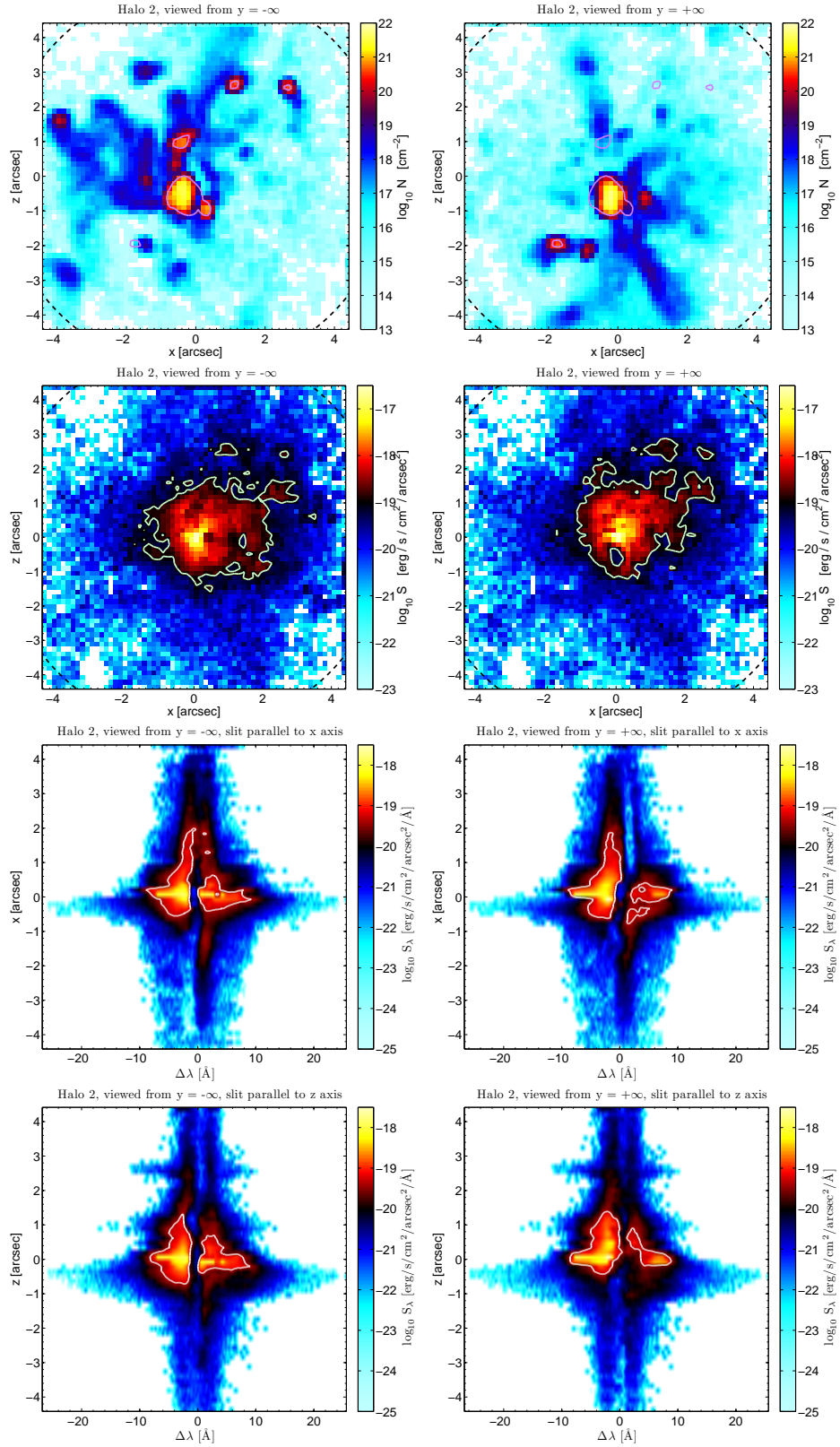Figure 6.8: 2D images and spectra for Halo 2, *x*-direction

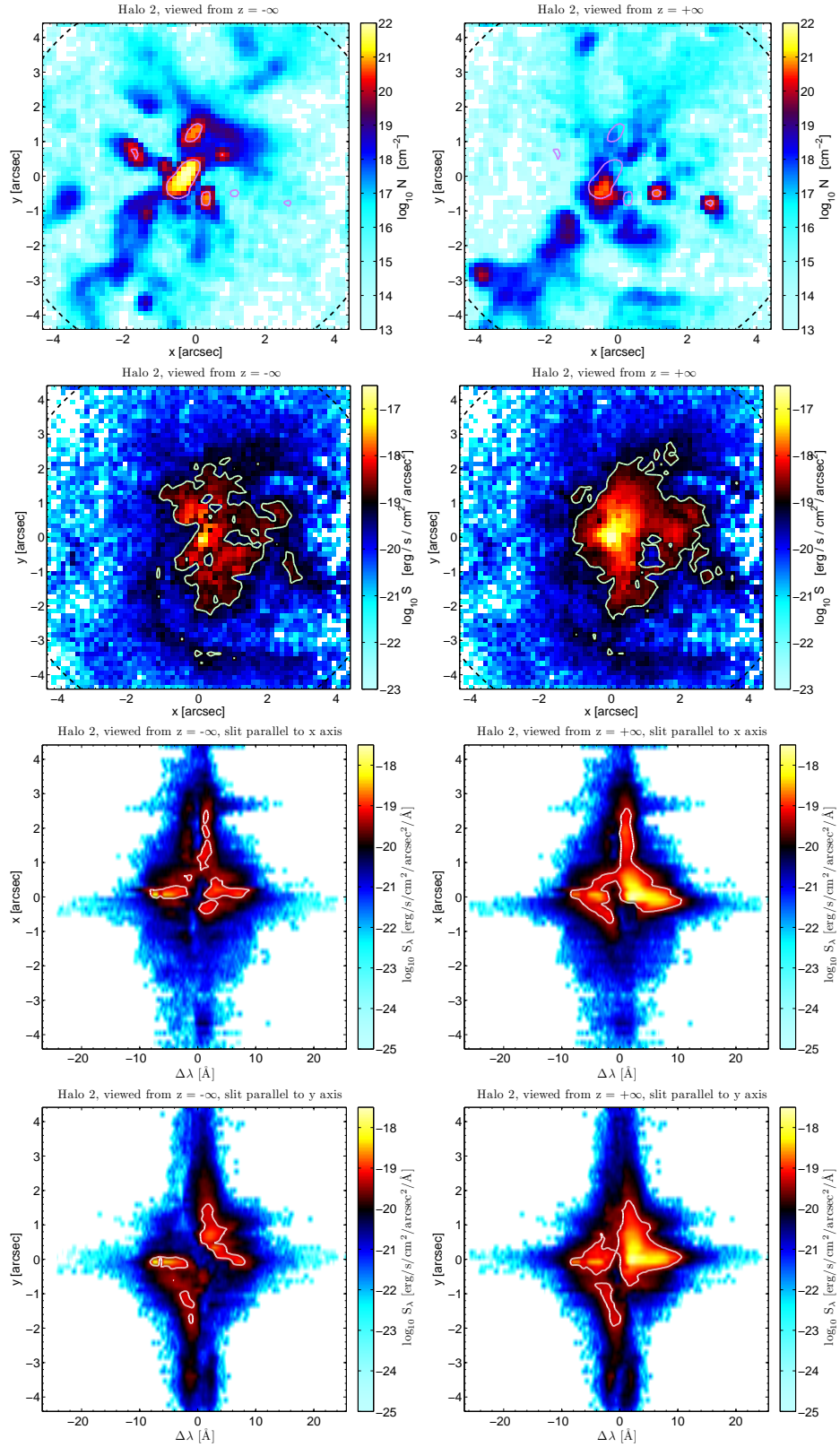Figure 6.9: 2D images and spectra for Halo 2, y-direction

Figure 6.10: 2D images and spectra for Halo 2, *z*-direction

126

the negative x-direction is significantly larger than in the positive direction. From the plot of $\mathrm{d}M/\mathrm{d}t$, we know that the gas in this small protogalaxy is outflowing with a moderate velocity. Thus, photons emitted in the positive x-direction are reflected off a receding HI cloud and are thus on average redshifted, while photons that are emitted toward $x = -\infty$ have been scattered into the rest frame of gas that is approaching the observer, resulting in a net blueshift.

The bottom left panel of Figure 6.10 shows a shift from a single blue peak to a double-peaked profile to a red peak as y increases. Such a profile is often interpreted as a rotating velocity field, viewed edge-on. However, in gas with such high optical depth, the relationship between bulk velocity and spectral shape can be more complicated. Here, the spectral shape is indeed not indicative of an ordered rotation field, at least not on the implied scale. This has been verified directly, and is confirmed by the fact that the "rotation" spectral shape is not seen from any other viewpoint.

Most of the other spectra are qualitatively similar to the angularly-averaged profile.

Halo 3

Angularly-Averaged Properties

The angularly-averaged properties of Halo 3 are shown in Figure 6.11; the layout is the same as in Figure 6.2. Halo 3 contains discrete clouds embedded in a low-density medium, which is evident in the peaks in the HI density accompanied by low density tail. There is a clump at $r = 5.3$ arcsec. This clump affects the angularly-averaged column density at smaller radii, which accounts for the plateau at $N_{\mathrm{HI}} \sim 10^{18}$ cm^{-2}. If we discount this outer clump, the column density falls rapidly to 10^{16} cm^{-2} beyond $r \approx 2$ arcsec.

The radial velocity profile is dominated by an infalling clump at $r \approx 1.6$ arcsec with a velocity of 130 km s^{-1}. The outer regions of the halo are also infalling at a velocity similar to the virial velocity. The mass flow shows a central dense clump with a moderate outflow velocity and two infalling outer clumps. The temperature of the neutral gas again remains relatively constant, with a noticeable drop as the density increases.

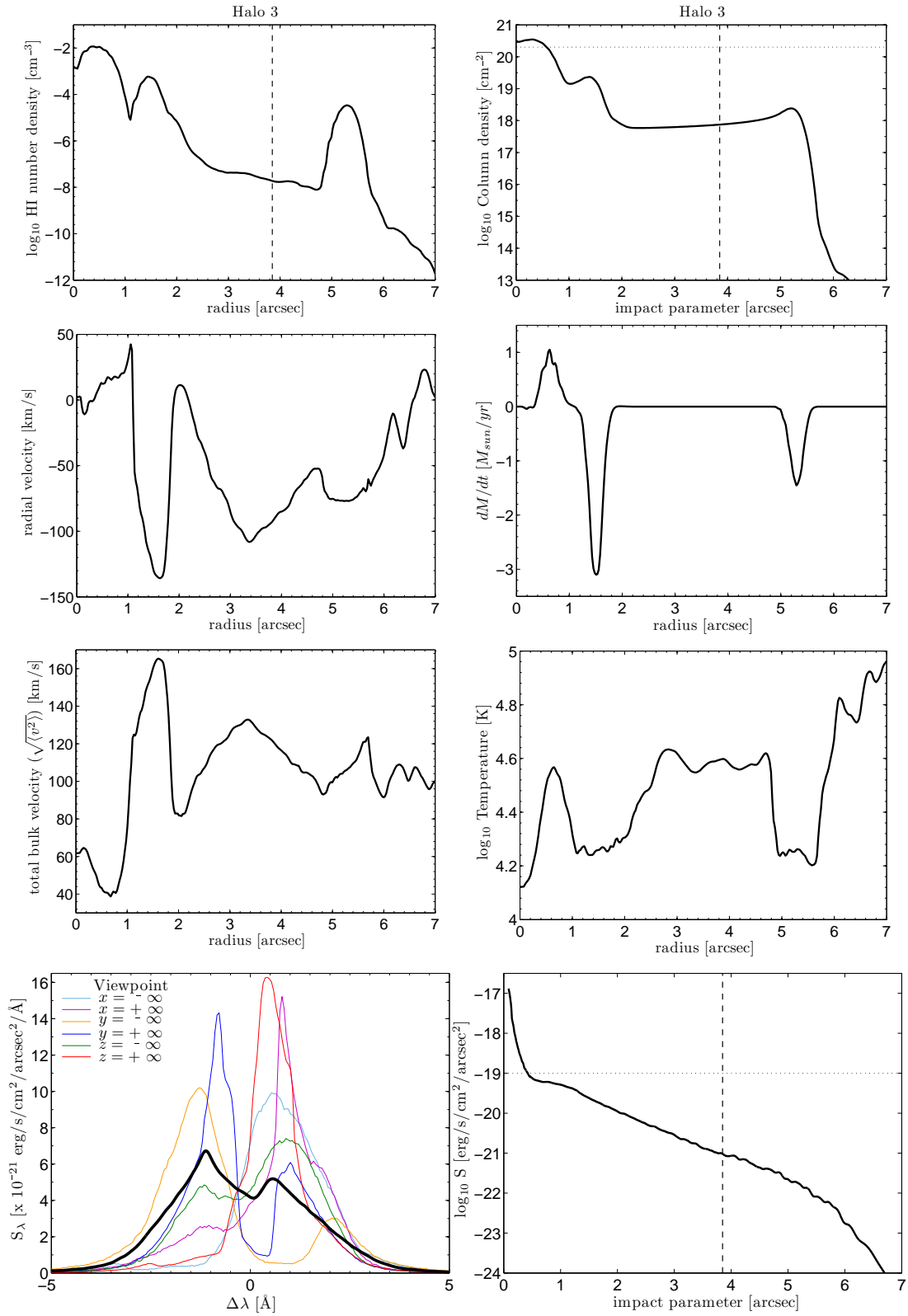The spectrum shows two peaks, with a dominant blue peak that can be at-

Figure 6.11: Angularly-averaged properties of Halo 3. Mass $= 4.61 \times 10^{10} M_\odot$, Mass H I $= 2.66 \times 10^8 M_\odot$, $R_v = 30.3$ kpc $= 3.85$ arcsec, $v_c = 80.9$ km s^{-1}, $L_{\text{Ly}\alpha} = 1.11 \times 10^{41}$ erg s^{-1}.

tributed to the presence of inflowing gas. The spectrum does not drop to zero between the peaks, showing that line-centre photons are able to escape. The surface brightness profile shows a central peak giving way to a more gentle decrease in the outer regions.

2D Images and Spectra

Figures 6.12, 6.13 and 6.14 show 2D perspectives on Halo 3, in the same way as for the other haloes. The column density is dominated by four dense clumps scattered inside the virial radius, and one clump outside. We see a familiar trend emerging — the Lyα photons are scattered to column densities of $\sim 10^{17}$ cm^{-2}, resulting in an emission region that is larger and smoother than the cross-section for damped absorption. Figure 6.14 shows an example of the emission region lighting up the neutral gas, and also being obscured (in the $z = +\infty$ image) by an outlying clump of gas at $y \approx -1$ arcsec. Our central source is able to illuminate detached clumps of gas. For example, the region at $x \approx -2$ arcsec in the $y = -\infty$ surface brightness image of Figure 6.13 contains no source of Lyα photons.

The 2D spectra show a variety of line shapes. The spectra of Figure 6.12 are dominated by a red peak, while those of Figure 6.13 are stronger on the blue side, reflecting the different velocities of the different clumps of neutral hydrogen. The central regions produce a double-peaked profile in Figure 6.14, indicating a moderate central velocity.

Halo 4

Angularly-Averaged Properties

The angularly-averaged properties of Halo 4 are shown in Figure 6.15; the layout is the same as in Figure 6.2. The halo shows a dense core (with $N_{\mathrm{HI}} > 10^{19}$ cm^{-2}) surrounded by a very low density background with a column density in the range 10^{14} - 10^{15} cm^{-2}. At the centre, there is a substantial inflow with a maximum infall velocity of 80 km s^{-1}, accompanied by a more moderate outflow at 20-30 km s^{-1}. The temperature again lies between $10^{4.2}$ and 10^5 K, with the denser gas being the coolest.
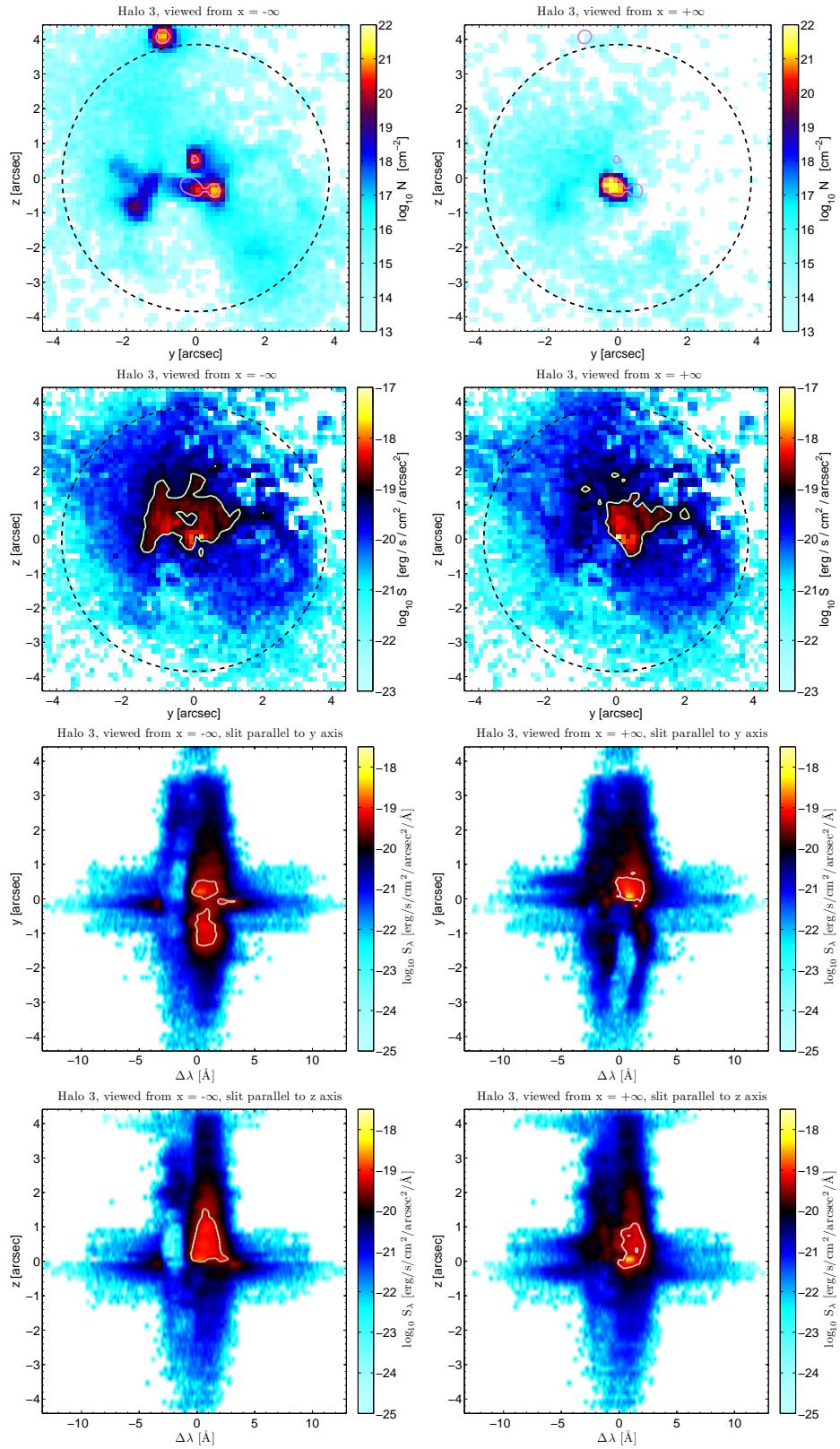
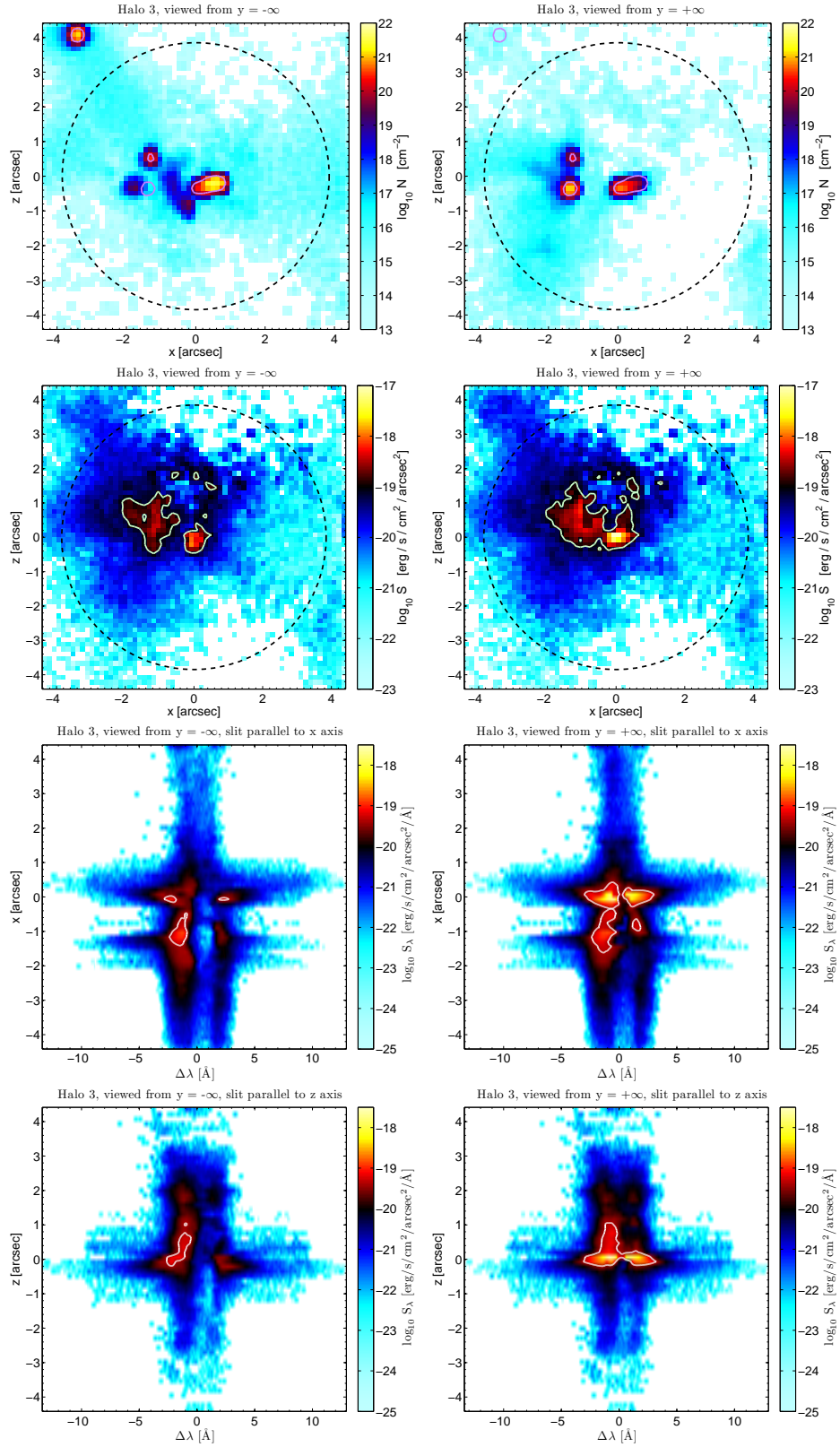Figure 6.12: 2D images and spectra for Halo 3, x-direction

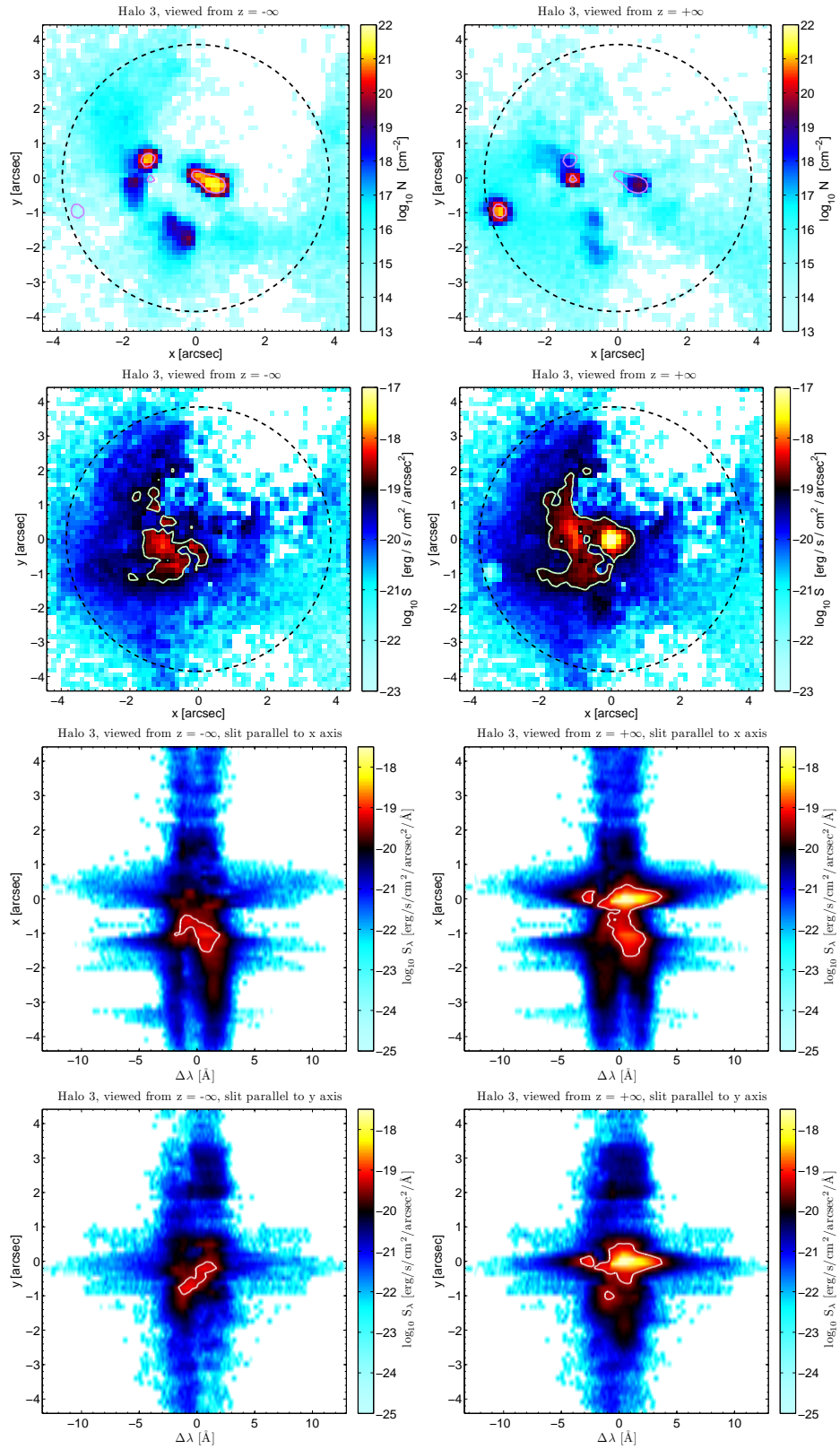Figure 6.13: 2D images and spectra for Halo 3, y-direction

131

Figure 6.14: 2D images and spectra for Halo 3, z-direction

The angularly-averaged spectrum is a particularly nice illustration of inflowing gas producing a more prominent blue peak in the spectrum. In spite of this, there are still viewpoints from which the spectrum is dominated by a red peak. The surface density profile reflects the column density profile — the inner, dense core results in a central peak whose rapid decline gives way to a shallower plateau as we reach the outer, diffuse background.

2D Images and Spectra

Figures 6.16, 6.17 and 6.18 show 2D perspectives on Halo 4, in the same way as for Halo 1. The image of the Lyα emission shows that scattering has effectively smoothed out the clumps in the neutral hydrogen distribution. Our central source lights up the rather low column density gas in the outer regions of the halo to surface brightness levels of $\sim 10^{-20}$ - 10^{-21} erg/s/cm^2/arcsec^2.

The 2D spectra are again rather diverse. Figure 6.16 shows double-peaked profiles with both red and blue prominent peaks, while the Figure 6.17 shows more symmetric peaks, with the view from $y = -\infty$ being considerably dimmed by intervening gas. The placement of the clumps with respect to the source and observer has a considerable effect on the visibility of the line. Figure 6.18 shows a prominent blue peak due to the infalling gas.

6.3 Discussion

We will now summarise our findings from the previous section.

- The haloes contain a mixture of inflowing and outflowing gas. As a result, the angularly-averaged spectrum typically shows two peaks, with the relative strength of the red (blue) peak being a reflection of the relative contribution of outflow (inflow) in the mass flow rate. The mass flow rate is more relevant than the radial velocity profile to the relative effect of inflow/outflow on the spectral shape. Line-centre photons can escape due to inhomogeneities in the gas density (e.g. Figure 6.14) providing low-density paths of escape and bulk velocities allowing rapid diffusion in the fluid frame frequency space.
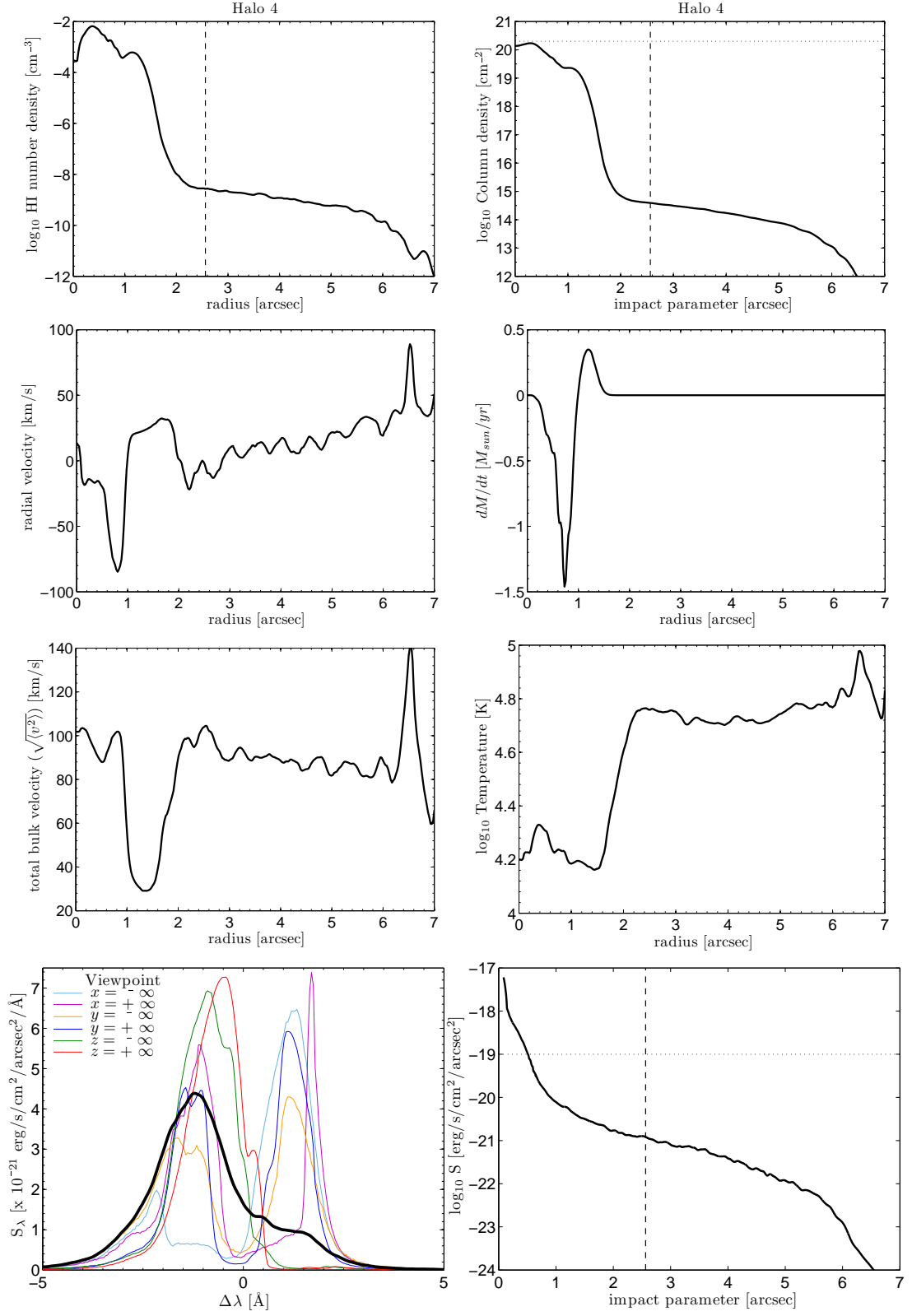
Figure 6.15: Angularly-averaged properties of Halo 4. Mass $= 1.36 \times 10^{10} M_\odot$, Mass HI $= 1.30 \times 10^8 M_\odot$, $R_v = 20.2$ kpc $= 2.56$ arcsec, $v_c = 53.8$ km s^{-1}, $L_{\mathrm{Ly}\alpha} = 5.43 \times 10^{40}$ erg s^{-1}.
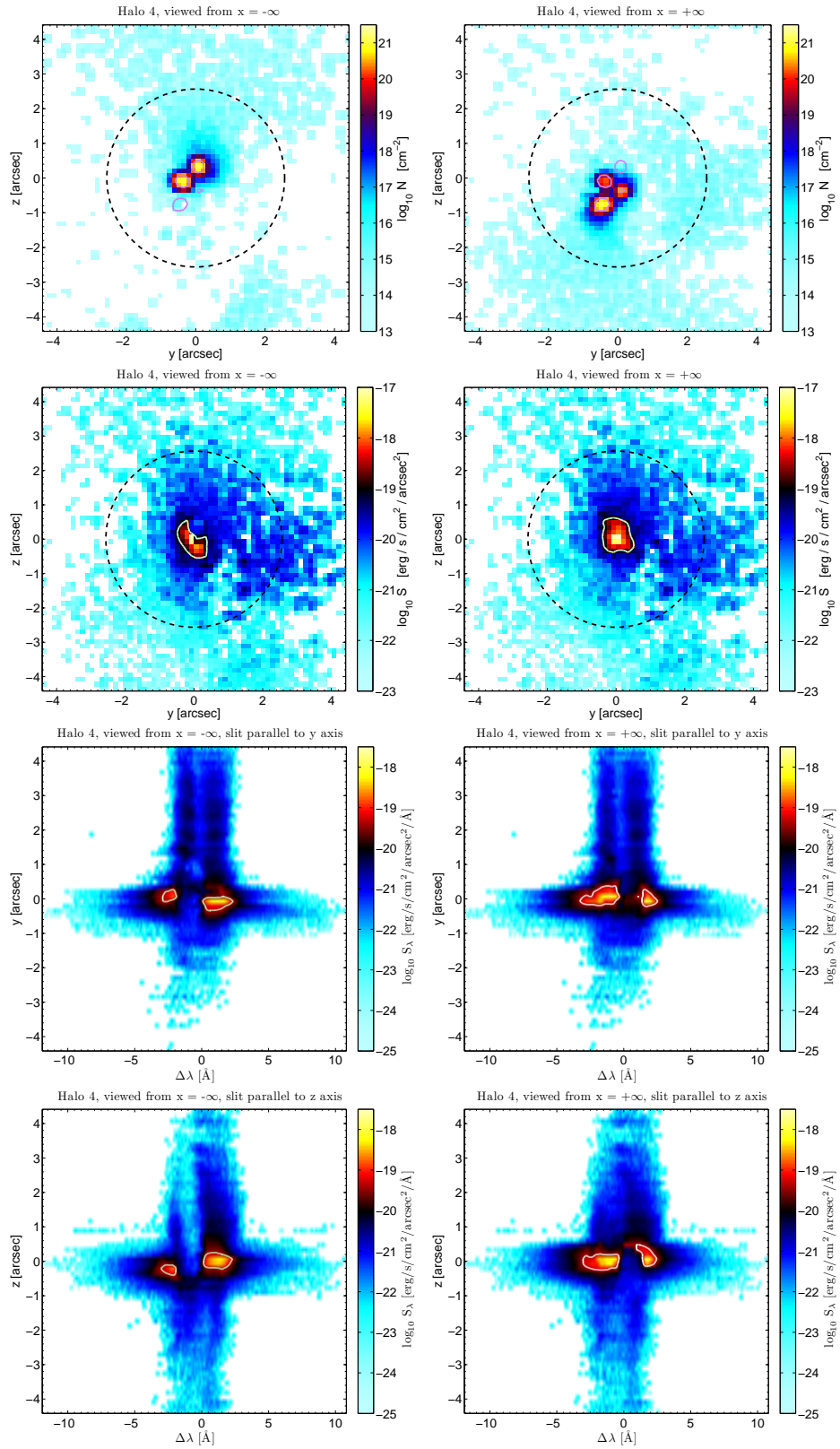
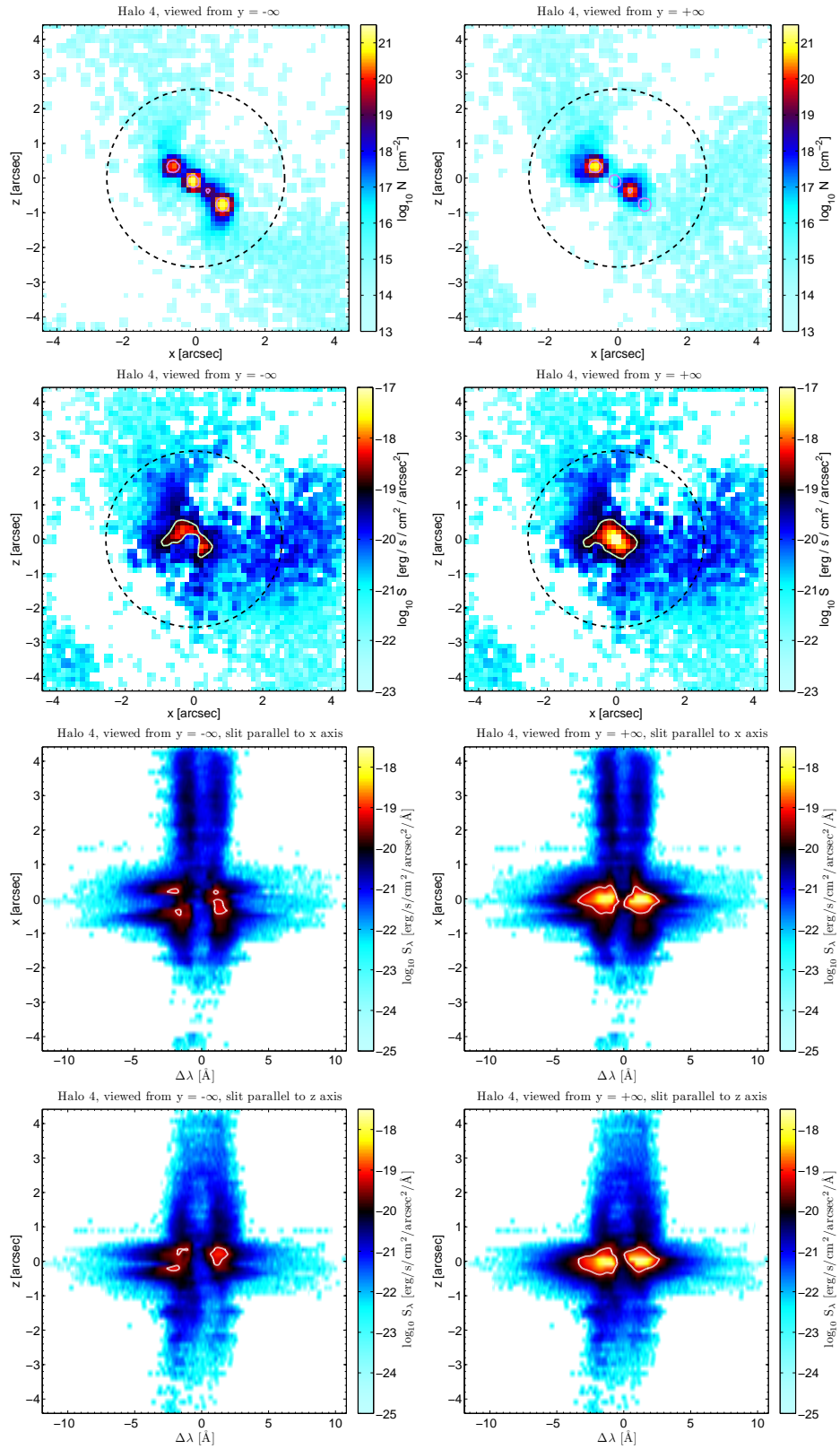Figure 6.16: 2D images and spectra for Halo 4, x-direction

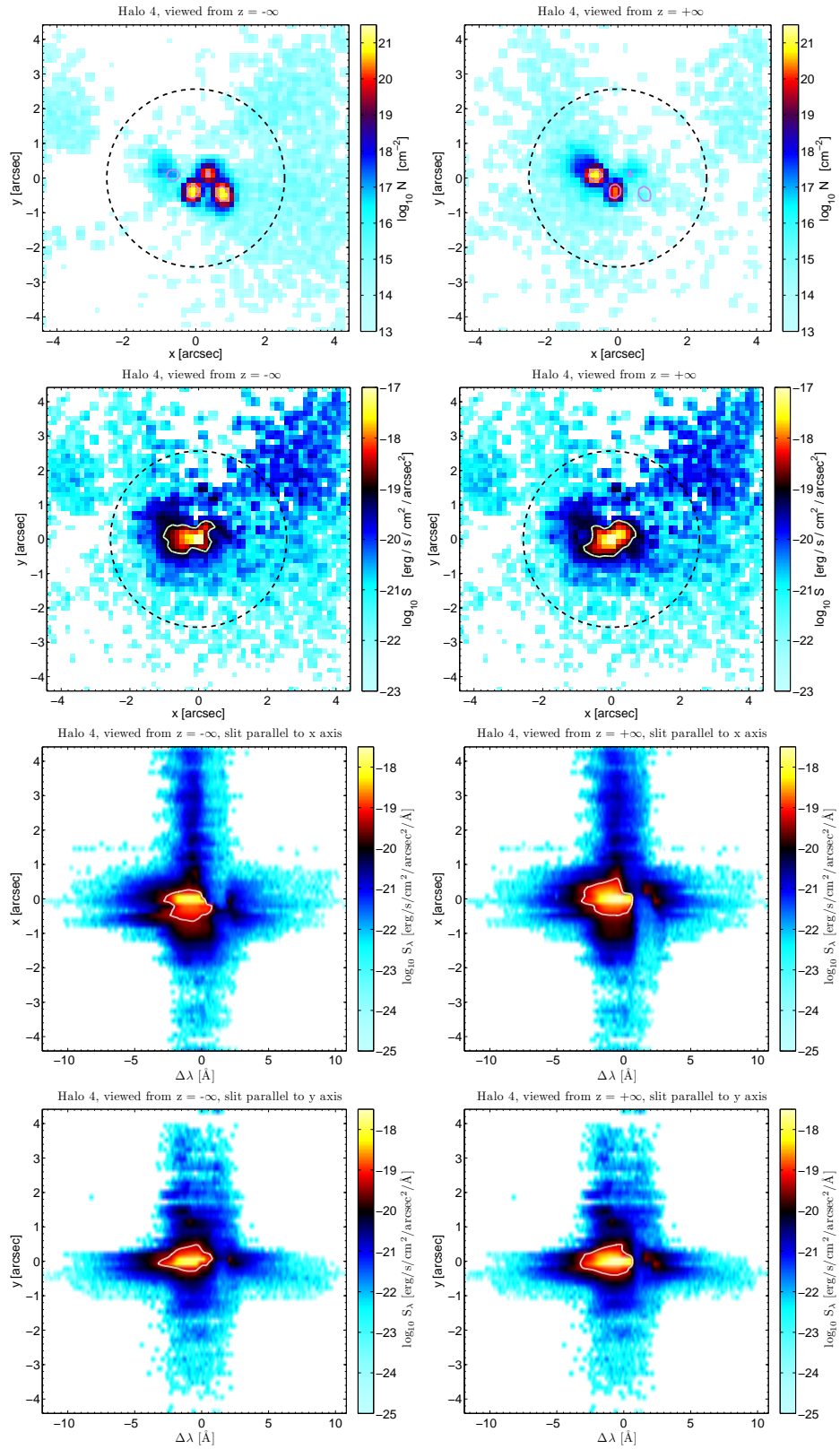Figure 6.17: 2D images and spectra for Halo 4, *y*-direction

Figure 6.18: 2D images and spectra for Halo 4, z-direction

- The angularly-averaged surface brightness profile is most sensitive to the column density of the gas. The profiles are all centrally peaked, especially in the smaller haloes, and are much smoother than the corresponding column density profiles. Our central source is able to illuminate gas at very low column densities ($N_{\rm HI} < 10^{17}$ cm^{-2}), albeit at very faint surface brightness levels.

- A comparison of the 2D column density and surface brightness images shows that the Lyα emission region is larger and smoother than the cross-section for damped absorption. Lyα photons are scattered effectively down to column densities of $\sim 10^{17}$ cm^{-2}, and the central source can effectively illuminate outlying clumps of neutral hydrogen. Asymmetries in the HI distribution can dramatically affect the observed surface brightness, with dense clumps casting shadows as photons are reflected off their surface. A central source of photons can illuminate diffuse, highly ionised gas inside and beyond the virial radius at very faint surface brightness levels.

- The 2D spectra show considerable variety. The same halo viewed from different angles can have very different spectra. A typical line profile is double-peaked with one of the peaks dominant. The separation of the peaks decreases with increasing distance from the central, dense regions of the halo. The dominance of the red or blue peak changes with viewing angle, and is affected by the velocity of the gas relative to the observer. The maximum spectral intensity is quite constant across the different haloes at $S_\lambda \approx 10^{-17.5}$ erg/s/cm^2/arcsec^2/Å, with the decrease in luminosity with mass being countered by reduced spatial and frequency diffusion.

The dependence of the spectra, in both the line shape and the total observed surface brightness, on the viewing angle gives us a different perspective on the models of the last chapter. There we imposed a "duty cycle", so that only a certain fraction of haloes host a Lyα emitter. We could equivalently think of this as an orientation effect — the inhomogeneity of the gas reduces the Lyα luminosity for a certain fraction of viewing angles. A statistically meaningful sample of haloes would need to be investigated in order to determine the probability distribution of the observed flux from a halo of given mass and intrinsic luminosity.

We should note some of the limitations of our modelling in this chapter. Firstly, the failure of the simulations of Tescari et al. (2009) to reproduce the velocity width distribution of the associated metal absorption in DLAs could hint at missing physics. The effect of this missing ingredient(s) would be to increase the velocity of the gas in the halo. The corresponding effect on the Lyα emission depends on exactly how the velocity in increased. If the bulk velocity in the centre of the halo is increased, then this would accelerate frequency-space diffusion resulting in a more centrally peaked surface brightness profile. On the other hand, if the bulk velocity is increased primarily in the outer parts of the halo, then this would have a minimal effect, perhaps shifting photons back toward line-centre and thereby increasing the apparent size of the emitter. If the velocity takes the form of turbulent motion, then this would have the same (comparatively small) effect as raising the temperature.

We have also ignored the effects of dust. Our reasons for doing so were discussed in the last chapter, and need not be repeated here.

Our use of a regular grid may also erase significant sub-grid structure. Small-scale inhomogeneities in the Hi density are likely to have little effect in the absence of dust, as we have seen that the Lyα emission profile smoothes them over. At most, an irregular edge of an Hi region may lead to a shallower surface brightness profile. Inhomogeneities in the bulk velocity would have a greater effect, increasing the frequency diffusion. These inhomogeneities could be modelled as a turbulent velocity, which as mentioned previously has a comparatively small effect.

We have simply injected Lyα photons at the centre of the halo, because our focus here has been on whether centrally emitted Lyα photons in DLAs can account for the large sizes of the Rauch et al. emitters. A more realistic Lyα emissivity would need to consider the interaction of UV radiation from star formation with the surrounding Hi, as well as the possible contribution from a quasar, cooling radiation and fluorescence due to the UVB. The fact that the Hi density peaks very near the centre of the halo means that the majority of photons should be emitted near the centre of the halo, as we have assumed. Making the intrinsic Lyα emission more extended would obviously make the observed emission more extended.

We have considered a small sample of haloes, for several reasons. Firstly, it allows us to expound their complicated features at length. Secondly, Lyα radiative transfer through a 3D grid is time-consuming. Finally, the simulations of Tescari et al. (2009) used a box size that was too small to produce large numbers of haloes with $M_v > 10^{10.5} M_\odot$. This was necessary to give an acceptable resolution. As a result, we are unable at this stage to produce a statistical sample of haloes as we did in the previous chapter. It is clear, however, that many of the assumptions of previous chapters are borne out in the simulations of this chapter: the Lyα emitters have considerable spatial extent, and are larger than the corresponding DLA cross-section as Lyα photons can be effectively scattered by gas with column densities much less than that of a DLA; the spectra are often double-peaked, with inflow/outflow producing a dominant blue/red peak; the radial velocity and mass flow rate are quite moderate toward the centre of the halo, increasing the spatial extent of the Lyα emission; the Lyα emission region is smaller than the virial radius of the halo.

Our main conclusion is to restate the plausibility of the claim of Rauch et al: their faint population of Lyα emitters are the long-sought host population of DLAs. Ultra-faint observations of Lyα emission have the potential to directly probe neutral hydrogen in early galaxies.

Chapter 7

Conclusions and Outlook

Galaxy formation is one of the central problems of Physical Cosmology. Neutral hydrogen plays an important role, linking the collapse of cooling gas into haloes with the formation of stars. Lyman alpha, hydrogen's strongest spectral line, can directly probe neutral hydrogen in the high redshift Universe. Lyα can be observed in absorption in Damped Lyman Alpha systems (DLAs): high H$\textsc{i}$ column density regions that dominate the neutral gas content of the Universe between $z \sim 0 - 5$. Lyα in emission is an important signature of early, star-forming galaxies. Both populations, however, present significant theoretical challenges.

Rauch et al. (2008) performed an ultra-deep spectroscopic survey and discovered a new population of very faint, spatially extended Lyα emitters, which they claimed to be the long-sought host galaxies of DLAs at $z \sim 3$.

In Chapter 3, I developed and tested a Monte Carlo Lyα radiative transfer code to investigate models of early galaxies.

In Chapter 4, I showed that a simple analytical model, which reproduces the incidence rate and kinematics of DLAs in the context of ΛCDM models for structure formation, also reproduces the size distribution of the faint Lyα emitters for plausible parameters, which supports their identification as DLA host galaxies.

The model suggests that galaxies in haloes with $v_c \sim 100 - 150$ km s^{-1} account for the majority of DLA host galaxies, and that these galaxies at $z \sim 3$ are the building blocks of typical present-day galaxies like our Milky Way.

In Chapter 5, the model of Chapter 4 was refined and extended using my newly developed Lyα code to perform detailed 1D radiative transfer calculations. I investigated the spatial and spectral distribution of Lyα emission due to star formation at the centre of DLAs, and its dependence on the spatial and velocity structure of the gas. The modelling reproduces the observed properties of both DLAs and the faint Lyα emitters, including the velocity width and column density distribution of DLAs and the large observed spatial extent of the faint emitters. In the model, haloes hosting DLAs retain up to 20% of the cosmic baryon fraction in the form of neutral hydrogen. The scattering of Lyα photons at the observed radii, which can be as large as 50 kpc, requires the bulk velocity of the gas at the centre of the haloes to be moderate.

In Chapter 6, I presented the results of my 3D Lyα radiative transfer simulations, building on numerical simulations of galaxy formation that include galactic winds and gas infall. The Lyα emission region is shown to be larger and smoother than the cross-section for damped absorption by $\sim 50\%$, with Lyα photons scattered effectively by gas with column densities $\gtrsim 10^{17}$ cm^{-2}. The spectra typically show two peaks, with the relative strength of the red (blue) peak being a reflection of the relative contribution of outflow (inflow) in the velocity profile. There is considerable variation in the observed line profile and spectral intensity with viewing angle. These more realistic models support many of the simplifying assumptions of my previous models, and have the potential to probe the important role of galactic winds in protogalaxies.

The main conclusion is that the faint population of Lyα emitters are indeed the long-sought host population of DLAs. Ultra-faint observations of Lyα emission have exceptional potential to directly probe the spatial distribution and kinematics of neutral hydrogen in early galaxies.

There are a number of ways in which the modelling presented here can be refined and extended. The dependence of Lyα radiative transfer on the kinematic state of the gas means that observations give us the ability to explore the velocity fields of protogalaxies. This provides a complementary probe to the kinematics of low-ionisation metals associated with DLAs. This is particularly important:

the difficulty that numerical simulations of galaxy formation have encountered in modelling this velocity width data casts a worrying shadow over the many successes of these models. The ability of Lyα to probe the neutral hydrogen, rather than metals scattered through the gas by star formation and supernovae, means that Lyα is a much more direct probe of the kinematics of protogalaxies. The challenge that remains is to untangle such information from spectra — inferring the bulk velocity of the gas from the Lyα spectrum is fraught with degeneracies.

One application of this idea is to study Lyα emission from simulated galaxies with a range of galactic wind prescriptions. As mentioned previously, Tescari et al. (2009) ran their simulations for a range of wind models. The dependence of the emergent spectrum on the parameters of the wind model would give us a handle on the influence of galactic-scale outflows on the kinematics of protogalaxies, which is a considerable source of theoretical uncertainty in galaxy formation simulations. Many outstanding problems in galaxy formation are widely believed to find their solution (at least in part) in a greater understanding of galactic winds. An example is the angular momentum problem, where galaxies in simulations shed too much of their angular momentum as they collapse, resulting in small, highly centrally concentrated disks with dominating bulges (Navarro & Benz 1991). Understanding galactic winds is especially important for haloes in the mass-range we identified as the most likely to host DLAs, for which the formation rate of galaxy haloes peaks at $z \sim 3$ (see, e.g. Figures 4 and 5 of Percival & Miller 1999). Exploring these haloes is crucial to our understanding of galaxy formation.

Theoretical models can also be refined using observations at other wavelengths. The star formation that powers Lyα emission will also produce continuum radiation. The relationship between continuum and Lyα emission, especially the increased spatial extent of Lyα emission due to resonant scattering, can provide important information on the sources of Lyα photons in a galaxy. Other wavelengths can also provide independent constraints on the amount and distribution of dust in protogalaxies. Other emission lines, especially other hydrogen lines such as Hα, can provide important information on the interaction of ionising radiation and neutral gas and hence on the Lyα emissivity. These lines can also provide complementary probes of the kinematic state of the gas in protogalaxies.

Advances in cosmological simulations will also improve Lyα radiative transfer

models. Larger 3D radiative transfer boxes will allow simulations to trace the effect of the local IGM on Lyα photons as they escape the galaxies in which they were emitted. Greater spatial resolution (including the incorporation of adaptively refined grids as in Laursen et al. 2009a) allows the effects of small-scale spatial and velocity structure in the gas to be explored, which is particularly important in the presence of dust. Larger simulation boxes will provide a statistically significant sample of haloes, allowing the properties of the population to be predicted. Perhaps most importantly, Lyα models will benefit directly from increasingly accurate modelling of the physics of galaxy formation, especially in relation to galactic winds and the production and distribution of dust.

Analytical models, too, have a continuing role to play in our understanding of Lyα. The complexity of Lyα radiative transfer, and in particular the difficulty of inferring the distribution, temperature and velocity structure of the gas given a spectrum, means that a physical intuition for Lyα radiative transfer is hard-won but crucially important. Analytical models have helped isolate the signatures of various geometries (spheres, slabs, disks, shells, filaments) and velocity structures (static, infall, outflow, rotation, turbulence) in observations of Lyα. There is a need to develop a greater understanding of the degeneracies between these different scenarios, as well as the signatures of different sources of Lyα photons (star formation, cooling radiation, fluorescence).

Our modelling shows the importance of deep Lyα observations such as those of Rauch et al. (2008) in probing the bulk of the neutral hydrogen participating in galaxy formation. Such observations provide an excellent opportunity to see galaxy formation as it happens. The observational community has realised the importance of Lyα, and a number of important projects are on the horizon. A preliminary 17 hour long slit spectrum in the Hubble Deep Field with the Keck I instrument LRIS will soon provide a complimentary data set to the ESO VLT FORS2 observations of Rauch et al. that we have considered here (Rauch et al., in prep.). The third-generation VLT instrument MUSE (Bacon et al. 2004), currently under construction, is an integral-field spectrograph that will reach similar surface brightness limits as Rauch et al. (2008). As Rauch & Becker (2009) have argued, observations of Lyα in the high redshift Universe will be one of the most promising applications of an ELT. Lyα radiative transfer simulations will be indispensable for interpreting the wealth of data provided by these instruments.

Bibliography

Adams, T. F. 1971, ApJ, 168, 575

Adams, T. F. 1972, ApJ, 174, 439

Adelberger, K. L., Steidel, C. C., Shapley, A. E., Hunt, M. P., Erb, D. K., Reddy, N. A., Pettini, M. 2004, ApJ, 607, 226

Ahn, S.-H., Lee, H.-W., Lee, H. M. 2000, Journal of Korean Astronomical Society, 33, 29

Ahn, S.-H., Lee, H.-W., Lee, H. M. 2001, ApJ, 554, 604

Ahn, S.-H., Lee, H.-W., Lee, H. M. 2002, ApJ, 567, 922

Allen, S. W., Schmidt, R. W., Fabian, A. C., Ebeling, H. 2003, MNRAS, 342, 287

Arons, J. 1972, ApJ, 172, 553

Astier, P., et al. 2006, A&A, 447, 31

Auer, L. H. 1968, ApJ, 153, 783

Avery, L. W. House, L. L. 1968, ApJ, 152, 493

Bacon, D. J., Massey, R. J., Refregier, A. R., Ellis, R. S. 2003, MNRAS, 344, 673

Bacon, R., et al. 2004, in Society of Photo-Optical Instrumentation Engineers (SPIE) Conference Series, Vol. 5492, Society of Photo-Optical Instrumentation Engineers (SPIE) Conference Series, ed. A. F. M. Moorwood M. Iye, 1145–1149

Bahcall, N. A. Bode, P. 2003, ApJ, 588, L1

Barkana, R. Loeb, A. 2001, Phys. Rep., 349, 125

Baugh, C. M. 2006, Reports of Progress in Physics, 69, 3101

Birnboim, Y. Dekel, A. 2003, MNRAS, 345, 349

Bond, J. R., Cole, S., Efstathiou, G., Kaiser, N. 1991, ApJ, 379, 440

Bond, J. R., Kofman, L., Pogosyan, D. 1996, Nature, 380, 603

Bonilha, J. R. M., Ferch, R., Salpeter, E. E., Slater, G., Noerdlinger, P. D. 1979, ApJ, 233, 649

Bouché, N., Gardner, J. P., Katz, N., Weinberg, D. H., Davé, R., Lowenthal, J. D. 2005, ApJ, 628, 89

Bower, R. G., et al. 2004, MNRAS, 351, 63

Brocklehurst, M. 1971, MNRAS, 153, 471

Bromm, V., Kudritzki, R. P., Loeb, A. 2001, ApJ, 552, 464

Brooks, A. M., Governato, F., Booth, C. M., Willman, B., Gardner, J. P., Wadsley, J., Stinson, G., Quinn, T. 2007, ApJ, 655, L17

Bryan, G. L. Norman, M. L. 1998, ApJ, 495, 80

Bullock, J. S., Kolatt, T. S., Sigad, Y., Somerville, R. S., Kravtsov, A. V., Klypin, A. A., Primack, J. R., Dekel, A. 2001, MNRAS, 321, 559

Bunker, A. J., Warren, S. J., Clements, D. L., Williger, G. M., Hewett, P. C. 1999, MNRAS, 309, 875

Cantalupo, S., Lilly, S. J., Porciani, C. 2007, ApJ, 657, 135

Cantalupo, S., Porciani, C., Lilly, S. J., Miniati, F. 2005, ApJ, 628, 61

Caroff, L. J., Noerdlinger, P. D., Scargle, J. D. 1972, ApJ, 176, 439

Carroll, S. M., Press, W. H., Turner, E. L. 1992, ARA&A, 30, 499

Casali, M., et al. 2006, in Society of Photo-Optical Instrumentation Engineers (SPIE) Conference Series, Vol. 6269, Society of Photo-Optical Instrumentation Engineers (SPIE) Conference Series

Chapman, S. C., Scott, D., Windhorst, R. A., Frayer, D. T., Borys, C., Lewis, G. F., Ivison, R. J. 2004, ApJ, 606, 85

Charlot, S. Fall, S. M. 1991, ApJ, 378, 471

Christensen, L., Wisotzki, L., Roth, M. M., Sánchez, S. F., Kelz, A., Jahnke, K. 2007, A&A, 468, 587

Ciardi, B. Ferrara, A. 2005, Space Science Reviews, 116, 625

Cole, S., et al. 2005, MNRAS, 362, 505

Coles, P. Lucchin, F. 2002, Cosmology: The Origin and Evolution of Cosmic Structure, Second Edition (John Wiley & Sons, West Sussex, England)

Cooke, J., Wolfe, A. M., Gawiser, E., Prochaska, J. X. 2006, ApJ, 652, 994

Cowie, L. L. Hu, E. M. 1998, AJ, 115, 1319

Croft, R. A. C., Weinberg, D. H., Bolte, M., Burles, S., Hernquist, L., Katz, N., Kirkman, D., Tytler, D. 2002, ApJ, 581, 20

Daddi, E., Cimatti, A., Renzini, A., Fontana, A., Mignoli, M., Pozzetti, L., Tozzi, P., Zamorani, G. 2004, ApJ, 617, 746

Dey, A., et al. 2005, ApJ, 629, 654

Dijkstra, M., Haiman, Z., Spaans, M. 2006a, ApJ, 649, 14

Dijkstra, M., Haiman, Z., Spaans, M. 2006b, ApJ, 649, 37

Dijkstra, M., Lidz, A., Wyithe, J. S. B. 2007, MNRAS, 377, 1175

Dijkstra, M. Loeb, A. 2009, ArXiv e-prints: 0902.2999

Djorgovski, S. G. 1992, in Astronomical Society of the Pacific Conference Series, Vol. 24, Cosmology and Large-Scale Structure in the Universe, ed. R. R. de Carvalho, 73–+

Dopita, M. A. Sutherland, R. S. 2003, Astrophysics of the Diffuse Universe (Springer, Berlin, New York: Astronomy and Astrophysics Library, 2003)

Eggen, O. J., Lynden-Bell, D., Sandage, A. R. 1962, ApJ, 136, 748

Eisenstein, D. J. Hu, W. 1999, ApJ, 511, 5

Eisenstein, D. J., et al. 2005, ApJ, 633, 560

Ellison, S. L., Yan, L., Hook, I. M., Pettini, M., Wall, J. V., Shaver, P. 2001, A&A, 379, 393

Fabian, A. C. 1999, MNRAS, 308, L39

Fall, S. M. Efstathiou, G. 1980, MNRAS, 193, 189

Fardal, M. A., Katz, N., Gardner, J. P., Hernquist, L., Weinberg, D. H., Davé, R. 2001, ApJ, 562, 605

Francis, P. J., et al. 2001, ApJ, 554, 1001

Friedmann, A. 1922, Z. Physik, 10, 377

Frieman, J. A., Turner, M. S., Huterer, D. 2008, ARA&A, 46, 385

Furlanetto, S. R., Schaye, J., Springel, V., Hernquist, L. 2005, ApJ, 622, 7

Fynbo, J. P. U., Prochaska, J. X., Sommer-Larsen, J., Dessauges-Zavadsky, M., Møller, P. 2008, ApJ, 683, 321

Fynbo, J. U., Møller, P., Warren, S. J. 1999, MNRAS, 305, 849

Fynbo, J. U., Thomsen, B., Möller, P. 2000, A&A, 353, 457

Gardner, J. P., Katz, N., Hernquist, L., Weinberg, D. H. 1997a, ApJ, 484, 31

Gardner, J. P., Katz, N., Hernquist, L., Weinberg, D. H. 2001, ApJ, 559, 131

Gardner, J. P., Katz, N., Weinberg, D. H., Hernquist, L. 1997b, ApJ, 486, 42

Gawiser, E., et al. 2006, ApJ, 642, L13

Geach, J. E., Smail, I., Chapman, S. C., Alexander, D. M., Blain, A. W., Stott, J. P., Ivison, R. J. 2007, ApJ, 655, L9

Giavalisco, M. 2002, ARA&A, 40, 579

Giavalisco, M., Koratkar, A., Calzetti, D. 1996, ApJ, 466, 831

Gould, A. Weinberg, D. H. 1996, ApJ, 468, 462

Governato, F., Mayer, L., Brook, C. 2008, in Astronomical Society of the Pacific Conference Series, Vol. 396, Astronomical Society of the Pacific Conference Series, ed. J. G. Funes E. M. Corsini, 453–+

Governato, F., Willman, B., Mayer, L., Brooks, A., Stinson, G., Valenzuela, O., Wadsley, J., Quinn, T. 2007, MNRAS, 374, 1479

Grainge, K., et al. 2003, MNRAS, 341, L23

Haehnelt, M. G., Steinmetz, M., Rauch, M. 1998, ApJ, 495, 647

Haehnelt, M. G., Steinmetz, M., Rauch, M. 2000, ApJ, 534, 594

Haiman, Z. Rees, M. J. 2001, ApJ, 556, 87

Haiman, Z., Spaans, M., Quataert, E. 2000, ApJ, 537, L5

Hansen, M. Oh, S. P. 2006, MNRAS, 367, 979

Harrington, J. P. 1973, MNRAS, 162, 43

Heymans, C., et al. 2005, MNRAS, 361, 160

Hinshaw, G., et al. 2009, ApJS, 180, 225

Hogan, C. J. Weymann, R. J. 1987, MNRAS, 225, 1P

Hu, E. M., Cowie, L. L., McMahon, R. G., Capak, P., Iwamuro, F., Kneib, J.-P., Maihara, T., Motohara, K. 2002, ApJ, 568, L75

Hummer, D. G. 1962, MNRAS, 125, 21

Illingworth, G. Bouwens, R. 2005, in Open Questions in Cosmology: the First Billion Years

Iye, M., et al. 2006, Nature, 443, 186

Jedamzik, K. Prochaska, J. X. 1998, MNRAS, 296, 430

Jena, T., et al. 2005, MNRAS, 361, 70

Johansson, P. H. Efstathiou, G. 2006, MNRAS, 371, 1519

Kashikawa, N., Kitayama, T., Doi, M., Misawa, T., Komiyama, Y., Ota, K. 2007, ArXiv: 0704.2238, 704

Kashikawa, N., et al. 2006, ApJ, 648, 7

Katz, N., Weinberg, D. H., Hernquist, L. 1996a, ApJS, 105, 19

Katz, N., Weinberg, D. H., Hernquist, L., Miralda-Escude, J. 1996b, ApJ, 457, L57+

Kauffmann, G. 1996, MNRAS, 281, 475

Kay, S. T., Pearce, F. R., Jenkins, A., Frenk, C. S., White, S. D. M., Thomas, P. A., Couchman, H. M. P. 2000, MNRAS, 316, 374

Keel, W. C., Cohen, S. H., Windhorst, R. A., Waddington, I. 1999, AJ, 118, 2547

Kennicutt, Jr., R. C. 1998, ApJ, 498, 541

Kereš, D., Katz, N., Fardal, M., Davé, R., Weinberg, D. H. 2009, MNRAS, 395, 160

Kereš, D., Katz, N., Weinberg, D. H., Davé, R. 2005, MNRAS, 363, 2

Kitayama, T., Susa, H., Umemura, M., Ikeuchi, S. 2001, MNRAS, 326, 1353

Kitayama, T., Tajiri, Y., Umemura, M., Susa, H., Ikeuchi, S. 2000, MNRAS, 315, L1

Kodaira, K., et al. 2003, PASJ, 55, L17

Kollmeier, J. A., Zheng, Z., Davé, R., Gould, A., Katz, N., Miralda-Escudé, J., Weinberg, D. H. 2009, ArXiv e-prints: 0907.0704

Kulkarni, V. P., Hill, J. M., Schneider, G., Weymann, R. J., Storrie-Lombardi, L. J., Rieke, M. J., Thompson, R. I., Jannuzi, B. T. 2000, ApJ, 536, 36

Kulkarni, V. P., Hill, J. M., Schneider, G., Weymann, R. J., Storrie-Lombardi, L. J., Rieke, M. J., Thompson, R. I., Jannuzi, B. T. 2001, ApJ, 551, 37

Kuo, C. L., et al. 2004, ApJ, 600, 32

Laursen, P., Razoumov, A. O., Sommer-Larsen, J. 2009a, ApJ, 696, 853

Laursen, P., Sommer-Larsen, J., Andersen, A. C. 2009b, ArXiv e-prints: 0907.2698

Le Delliou, M., Lacey, C. G., Baugh, C. M., Morris, S. L. 2006, MNRAS, 365, 712

Lemaître, G. 1931, MNRAS, 91, 483

Liddle, A. R. Lyth, D. H. 2000, Cosmological Inflation and Large-Scale Structure (Cambridge University Press, Cambridge, UK)

Loeb, A. Rybicki, G. B. 1999, ApJ, 524, 527

Lu, L., Sargent, W. L. W., Barlow, T. A., Churchill, C. W., Vogt, S. S. 1996, ApJS, 107, 475

Macciò, A. V., Dutton, A. A., van den Bosch, F. C., Moore, B., Potter, D., Stadel, J. 2007, MNRAS, 378, 55

Maller, A. H. Bullock, J. S. 2004, MNRAS, 355, 694

Maller, A. H., Prochaska, J. X., Somerville, R. S., Primack, J. R. 2001, MNRAS, 326, 1475

Matsuda, Y., Yamada, T., Hayashino, T., Yamauchi, R., Nakamura, Y. 2006, ApJ, 640, L123

Matsuda, Y., et al. 2004, AJ, 128, 569

McDonald, P. Miralda-Escudé, J. 1999, ApJ, 519, 486

McQuinn, M., Hernquist, L., Zaldarriaga, M., Dutta, S. 2007, ArXiv: 0704.2239, 704

Mo, H. J., Mao, S., White, S. D. M. 1998, MNRAS, 295, 319

Mo, H. J. Miralda-Escude, J. 1994, ApJ, 430, L25

Mo, H. J. White, S. D. M. 2002, MNRAS, 336, 112

Mori, M., Umemura, M., Ferrara, A. 2004, ApJ, 613, L97

Nagamine, K., Ouchi, M., Springel, V., Hernquist, L. 2008, ArXiv e-prints: 0802.0228

Nagamine, K., Springel, V., Hernquist, L. 2004, MNRAS, 348, 421

Nagamine, K., Wolfe, A. M., Hernquist, L., Springel, V. 2007, ApJ, 660, 945

Natta, A. Beckwith, S. 1986, A&A, 158, 310

Navarro, J. F. Benz, W. 1991, ApJ, 380, 320

Navarro, J. F., Frenk, C. S., White, S. D. M. 1996, ApJ, 462, 563

Neufeld, D. A. 1990, ApJ, 350, 216

Neufeld, D. A. 1991, ApJ, 370, L85

Nilsson, K. K., Fynbo, J. P. U., Møller, P., Sommer-Larsen, J., Ledoux, C. 2006, A&A, 452, L23

Nilsson, K. K. Meisenheimer, K. 2009, New Astronomy Review, 53, 37

Nojiri, S. Odintsov, S. D. 2006, ArXiv High Energy Physics - Theory e-prints: hep-th/0601213

Ohyama, Y., et al. 2003, ApJ, 591, L9

Okamoto, T., Gao, L., Theuns, T. 2008, MNRAS, 390, 920

O'Meara, J. M., Prochaska, J. X., Burles, S., Prochter, G., Bernstein, R. A., Burgess, K. M. 2007, ApJ, 656, 666

Osterbrock, D. E. 1962, ApJ, 135, 195

Osterbrock, D. E. 1989, Astrophysics of Gaseous Nebulae and Active Galactic Nuclei (University Science Books, Mill Valley, CA)

Palunas, P., Teplitz, H. I., Francis, P. J., Williger, G. M., Woodgate, B. E. 2004, ApJ, 602, 545

Panagia, N. Ranieri, M. 1973, A&A, 24, 219

Partridge, R. B. Peebles, P. J. E. 1967, ApJ, 147, 868

Peacock, J. A. 1999, Cosmological Physics (Cambridge University Press, Cambridge, UK)

Peebles, P. J. E. 1993, Principles of Physical Cosmology (Princeton Series in Physics, Princeton, NJ: Princeton University Press)

Pentericci, L., Grazian, A., Fontana, A., Salimbeni, S., Santini, P., De Santis, C., Gallozzi, S., Giallongo, E. 2007, ArXiv: astro-ph/07030134

Pentericci, L., et al. 2002, AJ, 123, 2151

Percival, W. Miller, L. 1999, MNRAS, 309, 823

Perlmutter, S., et al. 1999, ApJ, 517, 565

Péroux, C., Dessauges-Zavadsky, M., D'Odorico, S., Sun Kim, T., McMahon, R. G. 2005, MNRAS, 363, 479

Pettini, M. 2004, in Cosmochemistry. The melting pot of the elements, ed. C. Esteban, R. García López, A. Herrero, F. Sánchez, 257–298

Pettini, M. 2006, in The Fabulous Destiny of Galaxies: Bridging Past and Present, ed. V. Le Brun, A. Mazure, S. Arnouts, D. Burgarella, 319–+

Pettini, M., Rix, S. A., Steidel, C. C., Adelberger, K. L., Hunt, M. P., Shapley, A. E. 2002, ApJ, 569, 742

Pettini, M., Steidel, C. C., Adelberger, K. L., Dickinson, M., Giavalisco, M. 2000, ApJ, 528, 96

Piacentini, F., et al. 2006, ApJ, 647, 833

Pontzen, A., et al. 2008, MNRAS, 390, 1349

Press, W. H. Schechter, P. 1974, ApJ, 187, 425

Press, W. H., Teukolsky, S. A., Vetterling, W. T., Flannery, B. P. 1992, Numerical Recipes in FORTRAN. The Art of Scientific Computing (Cambridge: University Press, 2nd ed.)

Prochaska, J. X., Chen, H.-W., Wolfe, A. M., Dessauges-Zavadsky, M., Bloom, J. S. 2008, ApJ, 672, 59

Prochaska, J. X., Herbert-Fort, S., Wolfe, A. M. 2005, ApJ, 635, 123

Prochaska, J. X. Wolfe, A. M. 1997, ApJ, 487, 73

Prochaska, J. X. Wolfe, A. M. 2001, ApJ, 560, L33

Prochaska, J. X. Wolfe, A. M. 2009, ApJ, 696, 1543

Quider, A. M., Pettini, M., Shapley, A. E., Steidel, C. C. 2009, MNRAS, 398, 1263

Quinn, T., Katz, N., Efstathiou, G. 1996, MNRAS, 278, L49

Rauch, M. 1998, ARA&A, 36, 267

Rauch, M. Becker, G. 2009, Astronomy, 2010, 242

Rauch, M., et al. 2008, ApJ, 681, 856

Razoumov, A. O., Norman, M. L., Prochaska, J. X., Sommer-Larsen, J., Wolfe, A. M., Yang, Y.-J. 2008, ApJ, 683, 149

Razoumov, A. O., Norman, M. L., Prochaska, J. X., Wolfe, A. M. 2006, ApJ, 645, 55

Reddy, N. A. Steidel, C. C. 2009, ApJ, 692, 778

Reuland, M., et al. 2003, ApJ, 592, 755

Rhoads, J. E., et al. 2004, ApJ, 611, 59

Riess, A. G., et al. 2004, ApJ, 607, 665

Robertson, H. P. 1935, ApJ, 82, 284

Rosenberg, J. L. Schneider, S. E. 2003, ApJ, 585, 256

Ryan-Weber, E. V., Webster, R. L., Staveley-Smith, L. 2003, MNRAS, 343, 1195

Ryan-Weber, E. V., Webster, R. L., Staveley-Smith, L. 2005, MNRAS, 356, 1600

Rybicki, G. B. Lightman, A. P. 1979, Radiative Processes in Astrophysics (New York, Wiley-Interscience)

Sandage, A., Freeman, K. C., Stokes, N. R. 1970, ApJ, 160, 831

Santos, M. R. 2004, MNRAS, 349, 1137

Schaerer, D. Verhamme, A. 2008, A&A, 480, 369

Schiano, A. V. R., Wolfe, A. M., Chang, C. A. 1990, ApJ, 365, 439

Seljak, U., et al. 2005, Phys. Rev. D, 71, 103515

Semboloni, E., et al. 2006, A&A, 452, 51

Shapley, A. E., Steidel, C. C., Adelberger, K. L., Dickinson, M., Giavalisco, M., Pettini, M. 2001, ApJ, 562, 95

Shapley, A. E., Steidel, C. C., Pettini, M., Adelberger, K. L. 2003, ApJ, 588, 65

Sheth, R. K. Tormen, G. 2002, MNRAS, 329, 61

Sommer-Larsen, J. 2005, ArXiv: astro-ph/0512485

Spergel, D. N., et al. 2003, ApJS, 148, 175

Spergel, D. N., et al. 2007, ApJS, 170, 377

Springel, V. 2005, MNRAS, 364, 1105

Stanway, E. R., et al. 2007, MNRAS, 376, 727

Steidel, C. C., Adelberger, K. L., Shapley, A. E., Pettini, M., Dickinson, M., Giavalisco, M. 2000, ApJ, 532, 170

Storrie-Lombardi, L. J., McMahon, R. G., Irwin, M. J. 1996, MNRAS, 283, L79

Storrie-Lombardi, L. J. Wolfe, A. M. 2000, ApJ, 543, 552

Susa, H. Kitayama, T. 2000, MNRAS, 317, 175

Taniguchi, Y. Shioya, Y. 2000, ApJ, 532, L13

Taniguchi, Y., et al. 2005, PASJ, 57, 165

Tasitsiomi, A. 2006, ApJ, 645, 792

Tegmark, M., et al. 2004, ApJ, 606, 702

Tescari, E., Viel, M., Tornatore, L., Borgani, S. 2009, MNRAS, 397, 411

Thommes, E. Meisenheimer, K. 2005, A&A, 430, 877

Thompson, D., Djorgovski, S., Trauger, J. 1995, AJ, 110, 963

Thoul, A. A. Weinberg, D. H. 1996, ApJ, 465, 608

Unno, W. 1952, PASJ, 4, 100

van Breugel, W., de Vries, W., Croft, S., De Breuck, C., Dopita, M., Miley, G., Reuland, M., Röttgering, H. 2006, Astronomische Nachrichten, 327, 175

van Breukelen, C., Jarvis, M. J., Venemans, B. P. 2005, MNRAS, 359, 895

Veilleux, S., Cecil, G., Bland-Hawthorn, J. 2005, ARA&A, 43, 769

Verhamme, A., Schaerer, D., Atek, H., Tapken, C. 2008, A&A, 491, 89

Verhamme, A., Schaerer, D., Maselli, A. 2006, A&A, 460, 397

Viegas, S. M. 1995, MNRAS, 276, 268

Viel, M., Haehnelt, M. G., Springel, V. 2004, MNRAS, 354, 684

Villar-Martín, M., Humphrey, A., De Breuck, C., Fosbury, R., Binette, L., Vernet, J. 2007a, MNRAS, 375, 1299

Villar-Martín, M., Sánchez, S. F., Humphrey, A., Dijkstra, M., di Serego Alighieri, S., De Breuck, C., González Delgado, R. 2007b, MNRAS, 378, 416

Villar-Martín, M., Tadhunter, C., Morganti, R., Holt, J. 2005, MNRAS, 359, L5

Voevodkin, A. Vikhlinin, A. 2004, ApJ, 601, 610

Walker, A. G. 1936, Proc. London Math. Soc., 42, 90

Warren, S. J., Møller, P., Fall, S. M., Jakobsen, P. 2001, MNRAS, 326, 759

Wechsler, R. H., Bullock, J. S., Primack, J. R., Kravtsov, A. V., Dekel, A. 2002, ApJ, 568, 52

Weinberg, S. 2008, Cosmology (Oxford University Press, Oxford, UK)

White, S. D. M. Rees, M. J. 1978, MNRAS, 183, 341

Wild, V., Hewett, P. C., Pettini, M. 2006, MNRAS, 367, 211

Wilman, R. J., Gerssen, J., Bower, R. G., Morris, S. L., Bacon, R., de Zeeuw, P. T., Davies, R. L. 2005, Nature, 436, 227

Wolfe, A. M. 1986, Royal Society of London Philosophical Transactions Series A, 320, 503

Wolfe, A. M. Chen, H.-W. 2006, ApJ, 652, 981

Wolfe, A. M., Gawiser, E., Prochaska, J. X. 2005, ARA&A, 43, 861

Wolfe, A. M., Prochaska, J. X., Gawiser, E. 2003, ApJ, 593, 215

Wood, K. Reynolds, R. J. 1999, ApJ, 525, 799

York, D. G., Dopita, M., Green, R., Bechtold, J. 1986, ApJ, 311, 610

Yusef-Zadeh, F., Morris, M., White, R. L. 1984, ApJ, 278, 186

Zanstra, H. 1949, Bull. Astron. Inst. Netherlands, 11, 1

Zheng, Z. Miralda-Escudé, J. 2002, ApJ, 578, 33

Zwaan, M., Walter, F., Ryan-Weber, E., Brinks, E., de Blok, W. J. G., Kennicutt, R. C. 2008, AJ, 136, 2886

Zwaan, M. A., Meyer, M. J., Staveley-Smith, L., Webster, R. L. 2005, MNRAS, 359, L30